Enhanced Photon Upconversion by Silicon Metasurfaces

Dissertation

zur
Erlangung des Grades eines
Doktors der Naturwissenschaften
(Dr. rer. nat.)

am
Fachbereich Physik
der
Freien Universität Berlin

vorgelegt von

Doguscan Ahiboz

Berlin 2024

Erstgutachter/in: Prof. Dr. Klaus Lips

Zweitgutachter/in: Prof. Dr. Christiane Becker

Tag der Disputation: 01.10.2024

I declare that this thesis is my own work and has not been submitted for any other degree or professional qualification. Where jointly-authored publications have been included, I have clearly indicated my contributions and those of the other authors. Appropriate credit has been given throughout this thesis to the work of others where referenced.

Contents

Acknowledgements

First and foremost I offer my heartfelt gratitude to my supervisor, Prof. Dr. Christiane Becker, who has supported me during the course of my doctoral study and thesis writing with her patience and knowledge at the same time as allowing me the room to work in my own way. I attribute the level of my doctoral degree to her encouragement and effort and without her this thesis, too, would not have been completed.

I would like to thank my co-advisor Prof. Dr. Klaus Lips who provided me with valuable comments and advises for many perceptive conversations during the development of the ideas in our meetings.

I am much obliged to members of Helmholtz-Zentrum Berlin (HZB) members, Karola Klimm, Rowan W. MacQueen, Engin Özkol, Daniel Amkreutz, and members of Optics for Solar for their help during my research. I am grateful to members of The Federal Institute for Materials Research (BAM), Christian Würth, Elina Andresen and Ute Resch-Genger for their collaboration. I am also highly grateful to Dr. Klaus Jäger for his valuable comments.

I am grateful for the support of my dear friends Majvor, Cansu, Erolcan, and Ermen.

Furthermore, I would like to thank my partner, Franziska, for her love, support, and motivation.

Abstract

Photon upconversion is a non-linear process where multiple photons are absorbed, and a single photon with higher energy than the incident ones is emitted. This process is often achieved by lanthanide ions, such as Erbium ions which are generally embedded in optical inert crystals like Sodium-Yttrium-(tetra) Fluoride. The ability of the Erbium ions to covert the near-infrared photons into shorter infrared, visible and ultraviolet wavelengths opens up many applications such as life sciences and photovoltaics. The efficiency of the photon upconversion through Erbium ions strongly depends on Erbium ion's ability to absorb near-infrared photons. Unfortunately, Erbium, like any other lanthanide group element, is not an efficient near-infrared absorber. Their small absorption cross-section requires intense laser excitation power densities to obtain considerable upconversion luminescence. This requirement limits its applicability for practical applications.

In this thesis, an approach to enhance photon upconversion of the Erbium-doped and Erbium - Ytterbium co-doped Sodium-Yttrium-(tetra)Fluoride upconversion nanoparticles is studied by harvesting strongly enhanced near-fields on silicon metasurfaces. The aim is to reduce the required external excitation power densites for efficient photon upconversion luminescence and to gain a better understanding of resonant phenomena on silicon metasurfaces. To fulfil this aim, the resonant phonemonon on Silicon metasurface resulting strong near fields and photo-physical dynamics of the upconversion nanoparticles are meticulously investigated by experimental and theoretical methods.

As an upconversion enhancing platform, large area ($25\,\mathrm{cm}^2$) silicon mono- and double-layer metasurfaces with hexagonal lattice are produced by a nanoimprint

lithography based method. The resonant phenomena on silicon metasurfaces, such as leaky modes and bound states in continuum on silicon metasurfaces are probed by optical spectroscopy and aided with finite difference element simulations. In the light of the numerical calculations, the spectral position of the leaky modes of silicon metasurface is engineered by a single and simple production parameter; silicon metasurface thickness.

The excitation power density-dependent upconversion dynamics of the upconversion nanoparticles in solution are examined. The results on excitation power density dependent measurements shed on light electonic transition dynamics and luminescence quenching processes. By placing the upconversion nanoparticles on the silicon metasurface and variation of the incident angle, the effect of the 1550 nm light coupling with leaky metasurface modes on upconversion luminescence is investigated. The efficient coupling results in more than 2000-fold enhanced photon upconversion emission on silicon metasurfaces when it is compared with the emission of upconversion nanoparticles on a planar silicon surface.

Moreover, upconversion of Erbium-Ytterbium co-doped upconversion nanoparticles in polymer matrix is studied. The upconversion of the polymer-upconversion nanoparticle layer are investigated with 980 nm laser excitation. The enhanced photon upcoversion on metasurface more than 1000-fold is observed under 980 nm excitation.

These results pave the way to achieve efficient upconversion luminescence even at low excitation power densities inspiring applications in the fields of biophotonics and photovoltaics.

Abstrakt

Die Photonen - Hochkonversion ist ein nichtlinearer Prozess, bei dem mehrere Photonen absorbiert und ein einzelnes Photon mit höherer Energie als die einfallenden emittiert wird. Dieser Prozess wird häufig durch Lanthanid-Ionen wie Erbium erreicht. Erbium-Ionen sind in der Regel in optisch inerte Kristalle wie Natrium-Yttrium-(tetra)-fluorid eingebettet. Die Fähigkeit der Erbium-Ionen, die Photonen des nahen Infrarots in kürzere infrarote, sichtbare und ultraviolette Wellenlängen umzuwandeln, eröffnet viele Anwendungsmöglichkeiten, z. B. in den Biowissenschaften und der Photovoltaik. Die Effizienz der Photonenumwandlung durch Erbium-Ionen hängt stark von der Fähigkeit der Erbium-Ionen ab, Photonen im nahen Infrarot zu absorbieren. Leider ist Erbium, wie jedes andere Element der Lanthanidengruppe, kein effizienter Nahinfrarot-Absorber. Ihr geringer Absorptionsquerschnitt erfordert hohe Laseranregungsleistungsdichten, um eine beträchtliche Hochkonversion - Lumineszenz zu erzielen. Dies schränkt ihre Eignung für praktische Anwendungen ein.

In dieser Arbeit wird ein Ansatz zur Verstärkung der Photonen - Hochkonversion von Erbium -dotierten und Erbium - Ytterbium - codotierten Natrium -Yttrium-(tetra)fluorid - Nanopartikeln untersucht, indem stark verstärkte Nahfelder auf Silizium - Metaoberflächen genutzt werden. Ziel ist es, die erforderlichen externen Anregungsleistungsdichten für eine effiziente Photonen - Hochkonversion - Lumineszenz zu reduzieren und ein besseres Verständnis der Resonanzphänomene auf Silizium - Metaseiten zu erlangen. Um dieses Ziel zu erreichen, werden das resonante Phänomen auf der Silizium - Metasurface, das zu starken Nahfeldern führt, und die photophysikalische Dynamik der Upconversion - Nanopartikel mit experi-

mentellen und theoretischen Methoden eingehend untersucht.

Als Plattform zur Verstärkung der Hochkonversion werden großflächige ($25\,cm^2$) ein - und zweischichtige Silizium - Metasurfaces mit hexagonalem Gitter durch eine auf Nanoimprint - Lithographie basierende Methode hergestellt. Die Resonanzphänomene auf Silizium - Metasurfaces, wie z.B. Leaky Moden und gebundene Zustände im Kontinuum auf Silizium - Metasurfaces, werden durch optische Spektroskopie und mit Hilfe von Finite-Differenzen - Element - Simulationen erforscht. Gemäß der numerischen Berechnungen wird die spektrale Position der Leaky Moden der Silizium - Metasurface durch einen einzigen und einfachen Produktionsparameter bestimmt: die Dicke der Silizium - Metasurface.

Die von der Anregungsleistungsdichte abhängige Hochkonversion - Dynamik der Hochkonversion-Nanopartikel in Lösung wird untersucht. Die Ergebnisse der von der Anregungsleistungsdichte abhängigen Messungen geben Aufschluss über die Dynamik des elektonischen Übergangs von Licht und die Lumineszenzlöschungsprozesse. Durch die Platzierung der Hochkonversion - Nanopartikel auf der Silizium - Metasurface und die Variation des Einfallswinkels wird die Auswirkung der 1550 nm - Lichtkopplung mit undichten Metasurface - Moden auf die Hochkonversion - Lumineszenz untersucht. Die effiziente Kopplung führt zu einer mehr als 2000 - fach erhöhten Photonenemission auf Silizium - Metasurface im Vergleich zur Emission von Nanopartikeln auf einer planaren Siliziumoberfläche.

Außerdem wird die Hochkonversion von Erbium - Ytterbium - codotierten Hochkonversions - Nanopartikeln in einer Polymermatrix untersucht. Die Uptransformation der Polymer - Uptransformations - Nanopartikelschicht wird mit einer Laseranregung bei 980 nm untersucht. Unter 980 nm - Anregung wird eine mehr als 1000 - fache Steigerung der Photonen-Upscoversion auf der Metasurface beobachtet.

Diese Ergebnisse ebnen den Weg zu einer effizienten Hochkonversionslumineszenz auch bei niedrigen Anregungsleistungsdichten, die zu Anwendungen in den Bereichen der Biophotonik und Photovoltaik inspirieren.

List of Abbreviations

ARLM	Angular resolved luminescence measurement
ARRM	Angular resolved reflectance measurement
ARTA	Absolute reflectance and transmittance accessory
ARTM	Angular resolved tranmittance measurement
BIC	Bound states in continuum
CCD	Charge coupled device
CR	Cross relaxation
ESA	Exited state absorption
EMW	Electric magnetic wave
ETU	Energy transfer upconversion
EUV	Extreme ultra-violet
FEM	Finite element method
GSA	Ground state absorption
IR	Infra-red
MPR	Multi phonon relaxation
NIL	Nano imprinting lithography
NIR	Near infra-red
PDMS	Polydimethylsiloxane
PMT	Photo multiplier tube
PhC	Photonic crystal
SERS	Surface enhanced raman spectroscopy

SHG	Second harmonic generation
s-NIL	Soft-nano imprinting lithography
SPR	Surface plasmon resonance
STPE	Simultaneous two photon excitation
TE	Transverse electric
TEC	Thermo-electrical cooling
UC	Upconversion
UCNP	Upconversion nano particle
UV	Ultra-violet
TM	Transverse magnetic

1 Introduction

Materials can interact with light in many different ways which we experience in our daily lives: light can penetrate through our windows, a shiny metallic surface reflects incident light, or our sunglasses partially block sunlight by reducing its intensity reaching our eyes. Some materials interact with light in a peculiar way: very small particles containing lanthanide elements can change wavelengths (colors). Such particles emit a single high-energy photon (energy package of light) when they absorb at least two low-energy photons, which is called photon upconversion (UC). For example, when tiny particles containing Erbium (Er), which is a lanthanide group element of the periodic table, are put under an infrared light source, they start to emit visible light. Such materials are of particular interest, besides their colorful appearance under infrared light: they open up many applications that have a direct impact on our daily lives.

The lanthanide group elements are often subjected to scientific research on photon UC materials for applications, such as anti-counterfeit inks [1], upconverter for solar cells [2], bio-sensing [3], nano-scale sensors [4–6]. What has been making lanthanide-based UC appealing to the photonics research community? The answer to this question immediately emerge from the very first research article on photon UC by N. Bloembergen in 1959: the described multi-energy level system can be easily satisfied by lanthanide group elements. In his seminal paper proposing photon UC, N. Bloembergen suggests an application idea; a near infra-red quantum counter consisting of a photon converter, a filter, and a photomultiplier tube (PMT) by pointing potential applications [7], which can be realized by employing lanthanide ions. In the following studies in the 1960s, photon UC is considered small effect in rear-earth salts and rear-earths impurities in glass [8]. In follow-

ing years, research interest moved lasing action on trivalent-Erbium (Er^{3+})-doped glasses [9–11]. The discovery of the multi-phonon relaxation (MPR) process and advances in understanding inter-ionic interaction on lanthanide elements let the focus of the UC research move towards UC applications [12–16]. The following studies on the UC mainly focused on increasing the emission intensity by investigating emission of the lanthanide ions in various bulk crystal materials and tuning the emission color by co-doping the host material with multiple lanthanide ions or transition group metals [17–21]. The next breakthrough in the field was the development of lanthanide-doped colloid synthesis methods [22–25]. The colloidal synthesis of the lanthanide-doped UC nanoparticles (UCNP) flourished the research on UC [8, 26, 27]. Depending on desired UC emission and the excitation source wavelength, UC can be attained via various lanthanide group elements. Particularly, Er^{3+} is exploited owing to its emission and excitation wavelengths covering the first (650 nm - 950 nm) and the third (1550 nm - 1870 nm) biological window, where absorption by biological tissue and by water is minimum besides the autofluorescence of the biological molecules are low in these wavelength ranges [28–30]. Moreover, the ground state absorption of the Er^{3+} between 1450 nm - 1600 nm overlaps with the significant part of the solar spectrum between 1400 nm and 1600 nm [31], which makes Er^{3+} a promising candidate for harvesting sub-bandgap photons (E_{photon} < 1.12 eV) that cannot be absorbed by Silicon (Si) solar cells. Despite the exciting application ideas, the UC through Er^{3+} UC is a latent application. Similarly, achieving UC emission of the Er^{3+} is crucial for realizing the sub-bandgap absorption losses of the Si solar cells. Utilizing the sub-bandgap photons of Si solar cells can improve the photo-induced current generated by a Si solar cell enabling photo-conversion efficiencies beyond the fundamental efficiency limit for solar cells [32]. The early examples of transferring the energy of the near-infra-red (NIR) radiation to Si conduction band electrons were performed by using a thick UC film on the bottom of the Si solar cells [33–35]. Although a photocurrent across the solar cell was achieved, these values are obtained by strong excitation power density (P_{exc}), which are impossible to reach under 1 Sun (1000 W/m^2) irradiance. A later approach was developed by combining the UC layer with elements of non-imaging optics, such as solar concentrators. Although a small improvement was achieved, the practical application of the UC in Si solar cells was still far from applicability [27]. Moreover, an application such as a bio-sensing application, requires a sensible signal from nano-emitters [36]. In general, high-power light sources are used to

increase emission intensity of a poor emitter. Such a high-power light source can consume so much energy [37, 38].

In recent years, methods of nano-optics were applied to enhance the luminescence of the UCNPs. A common way to overcome high-irradiance requirement is to increase electric field energy locally; one of the very first significant effects put on the reduction of intense irradiation requirement was demonstrated in the early '80s in the context of surface-enhanced Raman spectroscopy (SERS) [39]. The advances in SERS were followed by the other fields of photonics research such as plasmonics, photonic crystals (PhC), and metasurface enhanced optical phenomena. The dielectric or metallic nano-structured surface can form intense local electric fields, once certain physical conditions are satisfied, i.e. the wavelength of the excitation source (λ_{exc}) incident on the nanostructure is resonant with an electromagnetic mode of the structure. When a luminescent material is placed inside a periodic nanostructure or in close vicinity of nano-structured dielectric or metallic surfaces, its photon absorption and luminescence can be enhanced. Nano-structured metal surfaces, for example, support surface plasmon resonances (SPR) [40–43]. The SPR-enhanced luminescence has been exploited extensively by the photonics research community and many examples of SPR enhanced luminescence by metallic slabs composed of nanoholes [44, 45], plasmonic nano-rods [46, 47] and nano-particle mono-layers [48–51] were demonstrated. Although reasonable luminescence enhancement factors are achieved by the metallic nanostructures mentioned above, the enhancement factors are limited by the parasitic plasmonic absorbance that originated from the metallic nature of the plasmonic nanostructures [52]. The plasmonic effects on SPR are strongly dependent on the inter-particle distance, i.e. contact of the luminescent particle and the metallic surface [53]. These can be detrimental to luminescence enhancement. Moreover, precise control of the inter-particle distance is needed for maximizing the luminescence enhancement by SPR systems [54]. Alternatively, a dielectric nanostructure can overcome the challenges introduced by metallic nanostructures while enhancing the local electric field energy density [55–59]. Periodically arranged dielectric nano-beads [41, 60, 61], nano-disks [62–65] and dielectric photonic crystal slabs and metasurfaces [56, 57, 59] opened up many practical applications by enhancing the emission and excitation radiation. The realization of promising applications relies on understanding the physics behind the UC conversion mechanism and developing ways to control interactions between upconverters and metasurfaces.

At this point, it is necessary to define explicitly what is a photonic metasurface. A photonic metasurface is an artificially produced two-dimensional device that contains structural units with different dielectric constants, i.e. laterally alternating air - dielectric surface. What distinguishes an artificially produced surface from any other artificial two-dimensional structure is that the building units (also known as meta-atom or meta-molecule) on the metasurface interacting with light are considerably smaller than the wavelength of the light. These kinds of artificial materials were first predicted by V.G. Veselago as materials exhibiting negative dielectric permittivity and magnetic susceptibility in 1968 [66]. The development of the metasurface is closely related to PhCs, which consist of periodically varying dielectric materials. Later, two seminal works published in 1987 by E. Yablonovitch and S. John accelerated research on photonic crystals [67, 68]. In the following years, photonic gap and guided resonances in photonic crystals and photonic crystal slabs were extensively investigated [69–72]. The photonic crystal slabs gained interest since they can be produced easily when compared to the three-dimensional photonic crystals, which are produced by costly lithographic methods [73]. The advances in nano-production techniques lead to feasible and large-area production of photonic crystal slabs with nano features as small as to be considered as metasurface [45, 74, 75]. Especially, periodically nano-patterned dielectric metasurfaces gained broad attention due to a special kind of optical resonances existing on them: Leaky modes. As inferred by its name, a leaky mode is an evanescent wave propagating along the metasurface, which may create strong electric fields when the leaky mode couples with external radiation on and inside a metasurface [70, 76–78].

The aim of this doctoral study is two-folded: (1) To investigate the physical mechanism underlying photon UC of Er-doped hexagonal phase Sodium-Yttrium-(IV)-Fluoride (β-$NaYF_4$:Er^{3+}) and Er/Ytterbium (Yb) co-doped hexagonal phase β-$NaYF_4$ (β-$NaYF_4$:Yb^{3+}/Er^{3+}), and their interaction with the leaky modes of the silicon metasurface, (2) tailoring the resonance phenomena on silicon metasurface for enhancing photon-UC of β-$NaYF_4$:Er^{3+} nanoparticles to enable practical applications of photon UC for low external irradiance conditions. A schematic in Fig. 1.1 illustrates the idea behind this thesis: enhanced photon upconversion of the UCNP layer on Si metasurface. The light incident on the metasurface (left) and on the planar silicon surface (right) with incident angle θ represents IR excitation. The effect of the enhanced UC emission is represented by bright green light while dim green light represents UC luminescence on the planar Si surface.

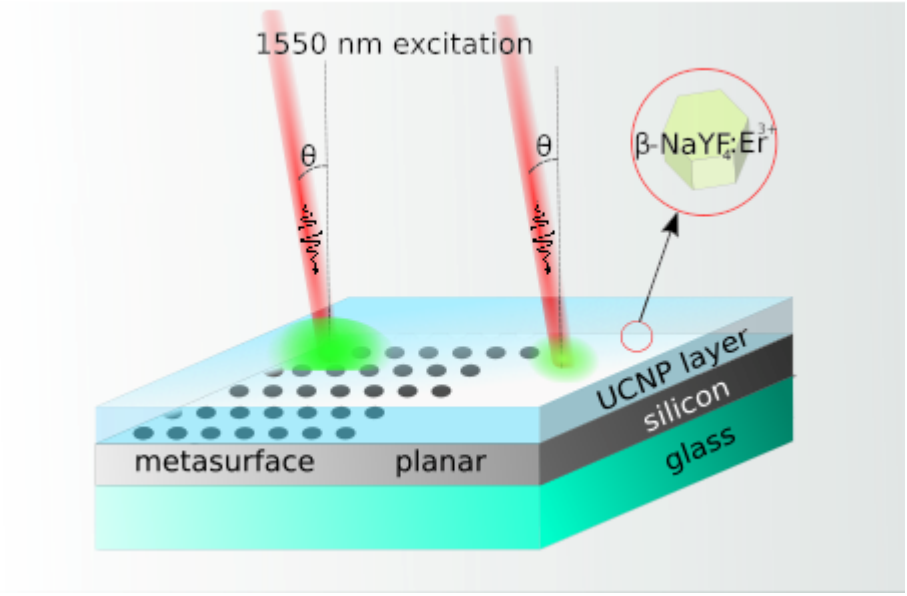

Figure 1.1: A schemetic illustration of silicon metasurface enhanced upconversion emission from β-$NaYF_4$:Er^{3+} nanoparticle layer. Taken from Ahiboz *et al*. [79]

This monograph is written in a way that provides the reader with theoretical aspects and experimental techniques before diving into a discussion on experimental findings. In **Chapter-2** and **Chapter-3**, the fundamentals and theoretical background of metasurfaces and photon UC are briefly given. The definition and properties of metasurfaces are explained while keeping the main focus on the resonant phenomena of metasurfaces leading to strong near-electric fields in Chapter-2. It is indeed unattainable to cover all aspects of metasurfaces. Nonetheless, some of their most crucial attributes of them regarding their interaction are revisited. In Chapter-3, photon UC via lanthanide group elements is outlined. Fundamental building blocks of the photon UC dynamics are presented prior to the rate equation model of the UC luminescence. The experimental and computational techniques that are subjected to this thesis are elaborated in **Chapter-4**. First, the silicon metasurface production and its process steps are explained in detail. Then, the reader is apprised of the synthesis of the UCNP as well as the characterization of the UCNP. Next, optical setups employed and designed for the experiments are presented in detail. Finally, brief explanations of numerical methods used for simulated experimental results finalize Chapter-4. In **Chapter-5** to **Chapter-7** the outcome of the experiments is revealed. Names of each researcher who collaborated and contributed to this study are pronounced as well as their contribution

to this work. The results start with **Chapter-5**: experimental and numerical findings begin with the details of spectral engineering of the leaky modes and observed resonance phenomena on both mono- and bi-layer silicon metasurface [80, 81]. It is demonstrated that the spectral position of the leaky modes of the Si metasurface can be adjusted by changing its Si thickness. Furthermore, various types of optical phenomena are discussed on both mono- and double-layer Si metasurface. In **Chapter-6**, β-$NaYF_4$:Er^{3+} UCNP and their excitation power dependent UC dynamic are discussed by a model based on the rate equations of population densities of the electronic levels of Er^{3+}. In **Chapter-7**, the effect of the electric near field generated after laser excitation and the leaky modes coupling on the luminescence of β-$NaYF_4$:Er^{3+} UCNPs are demonstrated [6, 79]. UC emission of β-$NaYF_4$:Er^{3+} and β-$NaYF_4$:Er^{3+}/Yb^{3+} more than 2000-fold and 1000-fold is enhanced on Si metasurface, respectively. In **Chapter-8** a complete discussion of metasurface enhanced photon UC for its practical application is provided. Feasibility and limitations on photon UC for different application fields are also accentuated. Moreover, an outlook is drawn on further improvement that can be done to increase UC luminescence on metasurfaces. The thesis is concluded in **Chapter-9** by revisiting the problem and the offered solutions by the doctoral study subject of this monograph.

2

Fundamentals-I: Dielectric Metasurfaces

Photonic meta-structures, such as photonic crystals and metasurfaces, are pseudo artificial structures that can interact with light incident on them and change the way light behaves. They can be found in nature, as a result of natural processes such as evolution or tectonic activity of the earth, as a form of opal mineral (periodically arranged silica spheres), and in some species of butterflies (Thecla opisena) on their wings or they can be produced artificially in laboratory condition to control and change the behavior of the light [82–85]. What differentiates them from ordinary dielectric media is their ability to shape and change the properties of the light precisely in unusual ways that we experience in our daily life which lead to the realization many devices can be beneficial for our everyday life [86]. Some of those benefits can be achieved through either periodic or non-periodic structures. For example, random arrangement of nano-spikes can increase the transmission of light while periodic nano-structure containing metasurface can selectively filter certain wavelengths of light [87, 88]. Periodic nanostructures are, here, the focus.

2.1 Two Dimensional Extended Structures: *Photonic Crystals, Photonic Crystal Slabs and Metasurfaces*

An extended structure is an assembly of the small structures constituting a larger structure such that each small structures repeat itself with a period through the dimensions of extension. For example, a crystal material, i.e. $NaYF_4$, has subunits containing one Sodium and Yttrium, and four Fluorine atoms. This block

can be imagined as a small box repeating itself in three dimensions and forming a bulk crystal. Analogous to crystals, extended dielectric structures are repetition dielectric materials with a repetition period. In this case, dielectric constants (or equivalently refractive indices) are periodically changing in space instead of atoms.

A two-dimensional PhC is an extended dielectric structure having a plane of periodicity with periodically changing dielectric material in two dimensions. Such a structure is illustrated in Fig. 2.1 (a). A two-dimensional photonic crystal extends infinitely in three dimensions, however, it has an extended structure in only two dimensions. In other words, dielectric material alternates on x-y plane. The dielectric blocks alternating with period p, gray for n_1 with unit length d_1 and blue for n_2 with d_2, is shown in Fig. 2.1 (b) for a two-dimensional cross-section of the PhC. A PhC slab, similar to a two-dimensional PhC, is an extended dielectric structure in two dimensions. In contrast with two-dimensional PhC, a PhC slab has a finite thickness t. Two examples of PhC slabs are depicted in Fig. 2.1 (c) and (d). The PhC slab is suspended in the air in Fig. 2.1 (c) while the PhC slab in Fig. 2.1 (d) is built on a substrate with refractive index n_3. The major difference between the two PhC slabs is the translation symmetry on z-direction and mirror symmetry with to x-y plane. A dielectric metasurface, on the other hand, is nearly identical to a dielectric Si PhC. A PhC slab can be considered as a metasurface when the wavelengths of light (λ) interacting with the nano features of PhC is smaller than the size of the nano-features, such as d, p and t in Fig. 2.1.

2.2 Properties of the Metasurface

A metasurface interacts with the light and can dramatically change its temporal and spatial behavior [89]. These properties can be controlled by changing the geometric or material properties of a metasurface. Geometric parameters can be the shape, feature size, or repetition period of the nano-features of a metasurface while the electronic properties can be changing refractive and extinction coefficients of the nano-features by material choice and electrical modulation of the dielectric constant. Light, as an electromagnetic wave, propagating in z-direction in Fig. 2.1 can be described as [90]:

$$\mathbf{E}(x,y,z,t) = \mathbf{F}(x,y,z,t)\mathbf{A}(z,t)\Phi(z,t)\mathbf{e}(z,t)e^{i(\omega t - kz)} \tag{2.1}$$

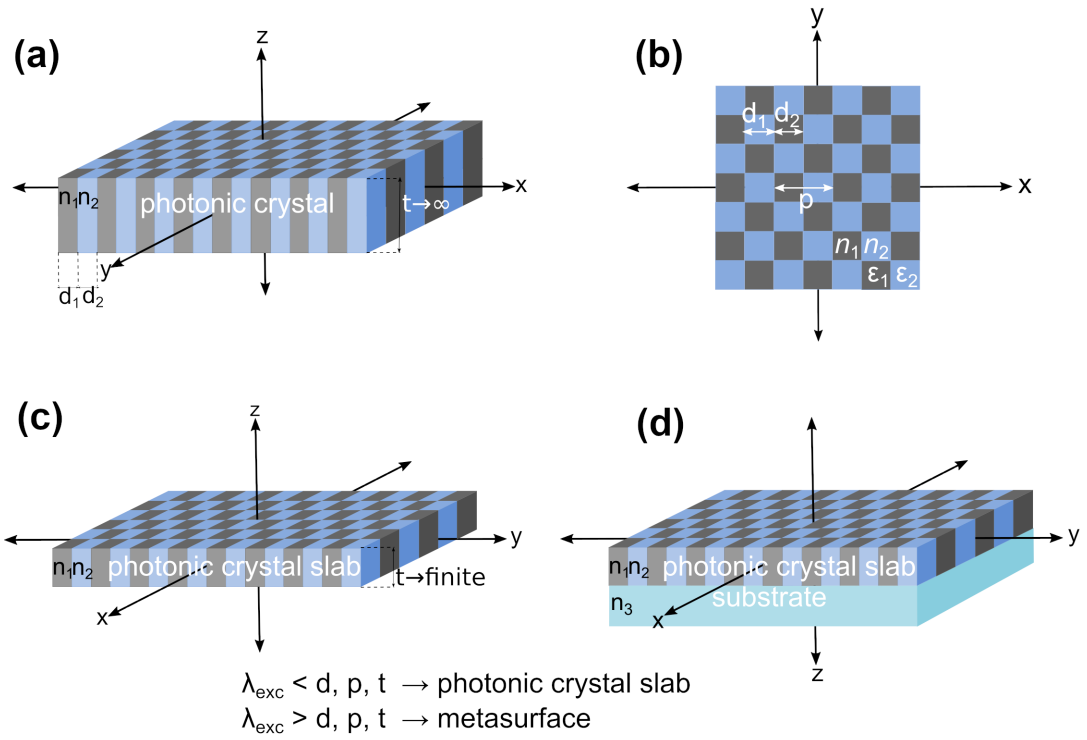

Figure 2.1: Extended dielectric structures in two-dimensions: (a) A two dimensional photonic crystal with transnational symmetry with respect to x-, y- and x-axes. (b) A cross-section figure showing plane of periodicity (x-y plane) of the two dimensional extended structure with two different dielectric materials with n_1 (ϵ_1) and n_2 (ϵ_2). (c) A dielectric photonic crystal slab with a finite thickness t and extended structure on(x-y) plane, and (b) a dielectric photonic crystal slab with a substrate which having no translation symmetry in on z-axis.

A metasurface can be designed to interact with every element of the Eqn. 2.1 so that overall electromagnetic wave $\mathbf{E}(x,y,z,t)$ can be altered. A metasurface can act as a collection of micron-size tiny lenses, which changes the spatial shape $\mathbf{F}(x,y)$ of the electromagnetic wave incident on its surface [91]. The ability of wave-front shaping of the metasurfaces enables the spatial control of the light at a microscopic level, i.e. light bending on a photonic microchip [92]. The control of the amplitude $\mathbf{A}(z,t)$ and the phase $\Phi(z,t)$ of the electromagnetic wave can realize computer-generated 3-dimensional holography technology [93, 94]. The control over the polarization of the electromagnetic wave by a metasurface enables the realization of extremely small polarization splitters compared to their conventional bulky crystal-based beam splitters while maintaining efficient light transmission [95, 96]. More-

over, geometrical parameters of the metasurface, such as the period and size of the nano-features on the metasurface, can be designed to create intense electromagnetic fields within or close vicinity of the metasurface. The created strong near-fields result in a dense electromagnetic energy density distribution which improves incident on the metasurface within a certain volume, before the energy dissipated through the space. Localization of the electromagnetic energy carried by incident light on metasurface; resulting in hot spots where electromagnetic energy density can dramatically affect the absorption of the photons by a nano-emitter on a metasurface [97].

2.3 Theoretical Aspects of the Metasurface

2.3.1 Maxwell equations for extended dielectric structures

Maxwell equations in a dielectric medium in the absence of free current density and free charges can be expressed as [98]:

$$\nabla \cdot \mathbf{D}(r,t) = 0 \tag{2.2}$$

$$\nabla \times \mathbf{E}(r,t) = -\frac{\partial \mathbf{B}(r,t)}{\partial t} \tag{2.3}$$

$$\nabla \cdot \mathbf{B}(r,t) = 0 \tag{2.4}$$

$$\nabla \times \mathbf{H}(r,t) = \frac{1}{c^2}\frac{\partial \mathbf{B}(r,t)}{\partial t} \tag{2.5}$$

where $\mathbf{E}$ and $\mathbf{B}$ are electric and magnetic field vectors, r (m) and c (m/s) are position vector and the speed of light in vacuum. $\mathbf{D}(r,t)$ and $\mathbf{H}(r,t)$ are the auxiliary macroscopic fields of electric and magnetic fields. The auxiliary field are connected electric field with dielectric permittivity ϵ and magnetic permeability μ as $\mathbf{D}(r,t) = \epsilon\mathbf{E}(r,t)$ and $\mathbf{B}(r,t) = \mu\mathbf{H}(r,t)$. Most of the optical materials has $\mu \approxeq 0$, $\mathbf{B}(r,t)$ can be approximated as $\mathbf{B}(r,t) = \mu_0\mathbf{H}(r,t)$ [99].

Time-varying Maxwell equations can be given by it separable form (space and time):

$$\nabla \cdot \mathbf{D}(\mathbf{r},t) = \nabla \cdot (\epsilon(r)\mathbf{E}(\mathbf{r}))e^{-iwt} = 0 \tag{2.6}$$

$$\nabla \times (\mathbf{E}(\mathbf{r},t) + \frac{\partial \mathbf{B}(\mathbf{r},t)}{\partial t} = \nabla \times \mathbf{E}(\mathbf{r}) - i\omega \mathbf{B}(\mathbf{r}) = 0 \tag{2.7}$$

$$\nabla \cdot \mathbf{B}(\mathbf{r},t) = 0 \tag{2.8}$$

$$\nabla \times \mathbf{H}(r) = \frac{1}{c^2}\frac{\partial \mathbf{E}(r)}{\partial t} \tag{2.9}$$

by solving the Eqn. 2.6 - 2.9, an eigen value equation for the magnetic field H(r,t) as following:

$$\mathscr{L} \times \mathbf{H}(r) = \frac{\omega^2}{c^2}\mathbf{H}(r) \tag{2.10}$$

which has the eigenvalue of w^2/c^2 and Hermitian operator $\mathscr{L}$ is:

$$\mathscr{L} = \nabla \times \frac{1}{\epsilon(r)}\nabla \tag{2.11}$$

where $\epsilon(r)$ (F/m) is the electric permittivity at a position r. The eigenvalue of the Eqn. 2.10 with ω gives the mode; the electromagnetic wave solutions in a medium, solutions for an electromagnetic field [69]. Although the Maxwell equation can be expressed as an eigenvalue problem for $\mathbf{E}(r)$, the use of the $\mathbf{H}(r)$ is commonly preferred for mathematical convenience [69]. One of the most important properties of the Maxwell equations is that they are scale-invariant, namely, there is no fundamental scale in their solution [69, 98]. If the r is scaled as $r \rightarrow \Lambda r^{'}$, the solution of the master equation for $r^{'}$ becomes as following [100]:

$$\mathscr{L} \times \mathbf{H}\left(\frac{r}{\Lambda}\right) = \frac{(\Lambda\omega)^2}{c^2}\mathbf{H}\left(\frac{r}{\Lambda}\right) \tag{2.12}$$

where Λ is a scalar quantity. An important consequence of the scaling in Eqn. 2.12 appears on its eigenvalue; the frequency of the mode is also scaled, hence, the new frequency can be found as $\omega^{'} = \Lambda\omega$ [69].

When the master equation is solved for a linear dielectric media, the electromagnetic modes with the frequency of ω can be found. However, extended structures possess unique solution for $\mathbf{H}(r)$ [69, 100]. According to Bloch's theorem, the solution of the master equation inside an extended structure exists with a plane wave solution which reflects the periodic behavior of the dielectric function [101].

$\mathbf{H}(r)$ can be re-written in Bloch's wave form as below [102]:

$$\mathbf{H}(r) = \mathbf{h}_k(r)e^{ikr} \tag{2.13}$$

where Bloch's function $\mathbf{h}_k(r) = \mathbf{h}_k(r+T)$ reflects the transitional symmetry of periodic dielectric function. As an illustrative example, the Bloch function is solved for the 2-dimensional extended dielectric structure with COMSOL Multi-physics in Fig. 2.2 (a). The vectors $r_1 = p$ and $r_2 = \sqrt{3}p$ show the high symmetry direction $\Gamma \rightarrow$ K and $\Gamma \rightarrow$ M in real space, which are the first and the second near-neighboring dielectric points. The diameter of the dielectric region with ϵ_1 is $d = 0.4\,p$ while $\epsilon_1 = 12\epsilon_2$. The two-dimensional extended structure can be represented in momentum (or reciprocal) space equivalently, as shown in Fig.2.2 (b). In this case, real space lattice vectors transform into momentum space lattice vectors as following [103]:

$$k_1 = \frac{2\pi}{r_1} = \frac{2\pi}{p} \quad \text{and} \quad k_2 = \frac{2\pi}{r_2} = \frac{2\pi}{\sqrt{3}p}$$

The transformation from real space to momentum has an impact on the distance between Γ point and the first and second nearest neighboring points: the first nearest neighboring point in real space becomes the second nearest neighboring distance, likewise the second nearest neighboring points in real space becomes the first nearest neighboring point in momentum space. This means that the direction of the $\Gamma \rightarrow$ M and $\Gamma \rightarrow$ K replaces with the transformation to momentum space. Nonetheless, any point in momentum space that can be represented by the linear combination of the real space lattice vectors:

$$k = ak_1 + bk_2 \tag{2.14}$$

where a and b are constants. The red shaded area in Fig. 2.2 (b) is the first Brillouin zone, which is an irreducible area in momentum space that contains all the symmetries of the whole extended structure. When the Eqn. 2.13 solved for the first Brillouin zone for a k through the $\Gamma \rightarrow$ M and $\Gamma \rightarrow$ K direction, the mode diagram in Fig. 2.3 is obtained as: Guided modes are the mode solution of the Eqn. 2.13 with real-valued ω for the extended dielectric structure which is under the light line in Fig.2.3 [104]. Modes of the photonic bands are forbidden from coupling with external radiation, hence they are guided along the plane of periodicity [69]. Any EMW

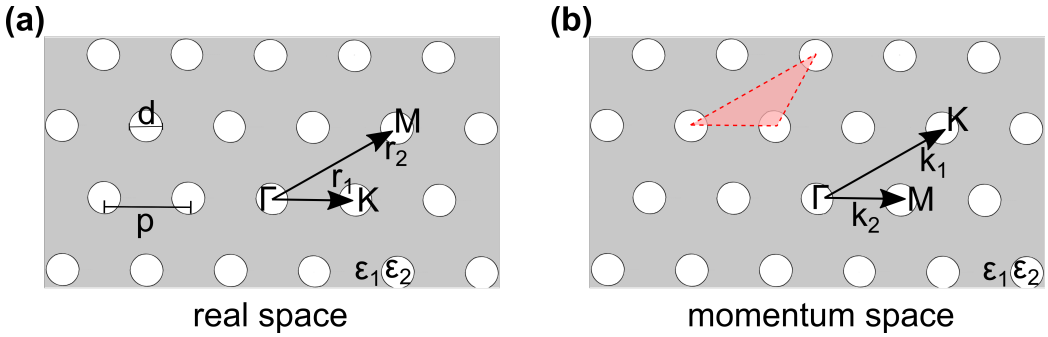

Figure 2.2: A two dimensional extended dielectric structure with hexagonal lattice in (a) real space and (b) momentum space. The gray region and white circles are the domains of the dielectric materials with ϵ_1 and ϵ_2. The red shaded area represent the first Brillouin zone.

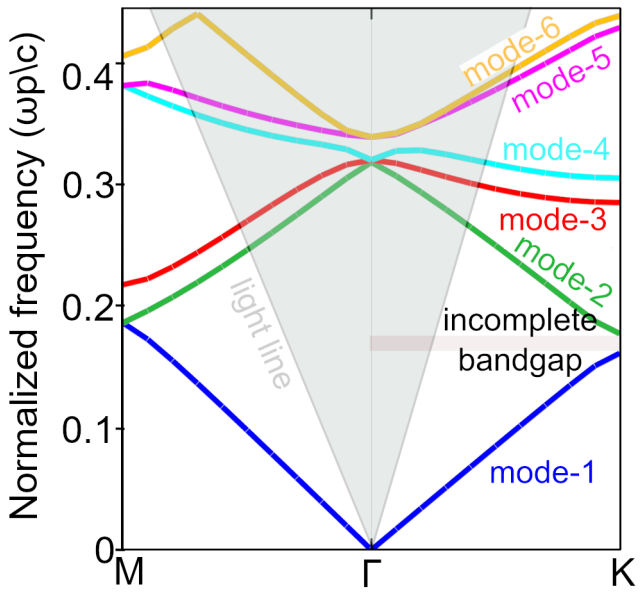

Figure 2.3: Modes solution of two dimensional dielectric extended structure. Red shaded area shows incomplete bandgap and gray shaded area above the light line represents radiation continuum

incident with k with the frequencies of photonic bandgap on the two-dimensional photonic crystal will be scattered from the boundary of each Brillouin zone, resulting in destructive interference [100, 101]. The only resonant interaction between incident light and guided modes is below the light line. However, it is impossible to produce such an infinitely thick photonic in practice.

The solutions for the first 6 photonic bands, which give electromagnetic mode frequencies for a given k, are shown in Fig. 2.3 for three high symmetry directions previously shown in Fig. 2.2. The modes above the light line are inaccessible since the light line gives the speed of light $c = \omega/k$ [69]. They only exist on the extended plane of periodicity with frequencies of the photonic bands, indeed, those modes are *guided modes* of the PhC. However, not all the modes in the photonic bands above the light line are inaccessible, since band structures are folded over the first Brillouin zone to show photonic band structure in a single frame. Moreover, a unique property of a two-dimensional extended dielectric structure appears immediately when the momentum space vector approaches K direction, which is the frequency gap at the edge of the first Brillouin zone. This band of forbidden frequencies is called a photonic bandgap. However, this gap is not a complete photonic bandgap, contrary to its complete photonic bandgap exhibiting three-dimensional PhC counterparts, which only exists in $\Gamma \rightarrow$ K direction. This means that waves with frequencies within incomplete bandgap are not allowed to propagate on the extended plane in $\Gamma \rightarrow$ K direction. Any wave incident on $\Gamma \rightarrow$ K direction with forbidden frequencies scatters from the edge of the Brillouin zone, resulting in destructive interference EMW on an extended plane. Nevertheless, the presence of allowed modes inside the two-dimensional structure and the photonic bandgap gives a distinctive behavior to extended structures, they can exhibit filtering response by cutting out the particular EMW with wavelengths within its photonic bandgap [105].

2.4 Interactions of Dielectric Metasurfaces with Electromagnetic Waves

Metasurface has diverse ways to interact with the light incident on it. These interactions can be divided into two groups depending on the presence of resonant interactions: Off- and on- resonant interactions. These two types of interactions are illustrated in Fig. 2.4 (a) and (b). The difference between on- and off-resonant

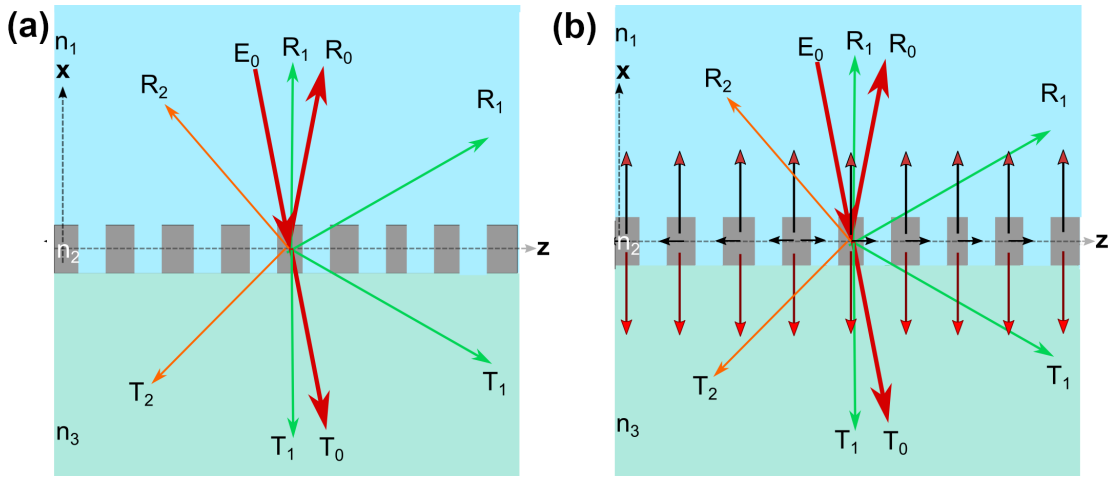

Figure 2.4: Interactions on dielectric metasurfaces: (a) off-resonant interactions and (b) on-resonant interaction.

interactions is based on the interactions on metasurface which yields a resonant wave pattern on the far-field.

2.4.1 Off-resonant interactions

The off-resonant interactions between the metasurface and the light are shown in Fig. 2.4 (a) in two dimensions. When the light incidents on the metasurface, depending on λ_{exc} and the size of the nano-features of the metasurface, off-resonant interactions emerge. Although dielectric materials are nearly lossless optical materials compared to metals, they can absorb incident photons if their energies are within absorption band of a dielectric material [99]. When a light beam incident on metasurface with electric field amplitude E_0 in Fig. 2.4 (a), metasurface response is similar to dielectric grating, some of the light intensity reflected as R_0 and transmitted as T_0. R_0 and T_0 are also known as zeroth reflection and transmission or directional reflection and transmission. Besides R_0 and T_0, the metasurface diffracts the incident light into its constituting colors (or wavelengths). The diffraction orders propagating on *x-z* plane are shown as R_1 and R_2 and T_1 and as T_2 for the propagation on *(-x)-z* plane in Fig. 2.4 (a).

2.4.2 Leaky modes

The unique difference between a two dimensional PhC in Fig.2.1 (a) and two dimensional PhC slab Fig.2.1 (b), here dimensional refers to periodically changing dielectric constant in two spatial dimensions, is that the PhC slab has radiation modes which channel the light outside of the slap over and below the slab [71]. These mode solutions are called leaky modes or guided mode resonance, referring to their ability to channel the coupled EMW out of the dielectric slab [69]. The modes are a member of on-resonant interactions, which is illustrated in Fig. 2.4 (b). When the EMW couples with these modes, depicted as black arrows on z-axis in Fig. 2.4 (b), they can channel through $\pm$ x-direction. The energy of the coupled mode slowly leaked out of the dielectric structure. These modes are called leaky modes, which are associated with complex frequency solutions of the Eqn. 2.10 [69]:

$$\omega = \omega_0 - i\gamma$$

where ω_0 is the real valued eigenvalue and γ gives the leakage rate of the coupling. The leaky modes can originate from various effects as a result of interference: guided wave resonance, diffraction, and coupling of in-plane component of the EMW incident on metasurface [69, 100]. A more realistic example of a metasurface based on a PhC slab on a substrate is illustrated in Fig. 2.1 (d). One of the important influences of the substrate under the metasurface is the breaking of the mirror symmetry in the z-direction, which introduces new channels for light to couple out a metasurface. Nevertheless, the leaky mode in Fig. 2.4 (b) can interfere with incident E_0 and yield a resonance pattern on measured spectra of zeroth-order reflection R_0 and T_0 in far-field [106]. Moreover, the EMW energy density carried by leaky mode exponentially decreases away from the metasurface [104]. On the other hand, coupling of the leaky modes with external radiation yields a strong near electric field in close vicinity of the metasurface [58].

2.4.3 Bound states in continuum

Bound states in continuum (BIC) are described as discrete states existing inside a continuum of radiation states, contrary to leaky modes, they are localized modes [107]. Despite their resemblance, a BIC exhibits no leakage, their leakage rate $\gamma = 0$ [108]. Therefore, they are forbidden to couple with external radiation [107].

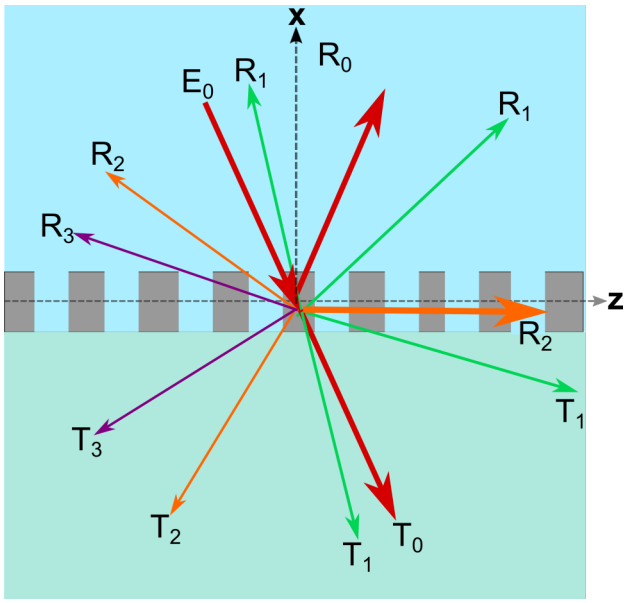

Figure 2.5: Rayleigh-Wood anomaly in metasurface: The intensity of the incident light denoted with E_0 while the directional reflection and transmission are represented by R_0 and T_0. The higher order reflection and transmissions (diffraction orders) are indicated with indexed T and R.

With this aspect, they can be considered off-resonant interactions. The symmetry-protected BICs exist in extended structures containing rotational symmetries on the *x*-*y* plane at the Γ point of the Brillouin zone of PhC slabs and metasurfaces. The external radiation incident on the metasurface cannot be coupled with a BIC. However, when the symmetry is broken, i.e. EM radiation inclines on the metasurface at oblique angles or structural imperfection that breaks 180° rotational symmetry on *x*-*y* plane, those localized states can radiate through to space, which eventually becomes a leaky mode [109].

2.4.4 Rayleigh-Wood anomaly

Rayleigh Wood anomaly can be observed when external radiation is diffracted by the metasurface at such an angle that the diffraction angle of the diffraction order is orthogonal to surface normal, hence, the diffracted in plane wave experiences periodic dielectric constant exhibited by the metasurface [81]. This effect is illustrated in Fig. 2.5. The diffraction order R_2 propagates along the metasurface by dissipating its energy in *z* direction, exhibiting evanescent wave nature. The condition for

Rayleigh-Wood's anomaly is given by the diffraction grating equation [110]:

$$n_1 sin(\beta_m) = n_3 sin(\theta) \pm \frac{m\lambda_0}{p} \tag{2.15}$$

Where m is the diffraction order, β_m and θ are the angle between surface normal and the wavevector of the m-th order diffraction. The condition for Rayleigh-Wood anomaly is β_m = 90°,then Eqn. 2.15 in terms of angle of incidence for the anomaly becomes:

$$\theta = sin^{-1}\left[\left(\frac{1}{n_3} n_1 \pm \frac{m\lambda_0}{p}\right)\right] \tag{2.16}$$

Eqn. 2.16 is the solution for a one-dimensional photonic structure, however, the principles can be easily expanded for the Si metasurface in two dimensions.

3 Fundamentals-II: Photon Upconversion

3.1 Light Absorption and Electronic Transitions

3.1.1 Light absorption and emission by an atom

Light absorption is a result of the interaction of light (photons) and matter in which the energy of the photons is transferred to matter. For example, an electron inside the matter can increase its energy by absorbing the energy of a photon. As a result of this interaction, an electron is excited and the photon is annihilated. When the electrons are bounded to an atom, the quantum nature of such a system dictates that the electron can exist in a bound state with a specific energy value. A hypothetical yet intuitive example is shown in Fig. 3.1 in which an electron is bounded to an atom that has two energy levels. The E_1 is the lowest energy state

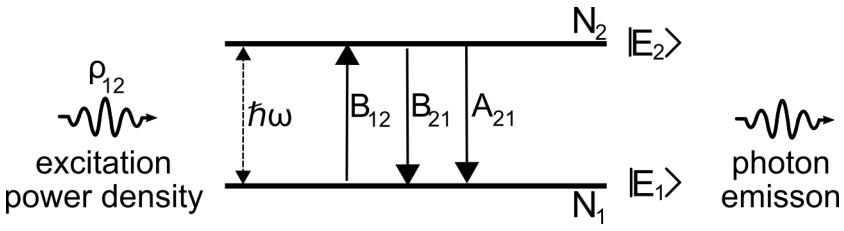

Figure 3.1: Light absorption and emission by a two-level system. The solid arrows which are labelled with Einstein coefficients B_{12}, B_{21} and A_{21} represent electronic transitions; photon absorption, stimulated and spontaneous emission while the dashed double-sided arrow shows the energy difference $\hbar\omega$ between the energy levels E_1 and E_2. The excitation power density that can bridge the energy gap between the ground state and excited state with photons with angular frequency of ω denoted as ρ_{12}

(or equivalently called as ground state) which is the electronically stable state, and E_2 is the excited state which can be occupied by an electron after absorption of a photon. In such an isolated atom, not all the photons can provide the electronic transitions but the ones which can bridge the energy difference between the ground and exited state ; $\hbar\omega$, and satisfy momentum conservation. These requirements will be discussed later in this chapter in the context of selection rules for electronic transitions. The electronic transitions between two energy levels in Fig. 3.1 are governed by transition probabilities. The electronic transition probabilities on such an atom are given by Einstein coefficients [111, 112]:

$$\frac{\mathrm{d}N_2}{\mathrm{d}t} = \rho_{12}(\omega)B_{12}N_1 - \rho_{12}(\omega)B_{21}N_1 - A_{21}N_2 \tag{3.1}$$

The Eqn. 3.1 is known as the rate equation which gives the rate of change of the population density ($1/m^3$) of the energy level-2 by time. $\rho_{12}(\omega)$ (J/m^3) is the incident electromagnetic energy density on the two-level system, and indices '12' indicate that it is the energy density that can bridge the energy gap between the two energy levels. The Einstein coefficients B_{12} (m^3/J.s), B_{21} (m^3/J.s), and A_{21} (1/s) give the ground state absorption, simultaneous emission, and spontaneous emission probabilities. A_{21} can be expressed in terms of electronic transition probabilities W_{12} (1/s) by using tools of quantum electrodynamics. The electronic transitions are given by Fermi's golden rule as following [111, 112]:

$$W_{12} = \frac{2\pi}{\hbar}|M_{12}|^2 g(\hbar\omega) \tag{3.2}$$

where $|M_{12}|$ and $g(\hbar\omega)$ are the matrix element of the transition between two energy levels and the density of the electronic states at the second energy level, while $\hbar$ (J.s) is the reduced Planck constant. The matrix element can contain various interactions [113]. If light is considered as classical electromagnetic waves and electrons as quantum particles, the interactions between light and atom can be approximated as an electric dipole or quadruple [111]. However, higher-order electromagnetic interactions such as quadruple interactions have lower transition probability than the dipole transitions [114]. In specific cases, electronic transitions can be approximated to dipole transitions [111]. Therefore, for the rest of the monograph, the interactions between light and matter are assumed to be electric dipole interactions. In this case, the matrix element simplifies to $M_{12} = -\mu_{12} \cdot \mathbf{E}$ where the $\mathbf{E}$ and

μ_{12} are the electric field and dipole moment. The Einstein coefficients for absorption and spontaneous emission are given by [111, 112]:

$$B_{12} = \frac{\pi}{3\epsilon_0\hbar^2}|\mu_{12}|^2 \tag{3.3}$$

and

$$A_{21} = \frac{\omega^3}{3\pi\epsilon_0\hbar c^3}|\mu_{12}|^2 \tag{3.4}$$

where ϵ_0 is the electric permittivity.

3.1.2 Term symbols and selection rules for dipole transitions

An atom can have many energy levels whose quantum state $|J,L,S\rangle$ can be expressed by its quantum numbers where J, L, and S are total angular momentum, orbital angular, and spin quantum numbers. This state can be expressed with the term symbols which are conventionally used in spectroscopy [115]:

$$^{2S+1}L_J$$

L is designated by alphabetic characters S (L = 0), P (L = 1), D (L=2), and F (L = 3), and the rest follows alphabetically. For example, an Er^{3+} ion at its ground state can be expressed as:

$$^4I_{15/2}$$

which means that the ion in this state has total L = 6, S = 3/2 and J = 15/2. The spin multiplicity, $2S$+1 = 4, means that it's a quartet state, by Hund's rule, the ion has 3 unpaired electrons.

The Einstein relations explains electronic transition between two energy level successfully. However, not all radiative transitions are possible in a multi-level energy system. The quantum nature of the light-matter interactions restricts radiative transitions. These transitions follow a set of rules which are so-called *selection rules*. These rules depend on the type of transitions. For example, the parity of a wave function of an atom changes for a dipole transition while quadruple transitions require even parity. The rules that describe allowed transition are based on the fact that a photon carries an integer spin angular momentum $\pm\hbar$ and the electric dipole moment is an odd function of the distance between electric poles [111, 112]. An electronic dipole transition between two enery levels $^{2S+1}L_J$ and

$^{2S'+1}L'_{J'}$ levels must obey selection rules below [111]:

1) $|L - L'| = 0, \pm 1$

2) $|J - J'| = 0, \pm 1$

3) $|S - S'| = 0$

In addition, the transition for $L = 0 \rightarrow 0$ and $J = 0 \rightarrow 0$ is forbidden for a dipole transition [111, 112]. This means that no radiative transition between the sub-levels is possible. Above mentioned selection rules are only valid for dipole transition in which an atom is approximated as an oscillator.

The transition between the states which cannot satisfy selection rules is called forbidden transition. Their probabilities are very low and require some internal conversion of the spin state of the electron or spin interaction between two atoms or molecules [116]. For example, although the third selection rule strictly forbids the change of spin multiplicity in a dipole transition, the spin multiplicity (i.e. relaxation to triplet state to singlet state) can change via an intermolecular spin change process which is called *inter-system crossing* [117].

The selection rules that govern dipole transitions are effective in explaining the spectrum of atomic and solid-state materials. However, they can fail to explain some of the transition when an ion embedded in a crystal host. For instance, they are unable to account for the photoluminescence spectra of rare-earth elements in crystal hosts, as these elements exhibit dipole transitions that are forbidden. Rare-earth elements are typically found in their 3+ oxidation state (Re^{3+}), with valence electrons occupying a $4f^n$ atomic shell that is shielded by 5d orbitals [118]. This leads to weak interaction with the environment and little involvement in chemical interactions. However, they are still sensitive to the crystal field and can exhibit a mixing of orbital (f-d orbitals), making some dipole-forbidden processes weakly allowed [118]. Re^{3+} ions often display spin and dipole forbidden transitions with low emission intensities in their emission spectra [119, 120]. In such cases, the selection rules for dipole transitions in Re^{3+} in a crystal host are modified by the Judd-Ofelt theory [119–121]:

1) $|L - L'| \leqslant 6$

2) $|J - J'| \leqslant 6$

3) $|S - S'| = 0$

4) parity of the wavefunction : opposite

In molecular or atomic systems, there may be numerous energy levels, including

those between the excited and ground states. If a transition from an excited state to lower states is weakly allowed or forbidden, electrons may take a long time to relax to the ground state, resulting in states with lifetimes up to several milliseconds. These states are known as metastable states, and the corresponding energy levels are referred to as metastable energy levels.

3.1.3 Electronic transitions and light absorption by many atom systems

The many atoms systems can be macroscopic media such as crystalline state material or disordered media with light absorbing centers. As shown in Fig. 3.2, a macroscopic medium with a length of d is a prime example. A beam of light with an intensity of I_0 must enter the absorbing medium without reflection. As the light travels through the medium with a thickness of d, some of its intensity is absorbed by the atoms or molecules within it. To calculate the intensity of the transmitted light through the medium, the Beer-Lambert law must be utilized [122]:

$$I = I_0 e^{-\alpha d} \tag{3.5}$$

where α is the absorption coefficient (1/m). The absorption coefficient is related to the density of the atoms or molecules N in a medium and absorption cross-section which is a measure of how well a medium absorption light with specific angular frequency ω [113].

$$\alpha(\omega) = N\sigma(\omega) \tag{3.6}$$

The absorption cross-section $\sigma(\omega)$ (m^2) is a function of ω (or equivalently λ, $\lambda = {}^{2\pi c}/_{\omega}$) because energy levels of the atoms or molecules can split into many sub-levels, therefore, the light absorption by the medium does not occur only at a specific wavelength. The absorption occurs over a spectral band which includes the electronic transitions between sub-levels of the two energy levels. For example an electronic transition between $^4I_{15/2}$ and $^4I_{13/2}$ requires absorption of a photon with wavelength of 1532 nm while a crystal containing many Er^{3+} can absorb photons with wavelength between 1400 nm and 1600 nm [31]. This results in an absorption band of wavelengths.

The photon absorption probability of an atom can be related to Einstein coeffi-

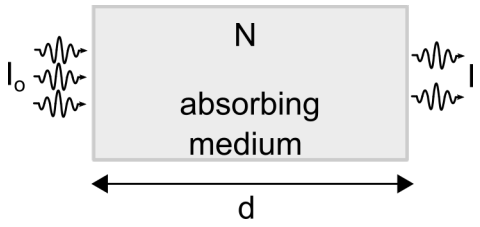

Figure 3.2: Light absorption by a macroscopic media: A light beam with intensity of I_0 is incident on the absorbing medium with thickness of d. I_0 is partially absorbed by the ions with density of N in the medium.

cients. This relation is can be expressed as [123]:

$$\sigma(\omega) = \frac{\hbar\omega}{I} B_{12} \tag{3.7}$$

In this case, the absorption rate R is given by [31, 124]:

$$R = B_{12} N_0 \tag{3.8}$$

By combining Eqn. 3.7 Eqn. 3.8 the absorption rate can be expressed as [31, 124]:

$$R = \frac{\sigma(\omega)}{\hbar\omega} I N_0 \tag{3.9}$$

In general for a material with linear dielectric properties, the absorption rate between an energy level n and m can be written as [31, 124]:

$$R_{m\to n} = \frac{\sigma_{mn}(\omega)}{\hbar\omega} N_m P_{exc} \tag{3.10}$$

where $R_{m\to n}$, $\sigma_{mn}(\omega)$ and N_m are the absorption rate and absorption cross-section of the dipole transition from m-th state to n-th state, the population density of the m-th state, respectively.

3.2 Basic Elements of Photon Upconverison

The UC is a three-step process: absorption of the two photons by upconverting material, conversion of the two-photon energy into a single photon, and the emission of a single photon with higher energy than one of the initial photons. An atomic or molecular system with at least three energy levels is needed, yet not every atom

or molecule possesses UC. The energy difference between the energy levels should be comparable so that at least two photons can be successfully absorbed. Moreover, these energy levels should be meta-stable so that the excited electrons can have a chance to interact with other photons or electrons before it relaxes back to their ground state [125].

UC can be achieved through various processes. The most basic yet most probabilistic two UC processes of a 3-level atom (or molecule), excited state absorption UC (ESA-UC) and energy transfer UC (ETU) are shown in Fig. 3.3 (a) and (b).

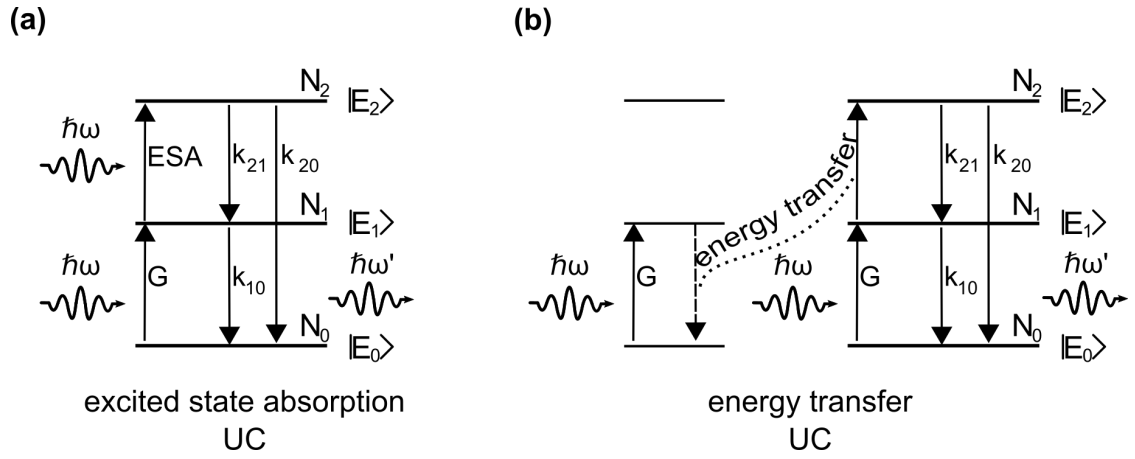

Figure 3.3: Selected radiative processes of photon upconversion: (a) Excited state absorption (ESA) upconversion and (b) energy transfer upconversion (ETU). The allowed radiative transitions and electron excitation to higher energy levels are shown as solid arrows. The non-radiative transitions are shown by dashed arrows.

3.2.1 Ground state absorption

The ground state absorption occurs when an electron in the E_0 state in Fig. 3.3 (a) and (b) is excited to the E_1 state by absorption of a single photon [126]. The GSA of electrons is shown by upright arrow express the electronic transition ($|E_0\rangle \rightarrow |E_1\rangle$) from the ground state $|E_0\rangle$ to first excited state $|E_1\rangle$ in Fig. 3.3 (a) and (b). The generation rate G (1/s) gives the number of electrons from ground state $|E_0\rangle$ to excited state $|E_1\rangle$ per unit time. G is related to the ground state absorption probability given by Eqn. 3.10 [31]:

$$G = \frac{R_{0\rightarrow 1}}{N_0} \tag{3.11}$$

where N_0 and $R_{0\rightarrow1}$ are the number of the electrons in the ground state and the absorption probability of the electrons in the ground state. $R_{0\rightarrow1}$ is [31, 124]

$$R_{0\rightarrow1} = \frac{\sigma_{01}(\omega)}{\hbar\omega} N_0 P_{exc} \tag{3.12}$$

where the absorption rate is in the units of ions/s·m^3. The P_{exc} and $\sigma_{01}(\omega)$ are excitation (or pump) power density and absorption cross-section of the $|\text{E}_0\rangle \rightarrow |\text{E}_1\rangle$ transition, respectively. $\sigma_{01}(\omega)$ is given as the function of the frequency of the absorbed photons and P_{exc} is assumed to consist of monochromatic photons with energy of $\hbar\omega$. Moreover, P_{exc} is assumed to have uniform spatial distribution. Furthermore, σ_{01} also depends on the frequency (or wavelength) of the photons within the absorption band of the ground state and its value is unique for every atom or molecule. The G for GSA can be expressed as [31]:

$$G = \frac{R_{0\rightarrow1}}{N_0} = \frac{\sigma_{01}(\omega)}{\hbar\omega} P_{exc} \tag{3.13}$$

The GSA can occur through any of the states as soon as the energy of the absorbed photon can satisfy the energy difference between the ground state and the one of excited states. Eqn. 3.12 can be generalized for any two allowed electronic transitions between two energy levels $|\text{E}_m\rangle \rightarrow |\text{E}_n\rangle$. Then, generalized generation rate can be written as:

$$G = \frac{\sigma_{0m}(\omega)}{\hbar\omega} P_{exc} \tag{3.14}$$

a where σ_{0m} is the absorption cross-section of the $|\text{E}_0\rangle \rightarrow |\text{E}_n\rangle$ transition. To sum up, GSA depends on the number of photons per second incident on upconverting material and the ability of the ground state to absorb the energy of the photon to achieve an electronic transition to a meta-stable state.

3.2.2 Excited-state absorption

Excited-state absorption (ESA) is the absorption of a photon by an electron that has been already excited in a meta-stable state [126]. In other words, ESA is the electronic transition from an excited state to a higher energy state as a result of photon absorption. A schematic drawing of the ESA is shown in Fig. 3.3 (a). A photon excites the electrons on $|\text{E}_1\rangle$ to $|\text{E}_2\rangle$, which is labeled as ESA and represented by the upward solid arrow in Fig. 3.3 (a). The generation rate for the ESA E_{12} (1/s)

is by employing Eqn. 3.10 and 3.14 [31, 124]:

$$E_{12} = \frac{R_{12}}{N_1} = \frac{\sigma_{12}}{\hbar\omega} P_{exc} \tag{3.15}$$

the ESA generation rate can be generalized for the between n-th state ($n \neq 0$) and m-the state [31, 124]:

$$E_{nm} = \frac{R_{nm}}{N_n} = \frac{\sigma_{nm}}{\hbar\omega} P_{exc} \tag{3.16}$$

Similar to GSA, ESA also depends on the number of photons incident on upconverting material and absorption cross-section of the electronic transitions. The whole ESA process is completed in a single molecule or atom. Hence, the ESA process is independent of the density of the ions or molecules which are capable of UC.

3.2.3 Energy transfer

Energy transfer (ET) is an inter-ionic (or molecular) non-radiative resonant energy transfer process in which two electrons in separate atoms or molecules [127] interact with each others. Namely, at least two atoms or molecules with excited electrons are needed for the ET process, which is depicted in Fig. 3.3 (b). This means that the two atoms or molecules have to experience electron excitation processes such as GSA before ET. When the two atoms or molecules have a short intermolecular or inter-ionic distance, the electrons can exchange their energy. For example, ET in Fig. 3.3 (b) illustrated as a dotted curve which shows the non-radiative exchange between two electrons, the energy of the electron on $|\mathrm{E}_1\rangle$ state of the first atom or molecule relaxes back to its ground state by exciting the electron on the second ion from $|\mathrm{E}_1\rangle$ to $|\mathrm{E}_2\rangle$ state. Inter-ionic energy transfers are governed by Fermis's golden rule, and hence, a relation for the inter-ionic energy exchange rate W_{nm}^{ET} (m^3/s) for transition $|\mathrm{E}_m\rangle \rightarrow |\mathrm{E}_n\rangle$ is given by Frank-Condon approximation [128]:

$$W_{mn}^{ET} = \frac{2\pi C}{\omega^2 n^4 r_{1-2}^x} f_m f_n \int g_n(\omega) g_m(\omega) \mathrm{d}\omega \tag{3.17}$$

where C, ω, f_m, and f_n are constant term, frequency, and electronic oscillator strength for the first and second ion, respectively. The integral term $\int g_m(\omega) g_n(\omega) \mathrm{d}\omega$ in Eqn. 3.17 is the spectral overlap integral of the first and the second ion. The most important outcome of the Eqn. 3.17 is that the inverse power dependence of the W_{12}^{ET} on x-th power of the inter-atomic distance r_{1-2}, which can take values 6

or 8 or 10, limits the effectiveness of the transfer rate in short inter-ionic distances. The x takes values of 6 for an electric dipole-dipole interaction in the ET process between two ions [125]. This implies that the W_{12}^{ET} is strongly inter-atomic distance dependent for dipole-dipole interactions:

$$W_{ET} \propto r_{1-2}^{-6} \tag{3.18}$$

The ET strongly depends on the density of the molecules or ions in a medium since the average inter-ionic or inter-molecular distance is determined by the distribution of the ions of the in the host medium.

3.2.4 Multi-phonon relaxation

Phonons, which are quantized crystal lattice vibrations, can interact with electrons (by absorption and emission). A phonon is characterized by a wave vector 'k_p' and vibrational energy '$\hbar\omega$' along the crystal lattice. The energy of a phonon can be absorbed by an electron such that the electron can experience an electronic transition to a higher energy state or an electron can relax to a lower energy state by emitting phonons to bridge the energy gap between two states. However, this phonon assistance depends on the density and frequency of the phonons which are available within the crystal hosting the atoms or molecules. Considering an electron at an energy level described by spectroscopic term symbol $^{2S+1}L_J$, an electronic transition between $^{2S+1}L_J$ state and $^{2S^{'}+1}L_{J^{'}}$ can be bridged by a phonon or multiple phonons only if the condition is satisfied for an even integer ζ such that [111]:

$$|J - J^{'}| \leq \zeta \leq |J + J^{'}| \tag{3.19}$$

When the energy gap is greater than single phonon energy '$\hbar\omega$', the energy difference can be bridged by the simultaneous emission of multiple phonons. The non-radiative electronic transition assisted by multiple phonon emission, illustrated in Fig. 3.4 (a), between two subsequent energy levels is called a multi-phonon relaxation (MPR) process. Assuming that the condition imposed by the Eqn. 3.19 is satisfied for the transition $|E_2\rangle \rightarrow |E_1\rangle$, the temperature-dependent probability of MPR is given by [129]:

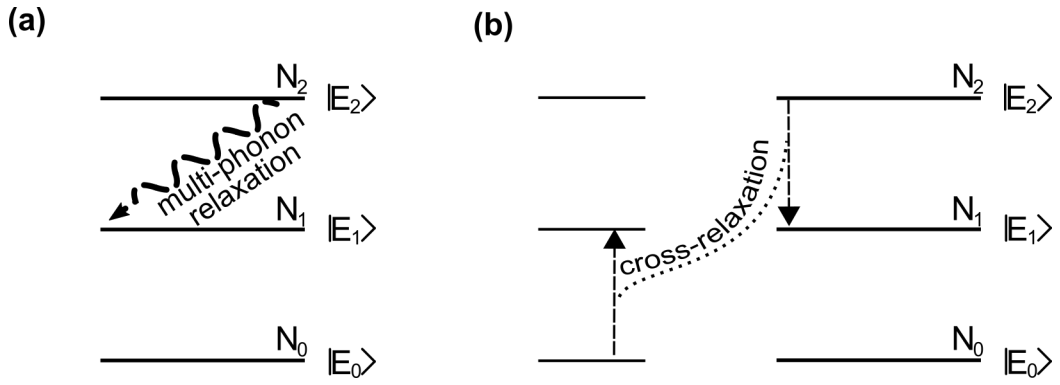

Figure 3.4: Selected non-radiative processes of the photon upconversion: (a) Multi-phonon relaxation and (b) cross-relaxation. The phonon involving non-radiative transition is represented dashed curled arrow while the non-radiative energy transfer process is shown by dashed straight arrows.

$$W^{MPR}_{|E_2\rangle\rightarrow|E_1\rangle} = W_0\left[1-\exp\left(-\frac{\hbar\omega}{k_B T}\right)\right]^{-n} \tag{3.20}$$

where W_0 (1/s), k_B and T are low-temperature related constants, Boltzmann constant and temperature (°K), while n is the number of the phonons with frequency of ω related with energy gap between $|E_3\rangle$ and $|E_2\rangle$:

$$n = \frac{E_2 - E_1}{\hbar\omega} \tag{3.21}$$

Eqn. 3.20 assumes the interaction of electrons with phonons with a single frequency. However, most of the crystalline solids exhibit multiple lines or bands of phonon emission and absorption [130]. Many experimental studies show that the MPR is dominated by phonons having a maximum frequency within the phonon spectrum of a crystal. Moreover, *energy-gap-law* relates the MPR rate to the maximum phonon frequency of a crystal host [130]:

$$W^{MPR}_{|E_2\rangle\rightarrow|E_1\rangle} = B\exp\left(-\alpha\frac{E_2 - E_1}{\hbar\omega_{max}}\right) \tag{3.22}$$

Here, B and α are the material and crystal lattice-depending constants, respectively. A strong dependence of $W^{MPR}_{|E_2\rangle\rightarrow|E_1\rangle}$ appears on the energy difference between the two subsequent energy levels, E_1 and E_2, and maximum phonon energy ω_{max}, which restrict to the probability of the MPR to specific crystal structure and materials.

3.2.5 Cross-relaxation

Cross-relaxation (CR) is an inter-ionic (or molecular) non-radiative resonant energy transfer process, similar to ET where two electrons in the separate atoms exchange their energy [127]. CR process for the 3-level system is shown in Fig. 3.4 (b). In the beginning, one electron is at the excited state E_2 of the second atom while a second electron occupies the ground state of the first atom. The electron at the ground state is excited to E_1 state while the electron is in the E_2 of the second atom. The excited electron and the relaxed electron are connected with a dotted curve in Fig. 3.4 (b) to explain the transitions. The CR can be considered as the reverse process of the ET in which the direction of the electron transitions is flipped. Therefore, the requirements and the rules for ET imposed by Eqn. 3.17 also apply to the CR process.

3.3 Rate Equations for Upconversion

The rate equation in the Eqn. 3.1 gives the rate of change of the population density of an energy level. Spontaneous and stimulated emission from this level decreases the population density of the level while excitation of the electrons to this state increases its population density. The solution of the rate equation for spontaneous emission after excitation gives the radiative lifetime of a transition [111]:

$$N_n(t) = N_n(0)e^{-\frac{t}{\tau}} \tag{3.23}$$

where τ is the radiative lifetime of the emission which is related to the radiative transition probability of the transition from a state m to another state as $k_{mn} = \tau^{-1}$. $N_n(t)$ and $N_n(0)$ in Eqn. 3.23 are the population densities of the level at the beginning and at time t. One of the outcomes of the Eqn. 3.23 is that after the excitation of electrons to N_2 level, electrons in this state exponentially decay to the lower states.

In reality, both radiative and non-radiative processes can be observed at the same time. Such a system is depicted in Fig. 3.5 which has their energy levels. Rate equation for each energy levels in Fig. 3.5 can be written as [31, 124, 131]:

$$\frac{\mathrm{d}N_0}{\mathrm{dt}} = -GN_0 + W_{ET}N_1^2 - W_{CR}N_1N_2 + k_{10}N_1 + k_{20}N_2 \tag{3.24}$$

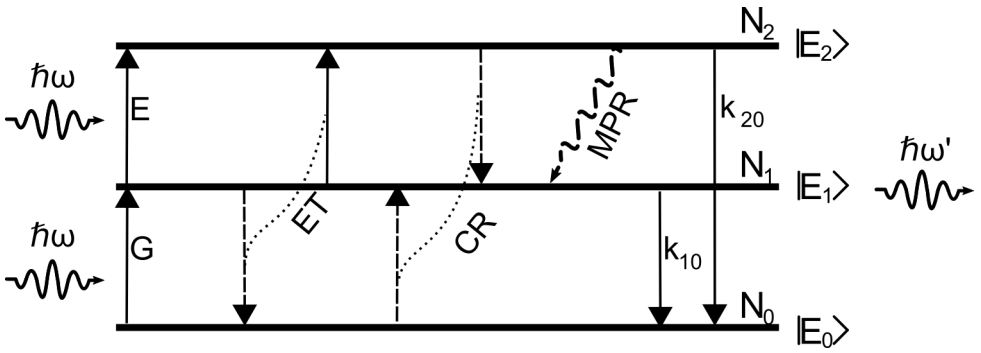

Figure 3.5: Energy level diagram of a system of many atoms and upconversion processes. The direction of the arrow indicates the exaction and relaxation routes for the electrons occupying the energy levels. Non-radiative pathways are shown as dashed curves and lines.

$$\frac{\mathrm{d}N_1}{\mathrm{dt}} = GN_0 - EN_1 - 2W_{ET}N_1^2 + 2W_{CR}N_1N_2 + W_{MPR}N_2 - k_{10}N_1 \tag{3.25}$$

$$\frac{\mathrm{d}N_2}{\mathrm{dt}} = EN_1 + W_{ET}N_1^2 - W_{CR}N_1N_2 - W_{MPR}N_2 - k_{20}N_2 \tag{3.26}$$

The population densities of the energy levels can be found by the steady-state solution of the Eqn. 3.24-3.26 when the $\frac{\mathrm{d}N_m}{\mathrm{dt}} = 0$. This condition can be satisfied when the UC material is excited with a continuous wave laser under equilibrium conditions. In this case, the experimental results of an UC experiment can be explained by the steady-state solution of the rate equation of the UC system since the spontaneous emission rate is related to UC emission: $I_{\mathrm{UC}} \propto k_m N_m$ in Eqn. 3.24-3.26. A relation which is called as *power-law* relates the intensity of the UC emission intensity and the P_{exc}:

$$I_{UC} \propto P_{exc}^n \tag{3.27}$$

where I_{UC} is the intensity of the UC emission. Eqn. 3.27 reflects the non-linear nature of the UC process such that I_{UC} depends on n-th power of P_{exc}. Depending on the minimum number of absorbed photons to achieve UC emission, n takes integer values. For example, for 2 photon UC, n takes a value of 2 while for 3 photon UC, n takes a value of 3. The power law is an intuitive and empirical relation that is valid when the intensity of the UC emission is significantly smaller than the P_{exc} and the density of the emitter N is substantially low so that the probability of the inter-ionic interaction is not strong [31].

4 Experimental and Computational Methods

4.1 Si Metasurface Fabrication

Si metasurfaces are produced by a two-step bottom-up approach. The first step is to produce nanostructures with soft-nanoimprinting lithography. The second step is the fabrication of the Si metasurfaces on the nanostructures. Both steps are completed in a clean room environment. The nanoimprinting technique and Si metasurface fabrication will be discussed in the following two sub-sections in detail.

4.1.1 Nano imprinting lithography

Lithography is one of the driving forces behind semiconductor device technology; especially very-large-circuit-integration (VLSI) technology [132]. The techniques and the methods of lithography have flourished with record development pace un-

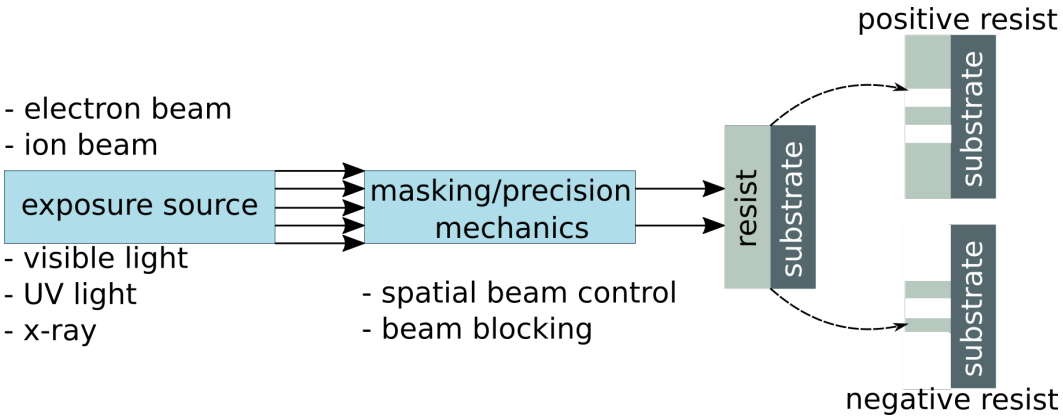

Figure 4.1: Components of a typical lithography system.

der the pressure imposed by the microelectronic industry, which is the requirement of scaling down the microelectronic units so that the electronic unit per wafer can increase [133]. In addition to being the driving force behind integrated electronics, lithography tremendously reduced the production costs of wafer-based electronic devices in the last few decades [133–135].

The advances in lithographic technologies for the production of sub-micron features with great precision on semiconductor wafers facilitated to development photonic components with feature sizes comparable with visible light wavelengths. The requirement for precise feature forming and high throughput production led to the development of various lithography techniques [136].

A conventional lithography system is shown as a diagram in Fig. 4.1. A typical lithography system uses an exposure source, which interacts with matter and forms the structures at the later stages of a lithography process. Exposure sources vary and the lithography techniques are named after them. For example, a lithography method in which the materials are exposed thermally, by a heated tip, is called thermal scanning probe lithography [137]. The output of the exposure source is projected on the sample and it creates the desired pattern on the sample. This can be achieved through precise control of the spatial position of the beam by a computer-aided system. Another way to pattern the sample is by partially blocking the exposure with a mask. The desired pattern can be placed between the exposure source and the substrate which is generally not created directly on the sample. The pattern forms on a kind of special layer, which is covered on a substrate surface, generally, via spin-coating. These chemicals can be either photo- or thermoactive materials or they can be sensitive to ion and electron beam exposure. These layers experience a change in their chemical composition or their structural state after exposure which enables them to transfer or form a pattern. In lithography terminology, these chemicals are called resists. If a resist experiences a chemical or structural change after light exposure, it is named photo-resist. Similarly, the resists which are chemically active under an electron beam (e-beam) are referred e-beam resist. The exposed resist layer is processed with other chemicals or by physical methods, which is called development, to form the final structure on the substrate. There exist two different kinds of resist depending on the behavior of the resist at this stage as shown in Fig. 4.1: positive and negative resists. The unexposed areas of the resist layer are removed for a positive resist, in contrast, the exposed areas are removed by development for a negative resist.

The most common lithography techniques for micro and nano feature production are ion-beam lithography, electron beam (e-beam) lithography, X-ray lithography, extreme ultraviolet (EUV) lithography, and optical lithography [136]. These lithographic methods have proven that they are even able to produce nanostructures with feature sizes less than 10 nm [138]. Although conventional lithography techniques enable precise control of nano-feature size and shape, the number of available photo-resist or e-beam resist and their applicability on different materials and material surfaces limits their applicability. For example, the lithography techniques listed above give desired shape and feature sizes on the flat semiconductor surface, however, they can fail to form nanostructures, especially periodic patterns, on organic materials or uneven surfaces, such as plastic substrates or curved surfaces [139].

The necessity for patterning on different substrates and uneven surfaces led to the development of a set of more versatile lithography methods, which are collectively referred to as soft-lithography, based on elastomeric materials such as widely used polydimethylsiloxane (PDMS) [140]. The patterns are transferred on resist-coated substrates by embossing, imprinting, or molding [141]. The main advantage of soft-lithography is its ability to transfer patterns with high throughput and less production cost compared to conventional lithography techniques [139]. On the other hand, the transferred patterns by soft-lithography are needed to be produced by conventional lithography techniques [141, 142].

Soft nanoimprinting lithography (s-NIL) is one of the members of the soft lithography methods that enables thousands of replication, consequently mass production, of sub-micron features in a cost-effective way [143]. In recent years, it has been shown that even sub-10 nm nano-features with high-aspect-ratio can be produced by the s-NIL method [144]. The s-NIL process is depicted in Fig. 4.2 (a)-(g) based on a previously well-established recipe [145–147]. As a starting point for s-NIL, a previously produced template or master structure is required. Si nano-pillar arrays with hexagonal lattices on Si wafers are fabricated by Eulithia AG with the ultraviolet interference lithography method for this study. These nanostructured wafers, so-called master structures, are used as templates for s-NIL. Hundreds of copies of the nanostructures can be copied from the master structure and transferred to other substrates. s-NIL of the nanostructures starts with the preparation of the mold material, which will serve as a stamp with the negative image of the nano-features of the master structure. PDMS is preferred as a molding material

for this study owing to its low-temperature curability [148]. The preparation of the PDMS molds is done by cross-linking its base polymer (Wacker) and its curing agent (Wacker). Both the base and curing agent are kept at room temperature. The PDMS base and its curing agent are mixed in a 9:1 ratio in a glass container. The mixture was stirred well until the base polymer and curing agent mixed homogeneously. Air bubbles are generated inside the mixture at this stage of the s-NIL process, which is a detrimental effect on the replication of the nano-structures from the master structure. The air bubbles must be taken out of the mixture before polymerization of the PMDS starts, hence, the PDMS mixture is immediately transferred to the vacuum box for degassing. Next, the degassed-air bubble-free PDMS mixture is poured over the master structures (Fig. 4.2 (a)). A few mm thick PDMS on master structures are cured at 90°C for 20 min (Fig. 4.2 (b)). During the heat treatment, the polymer cross-linking of the PDMS base occurs, resulting in a flexible solid PDMS mold, containing a negative surface image of the master structure (Fig. 4.2 (c)). Glasses (Corning Eagle) with dimensions of 1 mm x 5 cm x 5 cm are chosen as substrates for the meta-surfaces. All the glasses that are used in the experiments are subjected to lab-grade cleaning (Miele) with a lab-grade cleaning agent to prevent contamination for imprinting. A UV/Thermal curable sol-gel (Philips) is used as the imprinting fluid. It is compulsory to keep the sol-gel in a dark container and cool (<10°C) environment because of its easy curability. The temperature of the sol-gel in the experiment is adjusted to 23°C for consistency, i.e. for having the same sol-gel viscosity in each production bench, before proceeding further. However, the easy curability of the sol-gel can cause trouble after its temperature increase, for example, cured molecules in sol-gel can precipitate. The precipitate forms dust-like particles in sol-gel which lead to non-imprinted areas on the substrate at later stages of s-NIL. To avoid artifacts, the sol-gel is filtered to get rid of any small particles. Then, a buffer layer of sol-gel is spin-coated on the glass substrate by drop-casting 750 μL of sol-gel at a rotation rate of 17 rounds-per-second (rps) for 10 s. The presence of a buffer aims at two things. First, it stops the impurity ions emerging from the glass to reach layers deposited over the substrate at the later stage of the s-NIL. The second reason is the conformal coverage of the surface of the glass substrate so that the nano-features do not suffer local surface roughness of the glass surface. The imprinting fluid layer is formed on the buffer layer by spin-coating of 0.75 μL of sol-gel with a rotation rate of 10 rps for 30 s. Next, the PDMS mold is imprinted on the sample, and a gentle force is exposed by a rolling cylindrical mass on top of the PDMS mold to ensure

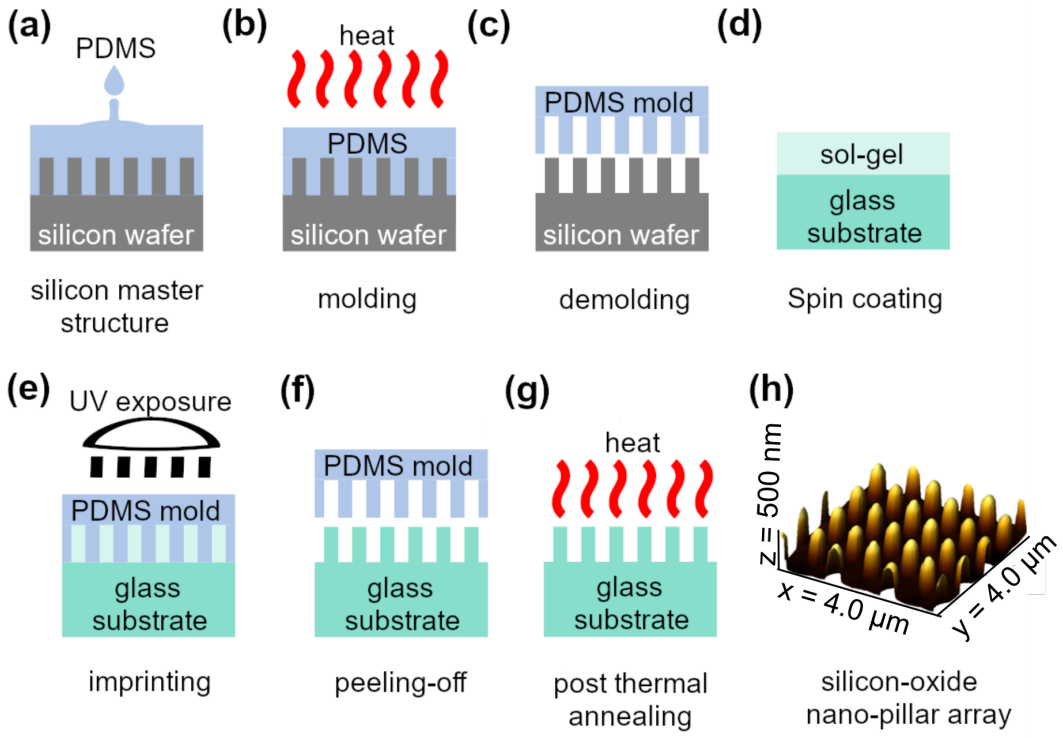

Figure 4.2: Process sequence for soft nano-imprinting lithography (a) PDMS pouring, (b) PDMS curing, (c) PDMS demolding, (d) sol-gel coating, (e) sol-gel curing, (f) Si oxide nano-pillars formation, (g) thermal annealing, and (h) an atomic force microscopy topographic image of Silicon-oxide nano-pillar array. Adapted from supporting information for Ahiboz *et al*. [79].

good contact between the mold and the imprinting fluid layer. While the sample and the mold are still in contact, the sample is exposed to UV radiation for 5 min (Fig. 4.2 (e)). After UV exposure, the both buffer layer and the imprinting layer get solidified, and transformed into Si oxide (Fig. 4.2 (f)). Although the nano-pattern of the master structure is successfully transferred onto a glass substrate at this stage, thermal annealing is needed for the sample to evaporate the excess solvent and firm the formed nanostructures. Therefore, the imprinted sample is annealed at 100°C for 8 min immediately after peeling off the PDMS mold (Fig. 4.2 (g)). The s-NIL process is finalized by post-thermal annealing of the sample at 600°C for 40 min to test the thermal stability, otherwise, cracks on the nanostructures can occur. The produced nanopillars are shown in Fig. 4.2 (h) as an atomic force microscopy (AFM) image. Before depositing the Si on the samples, surface analysis of all the samples is performed by the AFM system (Park System XE100). The surface of the pro-

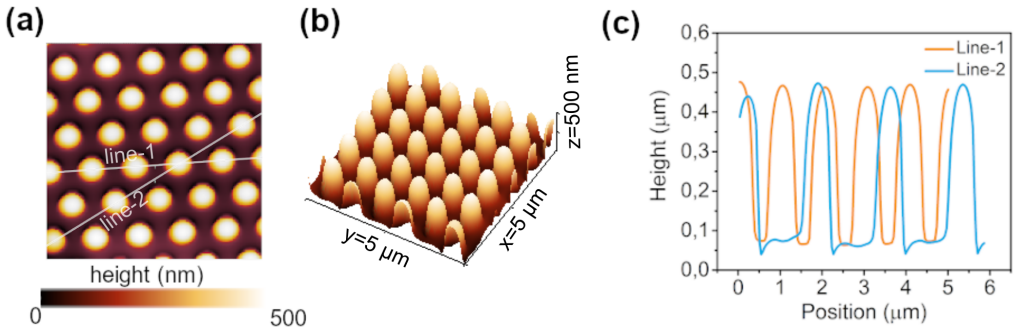

Figure 4.3: Surface analysis of the produced Si-oxide nanopillars on a glass substrate: (a) Two dimensional and (b) three-dimensional plot of the surface. (c) The thickness profile of the sample surface along the line through the first nearest neighboring point (line-1) and the second nearest neighboring point (line-2).

duced samples was analyzed in non-contact mode AFM. A high-resolution AFM tip that can probe the nanostructures with a great resolution scanned the surface of the samples. Two-dimensional surface topography and a three-dimensional surface plot are shown in Fig 4.3 (a) and (b). The period of the nanostructures is verified as 1000 nm. Two different lines, line-1, and line-2, in Fig 4.3(c) show two profiles towards two high symmetry directions of the hexagonal lattice. All the analysis of the AFM data was done by the AFM analysis software Gwyddion.

4.1.2 Si deposition

Si is chosen as a dielectric material for the fabrication of the metasurface owing to its superior material properties and well-developed and feasible production technology. Si has a refractive index n = 3.7 and n = 3.5 at the excitation wavelengths used in the experiments, λ_{exc} = 978 nm and λ_{exc} = 1550 nm, which creates a high refractive index contrast with glass-Si (0.40), air-Si (0.55) and UCNPs layer-Si interfaces (0.45) [149, 150]. Amorphous Si is deposited by a physical vapor deposition method (electron-beam evaporation) to form a Si layer on a glass substrate. The deposition of the amorphous Si is done in a vacuum chamber at 10^{-7} mbar pressure at 300 °C. The deposition process is illustrated in Fig. 4.4 (a). The amorphous Si layer deposited on the nanotextured glass substrate is shown in Fig. 4.4 (b). The process of the Si metasurface proceeds with the solid-state crystal-

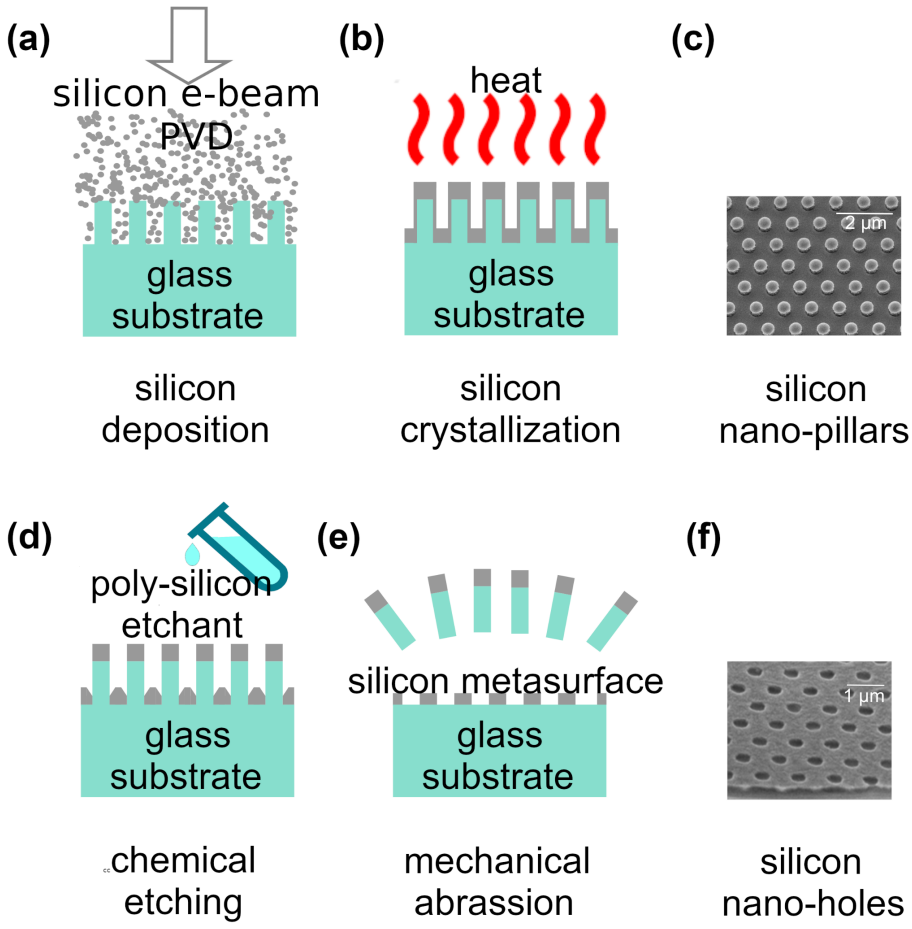

Figure 4.4: Process sequence for Si metasurface fabrication (a) Si deposition, (b) crystallization, (c) a scanning electron microscopy top-view image of the Si nano-pillars, (d) chemical etching of the non-crystalline Si residuals, (e) removal of the Si tips-Si oxide nano-pillars, and (f) a scanning electron microscopy top-view image of a produced Si metasurface. Adapted from supporting information for Ahiboz et al. [79].

lization of the amorphous Si layer on the nanotextured glass substrate in a quartz tube under nitrogen gas flow at 600°C (Fig. 4.4 (b)). The crystallization process was completed in three stages. First, the temperature of the sample ramped up 600°C in 6 h (approximately 1.6°C/min.) to avoid the thermal shock of the Si layer. Thermal shock can cause cracks in the Si layer. When the furnace reached 600°C the samples were left for crystallization at constant temperature (at 600°C) for 12 h. Then, the temperature of the samples ramped down to room temperature (approximately 1.6°C/min) under nitrogen gas flow. However, the Si layer around the Si oxide nano-pillars tends to stay in non-crystalline form [151, 152]. A scanning elec-

tron microscope (SEM) image of the Si deposited nanostructures on the glass substrate in Fig. 4.4 (c). This structure is called *double-layer Si metasurface* since the two distinct Si layers on the nanotextured glass can be defined: as Si nanodisks that are suspended by the nanopillars and low-lying Si layer on the glass substrate. A monolayer Si metasurface is created by the removal of the nano-pillars in two steps. After the crystallization step in (Fig. 4.4 (b)). The first etching step, which is a chemical etching, aims to dig trenches around Si nano-pillars. The double-layer Si metasurface is dipped into an electronic-grade (99.99 % pure) poly-Si etchant for 4 s. The chemical etching and the formed trenches are illustrated in Fig. 4.4 (d). The formation of the trenches between the Si layer and the Si nano-pillars enables the removal of the nano-pillars by mechanical abrasion, which is performed by sweeping lint and particle-free-laboratory-grade wiper on the double-layer Si metasurface (Fig. 4.4 (e)). At the end of this fabrication step, air holes instead of pillars on the Si surface are formed. As a result, double-layer Si metasurfaces transform into layer Si metasurfaces (For simplicity, Si metasurface refers to as monolayer Si metasurface in the rest of the monograph). An SEM image of the fabricated Si metasurface consisting of the nano-hole array on the Si layer is shown in Fig. 4.4 (f).

4.2 Synthesis and Deposition of the $NaYF_4$:Er^{3+} Nano Particles

Synthesis of the oleate capped β-$NaYF_4$:Er^{3+} nanoparticles were produced by Dr. Elina Andresen (Bundesanstalt für Materialforschung und -prüfung (BAM)), following the thermal-decomposition method demonstrated by Wilhelm *et al*. [153]. However, some modification is done to the procedure for large-scale synthesis of the nanoparticles. $YCl_3 \cdot 6H_2O$ (381.7 mg, 1.0 mmol) are sonicated in 15 mL of methanol. The obtained solution is mixed with 30 mL of oleic acid and 75 mL of 1-octadecene in a three-neck flask and stirred. The temperature of the mixture is raised to 150 °C under argon gas flow, while the mixture is stirred and the impurities in the mixture are boiled under vacuum pressure for 45 min. The lanthanide precursor-containing reaction mixture is then cooled down to room temperature under a constant argon flow. Afterward, a methanolic solution (30 mL) containing NaOH (500 mg, 12.5 mmol) and NH_4F (740 mg, 20 mmol) is added, and the resulting suspension is heated to 120 °C for 30 min to remove excess methanol. The reaction mixture is heated to

325 °C under reflux while applying a gentle flow of argon and kept at this temperature for 90 min. Then the reaction mixture is cooled down to room temperature and the nanoparticles are precipitated by ethanol and collected by centrifugation at 5000 round-per-minute (rpm) for 5 min. Then the NPs are re-dispersed in chloroform washed with ethanol several times and stored in cyclohexane (c = 30 mg/mL) at 4 °C.

The ratio of the Erbium doping is analyzed by inductively coupled plasma-optical emission spectrometry (ICP-OES) (Spectro Arcos). The Er^{3+} ions substitutes with Y ions in $NaYF_4$ crystals [125]. Therefore, the Er-to-Y ratio reveals Er^{3+} dopant ratio. The percentages of the Y and Er concentrations are determined as 74.2 ± 1.3 mol % and 25.8 ± 1.5 mol %, which are intentionally preferred for considering the Er^{3+} ratios demonstrated for solar cell applications in literature which is between 20 %, and 25 % of Er^{3+} content [33, 34].

The average size of the β-$NaYF_4$:Er^{3+} nanoparticles are calculated as 130 nm - 110 nm - 62 nm (width - depth - height) based on the TEM images, as depicted in Fig. 4.5.

The verification of the elemental composition of the produced nanoparticles is done by energy dispersive x-ray (EDX) spectroscopy.

The size and the shape of the produced nanoparticles are examined by a transmission electron microscopy (TEM) microscope (Thermo Fisher Scientific) and TEM images are shown in Fig. 4.5.

To get the elemental composition of the UCNPs, energy dispersive X-ray spectroscopy (EDX) with two Si drift detectors (SDD) is used during TEM analysis by Dr. Christian Würth and Dr. Elina Andresen. The counting time for the X-ray spectra is 60 s.

4.3 Optical Setups

Optical characterization and optical setup design are critical parts of this doctoral research project. Justification of the claims of this project, such as the presence of the leaky modes which enhance UC luminescence of the UCNPs, rely on optical detection of the light interacting with UCNPs and the leaky modes of the Si metasurfaces. Optical spectroscopy study of the metasurfaces, UCNPs, and their interactions are studied with two main spectroscopic systems. Before diving into the

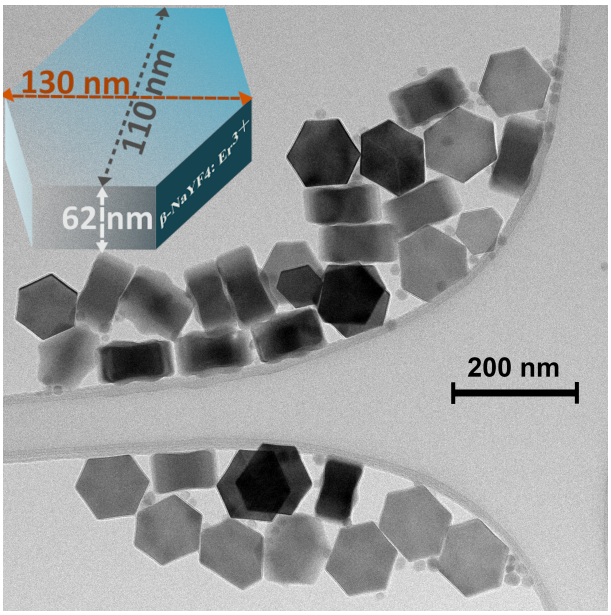

Figure 4.5: TEM image of the β-$NaYF_4$:Er^{3+}. Taken from Ahiboz *et al* [79].

spectroscopic methods that are subjected to this monograph, the general aspects of a spectrometer are summarized.

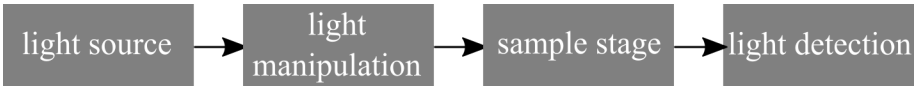

Figure 4.6: The four basic units of an optical spectrometer.

Spectroscopy is the study of light interacting with matter by decomposing electromagnetic waves into their wavelengths or frequencies. The series or collection of electromagnetic waves that are subject to spectroscopy is called a spectrum. A device designed for spectroscopy study is called a spectrometer, which allows us to investigate the spectrum of electromagnetic waves. A typical modern spectrometer consists of four main units; light source, light manipulation, sample stage, and light detection units which are shown in Fig. 4.6.

The light source can be monochromatic such as lasers or broad-band polychromatic gas discharge sources such as He-Ne discharge lambs. Most spectroscopic applications require stable optical-power output of the light source, namely, the intensity of the light emitted does not change over the period of interest of spectroscopic measurement. The stabilization of the light source can be achieved through the regulation temperature of the active light-emitting area of the light source or

waiting a certain amount of time until the temperature of the light source gets stable.

The second unit of a spectrometer consists of optical elements which enable the control of the spatial characteristics and polarization state of the light. Moreover, the light manipulation unit may include a monochromator, which is a dispersive or diffractive optical element-containing device. A monochromator separates the light into its constituent wavelengths. A spatial filtering of the light inside a monochromator, i.e. by allowing only a small portion of the diffracted or dispersed light to pass through a thin slit, a narrow-band light source can be obtained from a broad-band light source.

The third unit of the spectrometer is the sample stage where the light and matter interaction is investigated. It contains a tool or stage that holds the sample under investigation so that the sample can interact with light. Depending on the scope of the spectroscopy application, it may contain an integrating sphere, which is a hollow spherical container whose inner walls are painted with perfectly reflecting material. The design of the sample stage can vary depending on the aspect of the light-matter interaction, such as reflection, transmission, or scattering.

The last unit of a spectrometer, the light detection unit, is the collection of the component where the light after light-matter interaction is detected and analyzed. The detection can be achieved through various components such as photodiodes, photo-multiplier tubes (PMT), or charge-coupled devices (CCD). Photodiodes are generally made of semiconductor materials that are capable of producing an electrical signal when their active surfaces are excited by light.

4.3.1 Angular resolved transmittance and reflectance measurements

A common way to examine the spectral distribution and angular dispersion of leaky modes of a metasurface is to conduct angular resolved far-field measurements, such as spectral zeroth-order reflectance or transmittance [72, 154, 155]. A photospectrometer (Perkin Elmer Lambda-1050) equipped with *Absolute Reflectance and Transmittance Accessory* (ARTA) (OMT Solutions) is used for the detection of the spectral and angular position of the leaky modes of metasurfaces. An illustration of the ARTA-on-photo spectrometer setup is shown in Fig. 4.7 (a) and (b). The ARTA tool provides control over both the angle of incidence θ (angle between the surface

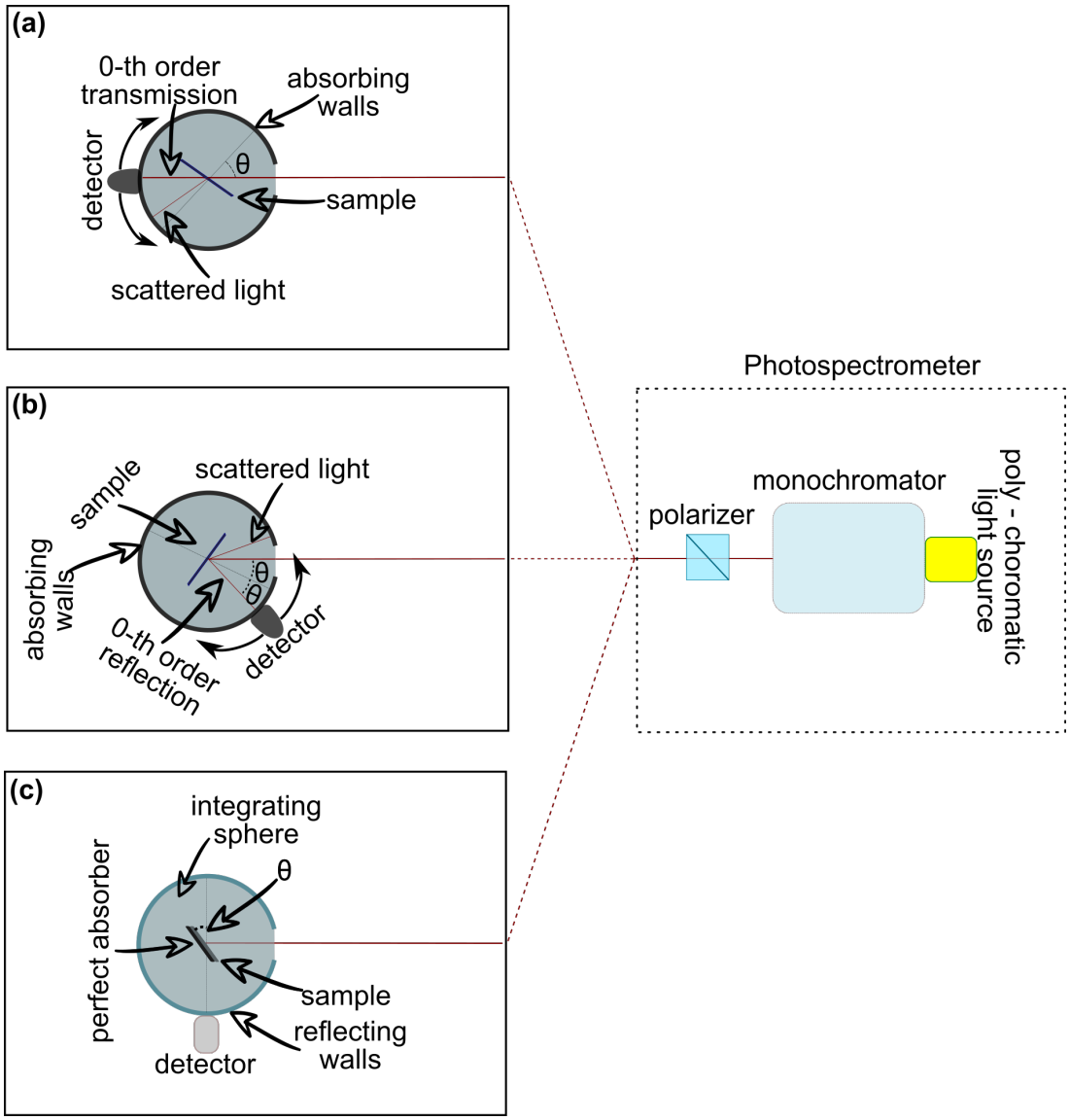

Figure 4.7: Angle resolved measurements with photo-spectometer: Angle resolved (a) directional transmittance measurement, (b) directional reflection, and (c) reflection measurement inside an integrating sphere. Solid red line represents the optical beam path while the dashed red line is for guiding the eyes to connect the different setups. Reprinted from supporting information for Ahiboz *et al*. [79].

normal of the sample and the incoming beam), and the detection of the reflected or transmitted light from a sample at different positions on a circle around the sample. Two motors change both, θ by rotating the sample around its rotation axis, and the position of the optical detector angle by orbiting the detection unit around the rotation axis of the sample stage. The inner walls of the detection unit, the light

grey circle containing the detector and sample stage in Fig. 4.7 (a) and (b), is covered with a broad-band black absorber to avoid a second interaction between reflected or transmitted light from the sample stage and the sample.

The samples are illuminated with a collimated broad-band emitting light source between 250 nm-2000 nm. Two different light sources are used for the measurements; a tungsten lamp for excitation between 320 nm-2000 nm and a deuterium arc lamp for excitation between 320 nm-250 nm. The light beam leaving the light source unit is dispersed into its colors by a Czerny-Turner style monochromator. The minimum slit size of the monochromator allows the dispersed light with spectral light 2 nm to pass through its outport. The mono-chromatized light is linearly polarized by a broad-band polarizer prism before heading toward to sample stage. Light polarization is required for accentuating any polarization dependence of the measured sample. The light reflection and transmission properties of the samples that are measured in this monograph strongly depend on light polarization. After TE or TM polarized light interacts with the sample, the reflected or transmitted light reaches the detection unit.

The detection unit is separated by an adjustable slit from the sample stage. An Indium-Gallium-Arsenide (InGaAs) photo-detector is used for the detection of the NIR light between 840 nm-2000 nm, whereas a Si photomultiplier tube (PMT) is employed for the detection between 250 nm-840 nm. The two detectors have different spectral responses and sensitivity, hence, the detectors are changed at 840 nm so that reasonable spectral detection sensitivity is ensured. Calibration and spectral matching of the reading from two detectors are auto-generated by Perkin Elmer's data acquisition software. However, a spectral mismatch can be still observed when the measured quantity, i.e. reflection or transmission intensity, is low. Nevertheless, the negligible spectral mismatch at 840 nm can easily be discerned from resonance patterns on the measured spectrum. Both angular resolved transmittance measurement (ARTM) in Fig. 4.7 (a) and angular resolved reflectance measurement (ARRM) in Fig. 4.7 (b) with the ARTA tool reveal spectral and angular dispersion of the spectral features of the measured sample. For example, the leaky modes of a metasurface can be detected by both ARTM and ARLM setups since leaky modes can be traced as resonant patterns in reflectance and transmittance spectra. The leaky modes interfere with the continuum of the radiation. The resonance patterns due to the coupling of the leaky mode and incident radiation can be detected on both the spectrum of zeroth order or higher order (diffracted and scattered light)

transmitted and reflected light. However, the zeroth order reflection and transmission is of interest since the angular position of the transmitted and reflected light can be precisely determined while the higher order transmitted and reflected light is dispersed. For example, the angular position of the diffracted light depends on the wavelength of the light. An ARTM and ARLM of the diffraction orders require continuous movement and adjustment of the detector angle which would make the measurements challenging. ARTM in Fig. 4.7 (a) is done at a fixed detector angle since the position of zeroth-order transmitted light is incident on the same position on the detector stage when the angle of incidence θ is swept. On the other hand, detector angles are changed to 2θ for ARRM Fig. 4.7 (b) since the angular difference between directional reflected light from a surface and incident light is 2θ by Snell's law. The rotation angles regarding the sample stage and detector stage are illustrated in Fig. 4.7 (b).

Alternatively, ARRM can be also performed for a sample placed inside an integrating sphere which is attached to the photo-spectrometer as shown in Fig. 4.7 (c). Contrary to the zeroth order ARRM setup in Fig. 4.7 (b), the higher-order reflections (scattering and diffraction) can be collected by ARRM with integrating sphere in Fig. 4.7 (c) since the detector at a fixed angle can receive the light reflected from to sample in all directions. A perfect absorbing foil (Edmund Optics) is placed at the back side of the sample such that the light transmitted through the metasurface is blocked.

4.3.2 Upconversion luminescence measurements

This subsection will give a detailed description of the devices and tools that are used in luminescence measurements. First, optoelectronic devices are introduced. Next, the design of the angular resolved luminescence measurement (ARLM) setup is detailed. In the end, the measurement details are presented.

Various optoelectronic devices are used for the detection, and characterization of light sources, and UC luminescence:

Spectrometer-1: The spectral measurements of the UCNPs between 200 nm and 1021 nm were performed with a compact charge-coupled device (CCD) spectrometer by Thorlabs (CCS200/M) which is a Czerny-Turner type spectrometer. The spectrometer consists of a diffraction grating and Si CCD array. The grating has a groove density of 600 per mm. The spectral accuracy is noted as less than 2 nm

at 633 nm. The CCS array has 3648 pixels with a pixel size of 8 μm x 200 μm. The spectral resolution of the CCD array is 4 pixels/nm with a signal-to-noise ratio less than 2000:1. The amplitude and spectral position of the spectrometer with its fiber optic cable were calibrated and certified by Thorlabs factory. The same fiber optic cable was used throughout all experiments to ensure accuracy and consistency in each experiment. Further check on spectral precision was tested by comparing the emission spectrum of well-known luminescent molecules (PtTPBP and BPEA) and various light sources (calibrated diode laser source with λ_{em} = 637 nm and λ_{em} = 532 nm).

Spectrometer-2: A NIR spectrometer, NIRQuest by Ocean Optics, for characterizing the spectral profile of the laser source. NIRQuest has a Czerny-Turney configuration, similar to the spectrometer-1, and it can perform spectral measurements between 850 nm and 1700 nm. Its grating has a groove density of 150 per mm. An Indium-Gallium-Arsenide CCD array with a pixel size of 25 μm x 500 μm and total pixel amount of 512. The signal-to-noise ratio of the CCD array is specified as 4000:1. The optical resolution of the spectrometer is 3 nm. The calibration of the spectrometer with its fiber optic cable was done by Ocean Optics.

Powermeter: The optical power of the laser is measured by a thermal power sensor (S405C, Thorlabs) driven by a digital optical power meter (Thorlabs, PMD100D) which can measure an incident power between 100 μW and 5 W. The measurement uncertainty of the device is specified as 3%. The resolution of the powermeter is listed as 100 μW. The power meter is calibrated and its calibration is certified by the producer.

Beam profiler: A scanning knife-edge spatial beam profiler by Thorlabs (BP209IR1) is used for the characterization of the spatial beam profile of the NIR laser. This device is able to scan the spatial distribution of the incident beam by scanning the intensity of the radiation passing through two rotation slits. The slit sizes are 5 μm, and 25 μm. The 9 mm aperture of the device allows the extraction of beam profiles having a diameter between 2,55 μm and 9 mm. The beam profiler is powered by an InGaAs photodetector which is able to detect radiation with wavelengths between 500 nm and 1700 nm.

1550 nm laser source: A 1550 nm emitting solid-state continuous wave laser diode (Thorlabs) with 1.7 W maximum optical power output is used as an excitation source for luminescence measurements. The power output and central wavelength of the laser diode are stabilized with a thermo-electrical cooling (TEC) element (Thorlabs,

LDM90M) at 18 °C. The laser diode and TEC element are driven by a laser driver (Thorlabs, ITC420). The emission profile of the laser is determined by the NIR spectrometer. Although the laser diode is labeled as 1550 nm emitting, the resulting laser emission has a central wavelength at 1551 nm with full width at half maximum (FWHM) of 5 nm as shown in Fig. 4.8 (a). These parameters are obtained by

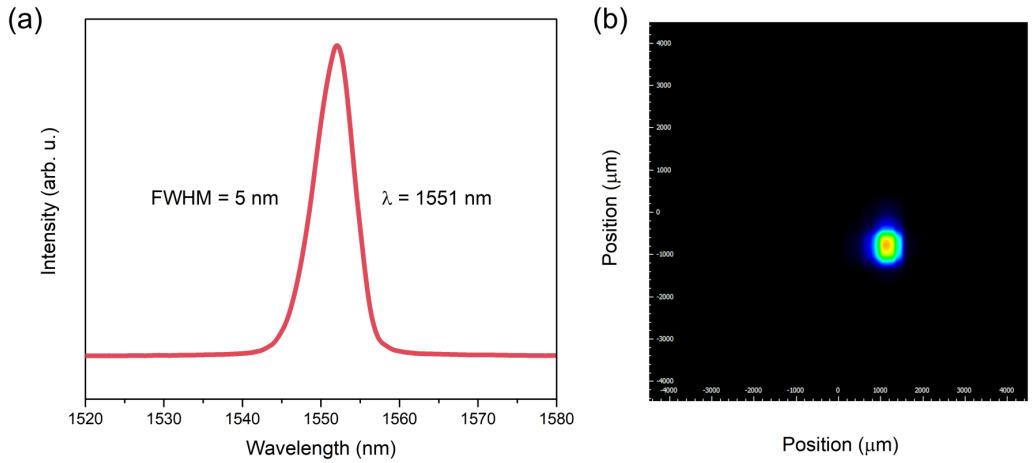

Figure 4.8: Characterization of the laser source. (a) Laser emission profile and (b) laser beam profile.

Gaussian fitting of the emission spectra. The beam emitted from the diode laser exhibits large divergence with high asymmetry along its two axes, 7° and 28°. The beam is initially observed as elliptical by the measurement done with the beam profiler. An optical setup is designed as shown in Fig. 4.9 (a) to obtain a well-defined beam profile with low ellipticity which is the basis of the luminescence measurement setup. The details of the light manipulation unit of Fig. 4.9 will be explained in the next section. The cylindrical lenses are placed in front of the laser diode for both collimation and circularizing the beam so that the excitation power density of the beam can be calculated. A circular beam profile for the laser is desired for achieving the uniform excitation of the samples. The circularization of the beam is achieved by matching the ratio of the divergence angle on two principal axes of the beam, which is 4 (28° : 7°), with the ratio between two cylindrical lenses. The focal length of the first cylindrical lens was chosen as 4.01 mm while the focal length of the second cylindrical lens is chosen as 12.7 mm. The beam profiler was placed on the sample stage where the beam meets with the sample in luminescence measure-

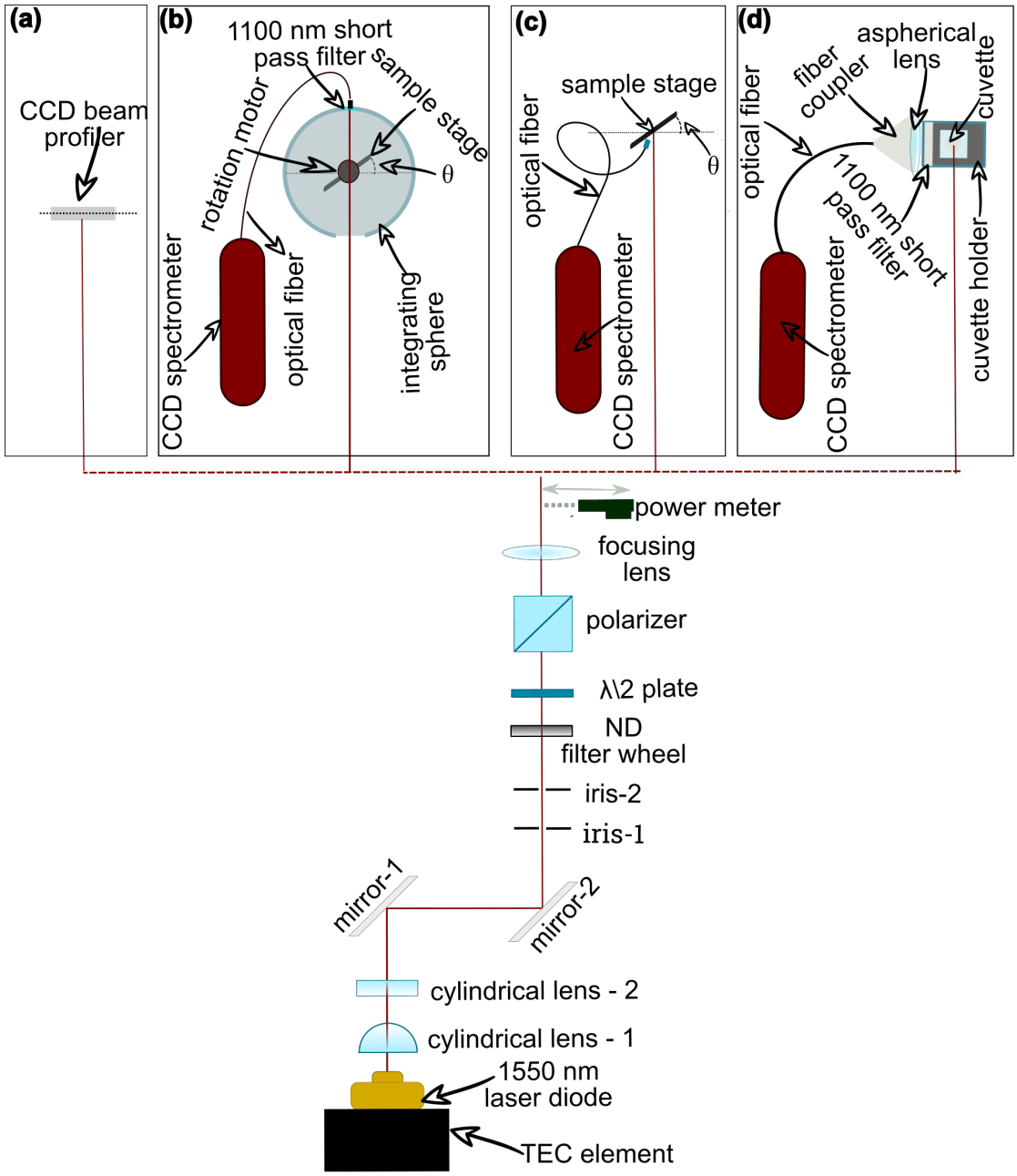

Figure 4.9: Photo luminescence setups: (a) CCD aray beam profiler for the laser beam, angular resolved luminescence measurements with (b) an integrating sphere and (c) without an integrating sphere, and (d) luminescence measurement on a cuvette. Solid red line represents the laser beam while the dashed red line is for guiding the eyes to each of the setup from (a) to (d). The solid grey rectangles encloses the each measurement setup. Reprinted from supporting information for Ahiboz *et al*. [79]

ments. The spatial beam profile of the laser light at the sample stage is shown in Fig. 4.8 (b) as a two-dimensional map of the beam profile. The area of the beam calculated as $0.006\,\mathrm{cm}^{-2}$.

Angular resolved luminescence measurements: The angular resolved luminescence measurement (ARLM) aims to explore the effect of the angle of incidence θ, the angle between the surface normal of the sample under investigation and the collimated laser beam, on photoluminescence intensity of an emitter on the sample surface. For example, an emitter on the metasurface can interact with one of the EM modes of the metasurface at a specific incident angle θ. The effect of the interaction can be traced by sweeping θ values. The ARLM setup is designed as four main parts as shown in Fig. 4.9 (b). The light source unit and light manipulation parts are kept fixed for all ARLM measurements. However, sample stage and light detection units are designed flexible so that modification on the components can be easily done considering the specific challenges of the respective measurements. The ARLM setup is based on the optical setup based in Fig. 4.9, which is illustrated in Fig. 4.9 (b). The collimated light is engaged in the light manipulation unit ARLM setup. The optical path which is the path that the laser beam is desired to travel is highlighted with the red line in Fig. 4.9 (b). The collimated laser beam is engaged in a light manipulation unit with the help of two flat mirrors. As a first step of the light manipulation unit, the stray radiation originated from the cylindrical lenses spatially filtered out the optical path by two irises. The optical power received at the sample stage is adjusted by a neutral density filter with optical density; 1-4. As discussed in Chapter 2, a metasurface can support TE- and TM-like modes which are only able to couple with TE and TM-polarized light. By considering this fact, it is necessary to use linear polarization of the light. The polarization direction of the light is altered by a rotatable half-wave ($\lambda\backslash 2$) plate, which is a birefringent crystal. A $\lambda\backslash 2$-plate has the ability to rotate the polarization vector of EMW traveling through the crystal. A Glenn-Taylor polarizer is cooperated with $\lambda\backslash 2$ plates to form a linear polarized laser beam. The aim of constructing such a stack ($\lambda\backslash 2$-plate and polarizer) is to have control over the polarization direction (TM or TE) light. When the polarization state of the laser beam is examined with two polarizers, it was realized that the ratio of the TE and TM polarized light emitted from the laser source is not equal. The emission from the laser source is in favor of TE polarization.

The linearly polarized light focused on the sample stage with a non-polarizing

focusing lens. The focusing lens has 10 cm of focal length which focuses the beam at a position that matches the position of the surface of the sample. The sample stage unit consists of an integrated sphere and a sample holder which keeps the sample middle position of the integrating sphere. The integrated sphere is a spherical cavity with a radius of 2.5 cm such that its inner walls are covered with a broadband reflector. The top of the integrating sphere contains a hole where the sample holder is engaged to the exact middle position of the integrating sphere. The sample holder is connected to a rotation ring and a servo motor which gives rotation capabilities, and consequently, the angular resolution of the ARLM setup. The laser beam is accepted into the integrating sphere via a circular hole which has a radius of 0.5 cm. The distance between the light source unit and the surface of the sample under investigation has to be the same as the distance between the light source unit and the position of the CCD array of the beam profiler in Fig. 4.9 (a). The position of the sample is calculated by considering the distance between the aperture of the beam profiler and the surface of the CCD array. After the position of the integrating sphere is set and fixed on the optical path, further consideration was done along the axis perpendicular to the optical path such that the beam always lunches on the rotation axis of the sample holder. In that way, the center of the beam always excites the same area of the sample as the sample rotated around its rotation axis. After all the alignments were deliberately done on the sample stage unit, the detection unit is designed. The spectral analysis of the luminescence was done with the spectrometer-1 which is connected to an integrated fiber optic cable. The integrating sphere has a port, which is a hole connecting the tip of fiber optic cable on its shell. The port is designed in a way that various optical filters can be placed between the inner surface of the integrating sphere and the tip of the optical fiber. An 1100 nm short-pass filter is placed between the out-port of the integrated sphere and the optical fiber coupler to protect the spectrometer from high optical power delivered by the laser.

ARLM at fixed excitation power: The ARLM was done in a dark environment inside an enclosed box to prevent stray light to enter the spectrometer. The temperature of the laser and power output is stabilized at 18°C. The laser is kept running for at least 90 min to maintain a constant excitation power output before measurements were done on the sample. The power output of the laser is measured with the power meter which is placed in front of the integrating sphere as shown in

Fig. 4.9 (a)-(d). The power meter is engaged to the optical path by flipping the mechanical arm attached to it. After the power output of the laser is stabilized, a standard procedure is applied for the spectrometer. First, the laser beam is blocked so that no photoluminescence signal is received by the spectrometer. The spectrum of the dark ambient is recorded by a spectrometer which is the combination of the detector noise and any possible stray light. The recorded background spectra are subtracted from a spectrum of a measured sample so that the noise of the luminescence spectra is reduced.

Excitation power dependent on measurements: UC is a non-linear process meaning that the UC luminescence intensity depends non-linearly on excitation power density. The comparison of the UC luminescence intensity of various P_{exc} can reveal the photodynamics of an emitter. Therefore, the other factors that can affect the UC luminescence intensity must be suppressed in a measurement while P_{exc} is systematically varied. The P_{exc} dependent ARLM was done by fixing the angle of incidence at a certain θ in Fig. 4.9 (b) while P_{exc} is varied by the ND filter. Before each measurement, the optical power meter flipped on the optical path where directly in front of the integrating sphere. Before, recording the optical power density, the optical power meter is led to stabilized for 1 min. After stable optical power density is recorded, the optical power meter is flipped off the optical path. The same spectral measurement protocol which is described for ARLM at fixed excitation power is also followed for the excitation power-dependent measurements.

Luminescence measurements without an integrating sphere: An integrating sphere inherently attenuates some of the emitted light at its ports. The integrating sphere used in the luminescence setup has three ports for fiber optic cable coupling and one large port where the light enters the sphere. All those ports can cause the emitted light from the UCNPs to leak out before coupling with fiber optic cable. On the other hand, an integrating sphere facilitates the collection of light by eliminating the considerations of directional light extraction by the nanostructures, in which the position of the detection unit (i.e. position of the tip of the CCD spectrometer-coupled fiber) determines the amount of light coupled into the fiber. The ARLM setup is modified to overcome the detection challenge at low emission intensities, which is illustrated in Fig. 4.9 (c). The luminescence measurements at the low P_{exc} are done by placing the tip of the fiber close to the surface of the sam-

ples. Although the configuration in Fig. 4.9 (c) is vulnerable to detection errors due to the light extraction effect, it does not pose a problem in the analysis of the photon upconversion dynamics since the final result of the excitation power-dependent measurements are independent of the emission intensity, in contrast, it depends on the relative intensity change among the other measured data points.

Luminescence measurements on cuvette: The luminescence measurements of the upconversion nanoparticles containing solutions were done on an experimental setup in Fig. 4.9 (d). This setup is specifically designed for luminescence measurements of the UCNPs in the cuvette. The polarization unit is removed from the optical path in Fig. 4.9. The liquid samples are filled into air-tight quartz cuvettes and placed on a cuvette holder, which is a black box with one input port (accepting laser light) and three output ports (for detection of luminescence emission from cuvette. Two of the three output ports are blocked with perfect absorbing material to avoid a second interaction between the reflected laser light and with upconversion material inside the cuvette. The output port of the cuvette holder. The emitted light is selectively transmitted with an 1100 nm short-pass filter before being focused on the tip of the fiber optical cable by an aspherical lens. The coupled light is guided to the CCD array spectrometer.

4.4 Optical Simulation

Optical transmittance and reflectance spectra of the metasurfaces are simulated, and electric field energy density on the metasurface is calculated by Dr. Phillip Manley by using the finite element solver (JCMsuite) at Zuse Institute Berlin (ZIB) [156]. The geometrical and structural parameters that are used in simulations and calculations are summarized in Fig. 4.10 (a) and (b). The metasurface model is based on the repetition of the unit cell which is enclosed by a red hexagon in Fig. 4.10 (a). The calculations are restricted by periodic boundary conditions by the red hexagon in the *x*-*y* plane, while a perfectly matched layer boundary condition is enforced in the *z*-direction in Fig. 4.10 (a). The space over the Si metasurface in *z*-direction as continuous layer with layer thickness t_{layer}. The space under the metasurface (-*z*- direction) is occupied by glass with refractive index n_{glass} = 1.53 [149]. The thickness of the glass t_{glass} is considered as infinite medium, hence,

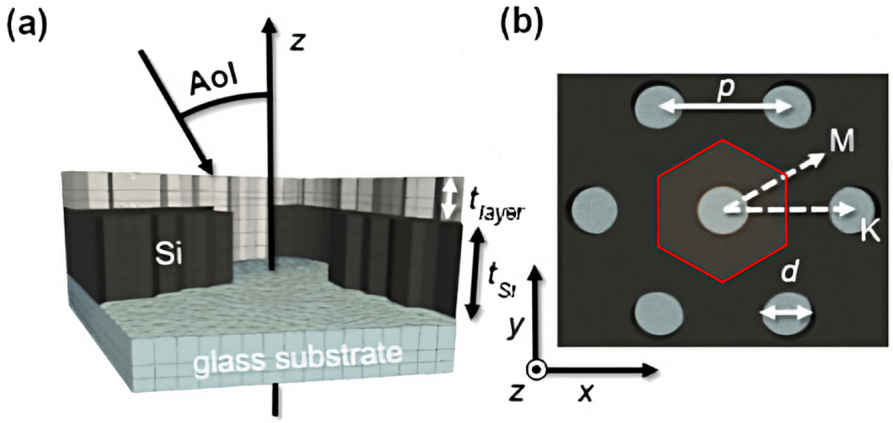

Figure 4.10: Structural and geometrical parameters of a Si metasurface. (a) Three dimensional view of Si metasurface on glass substrate at bottom and air on top. (b) two dimensional (top-view) of the Si metasurface. Adapted from Ahiboz *et al*. [80].

no coherent effect is predicted. Moreover, a negligible dispersion by the glass is assumed, therefore, the resonance pattern on transmittance or reflectance spectra originating from leaky modes of the Si metasurface is expected to be not affected. The only effect of the glass is considered to be on the overall transmittance and reflectance throughout the spectra. Furthermore, t_{layer} is assumed to be uniform all over the x-y plane. The excitation source is modeled with plane wave approximation with either TE or TM polarization. The spatial dependence of the electric field energy w_e on electrical field $\vec{E}$ is given as:

$$w_e(\vec{r},\theta,\lambda) = \vec{E}(\vec{r},\theta,\lambda)\cdot[\vec{\epsilon}(\lambda)\vec{E}(\vec{r},\theta,\lambda)]^* \tag{4.1}$$

where $\vec{r}$, θ, and $\vec{\epsilon}(\lambda)$ are position vectors, angle of incidence of the electric field vector concerning a surface normal, the wavelength of the electrical field and dielectric constant for λ. The mean electrical field energy $w_e(\theta,\lambda)$ in a volume V over a unit cell with t_{layer}, which is depicted in Fig. 4.10 (a), is calculated by the following relation:

$$w_e(\theta,\lambda) = \frac{1}{V}\int_V w_e(\vec{r},\theta,\lambda)\mathrm{d}^3r \tag{4.2}$$

Eq. 4.2 gives the mean electric field energy within V for a monochromatic plane wave continuous excitation incident on the unit the unit-cell, however, most of the laser excitation source exhibits a very narrow emission band. A more reliable calculation can be done by simulating the emission profile of the excitation source, which

is shown in Fig. 4.8 (a). A Gaussian emission profile is assumed, hence, the laser emission line shape was fitted:

$$G(\lambda) = \frac{1}{\sigma\sqrt{2\pi}} \exp\left(\frac{(\lambda-\mu)^2}{2\sigma^2}\right) \tag{4.3}$$

where $G(\lambda)$ is the Gaussian line shape function. The σ is variance, which is related to FWHM of the laser emission (= 5 nm) $FWHM = 2\sqrt{2\ln(2)}$. The center emission wavelength is denoted as μ, which is equal to 1551 nm. The electric field energy with the addition of the Gaussian beam profile is calculated by the following equation:

$$w_e(\theta) = \int_{\lambda_{min}}^{\lambda_{max}} G(\lambda) w_e(\theta, \lambda) \mathrm{d}\lambda \tag{4.4}$$

where λ_{max} and λ_{min} are the upper and lower limit of the laser emission line width.

5 Mono- and Double-layer Silicon Metasurfaces

5.1 Mono-layer Si Metasurfaces

The coupling of leaky modes with external radiation enables many applications ranging from bio-sensing to solar cells at low excitation intensity. Since the leaky modes couple with the external radiation at certain θ and under excitation with a specific λ_{exc}, a precise adjustment of the spectral position of a leaky mode is crucial. Leaky modes of a metasurface can be tuned by changing a range of parameters. For instance, the refractive index of the slab and substrate, the in-plane geometrical parameters of the slab (lattice constant and hole diameter), and the slab thickness [71]. Although there exist many materials such as noble metals, metal oxides, and nitrite compounds, the limited number of available feasible materials for the production process impedes adjustability via the refractive index. The adjustment of hole diameter or periodicity of the metasurface often requires costly nanofabrication steps. In contrast, the slab thickness can easily be varied if a bottom-up thin-film fabrication procedure is chosen, e.g. by changing the deposition time [74].

The SEM images of the produced metasurfaces are shown in Fig. 5.1 (a)-(d). A large area SEM top-view image shows the air holes in Si arranged periodically over the surface in Fig. 5.1 (a). A close-up top-view SEM image of a produced Si metasurface is separately shown in Fig. 5.1 (b), which reveals perfectly shaped air holes on the Si metasurface. Layers of the Si metasurface - glass substrate are depicted in SEM cross-section image in Fig. 5.1 (c). The shiny bottom layer of the SEM cross-section image is the glass substrate. The darker silicon-oxide layer is formed after the NIL liquid is cured, which has approximately the same refractive

index as the glass substrate. The brighter layer on top of the silicon oxide layer is the Si metasurface with air hole in it. Finally, a 30° tilted angle SEM image in Fig. 5.1 (d) shows both cross-sections of the Si metasurface and air holes in the Si metasurface.

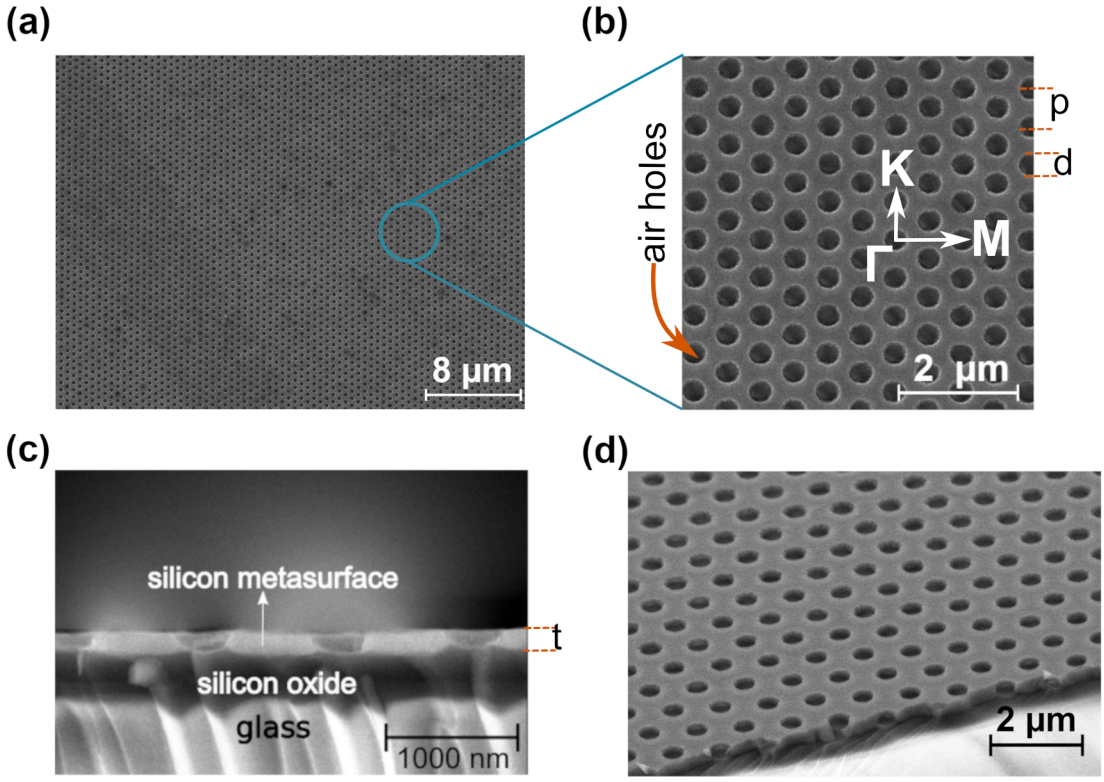

Figure 5.1: SEM images of the produced metasurfaces: (a) Top-view SEM image a produced Si metasurface, (b) the magnified top view of the SEM image. The Γ, M and K indicates high symmetry direction of hexagonal lattice, whereas p and d represents periodicity and diameter of the air holes. (c) A cross-section view of a Si metasurface on glass substrate. The thickness of Si is represented by t. (d) A 30° tilted view of the Si metasurface on glass substrate.

In this study, production, optical characterization, and AFM analysis of the Si metasurfaces were performed by Doguscan Ahiboz. SEM images were taken by Carola Klimm. All the simulations and numerical calculations are performed by Dr. Phillip Manley (JCMwave GmbH). ARDT measurements of the double-Si metasurface were conducted by Michele Segantini.

5.1.1 Analysing the leaky modes of Si metasurfaces

The structural and geometrical parameters of the produced Si metasurfaces are summarized in Fig. 5.1 (b), and (c). The Si layer thickness of the metasurface is denoted as t in Fig. 5.1 (b). The distance between two nearest-neighboring air holes of the Si metasurface is refered to period (p), as indicated in Fig. 5.1 (b). Si metasurfaces with two different p are fabricated in this study: p = 600 nm, and p = 1000 nm. The diameter of the air holes (d) in Fig. 5.1 (b) are measured as d = 325 nm and d = 400 nm for Si metasurface with p = 600 nm and p = 1000 nm, respectively.

A comprehensive exploration of the spectral and angular dispersion of the leaky modes of a metasurface is needed to carry out to derive benefit from strong near-fields provided at a metasurface. Angle-resolved far-field measurements, such as directional transmission or reflection measurements, are widely employed for the examination of the leaky modes of a metasurface [70, 77]. Radiation incidents on a metasurface can be scattered into multiple diffraction orders. Moreover, the external radiation with a specific λ_{exc} and polarization can couple with the leaky modes of a metasurface at particular θ, which is the angle between wave vector of excitation light and the surface normal (z-axis in Fig. 4.10) of the Si metasurface. The effect of the coupling between external radiation and the leaky modes of a metasurface is spotted as resonance patterns in the zeroth order transmission or reflection measurements. Detection of the spectral and angular position of the leaky modes of the Si metasurface with p = 600 nm and p = 1000 nm were done by the ARTM measurement which is described in Fig. 4.7. Although ARTM and ARRM give equivalent spectral information, the ARTM is more suitable for extracting the spectral data at an oblique angle and normal incidences. The ARTM results of the Si metasurfaces are featured in Fig. 5.2 (a) for p = 600 nm and Fig. 5.2 (b) p = 1000 nm. The measurements were performed by rotating the Si metasurfaces in steps of 2° (from θ = 0° to 60°) through the two distinct high-symmetry directions, $\Gamma \rightarrow$ M (the left column of Fig. 5.2) and $\Gamma \rightarrow$ K (the right column of Fig. 5.2), with TE (the upper-row of Fig. 5.2 (a) and (b)) and TM (Fig. 5.2 (the lower-row of Fig. 5.2 (a) and (b))) polarized light. The resonance patterns, visible as sharp dark blue lines in Fig. 5.2, imply the presence of the leaky modes as a result of coupling external radiation which lies on the NIR and visible spectrum. The solution of the Maxwell equation with periodic boundary conditions in Eqn. 2.12 dictates that the equations are scale-invariant, thereby, the spectral position of the leaky modes is expected

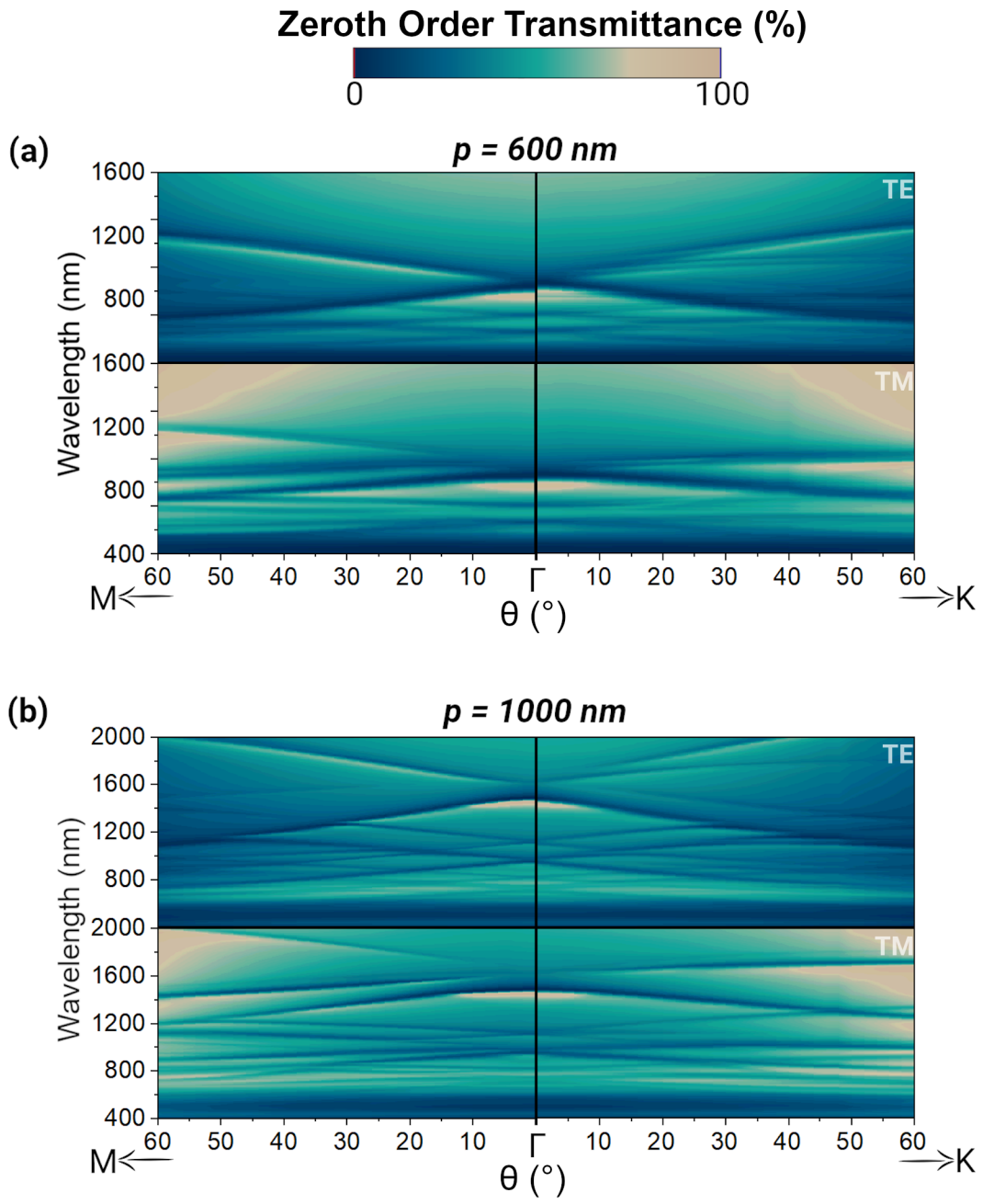

Figure 5.2: Angular resolved transmittance (zeroth order) measurement of a Si metasurface on glass with Si layer thickness t = 100 nm, periodicity: (a) p = 600 nm and (b) p = 1000 nm , measured with TE (upper row) and TM (lower row) polarized light and rotation along the Γ → M and Γ → K direction. Taken from Ahiboz *et al*. [80].

to be red-shifted by increasing t [69]. A noticeable difference in spectral position of the leaky modes of the Si metasurface with p = 600 nm and p = 1000 nm was observed, indeed. The spectral position of the leaky modes shifts towards longer wavelengths with increasing p, hence, the p can be considered as a coarse spectral tuning parameter for the spectral position of leaky modes. Although polarization of the excitation source has no direct effect on the spectral position of the leaky modes, they determine how and which leaky modes of the metasurface in a specific symmetry direction can couple with the excitation source. It is worth mentioning that the resonance pattern of the produced Si metasurface with t = 100 nm show a peculiar behavior around normal incidence, the modes in the NIR tend to vanish while the leaky modes in the shorter NIR and visible wavelengths are continuous across the normal incidence. The vanishing nature of the leaky modes is observed to be valid for both polarization (TE and TM) and the high symmetry directions $\Gamma \rightarrow$ M and $\Gamma \rightarrow$ K, which is attributed to hexagonal crystal-symmetry protected BICs, which are the localized discrete modes within the continuum of radiation [107]. Moreover, the leaky modes have various spectral widths as seen in Fig. 5.2 which indicates the spectral width of the resonances is affected by the thickness of the Si metasurface. In general, sharper resonances correspond to strong near fields when they are excited by a light source with a narrow emission bandwidth. In contrast, broader resonances correspond with less intense near fields but they are more effective in coupling to light with broader spectral width. After having identified with a vast variety of leaky modes, a leaky mode in NIR-Vis wavelengths can be chosen and engineered by setting p different values during the production process. The engineering of the leaky modes can be done by adjusting various structural parameters of the metasurface. For example, the spectral position of the leaky modes can be effectively tuned by systematically varying the diameter of the air holes d. However, these parameters require the production of the metasurface with e-beam lithography and EUV NIL methods for each parameter which are not beneficial for large areas and mass production. As a second production parameter t is investigated as a feasible and easily accessible spectral tuning parameter of the leaky modes since t can be systematically changed in Si deposition independent of s-NIL processes.

5.1.2 Engineering the spectral position of the leaky modes of the Si metasurfaces with p = 600 nm and p = 1000 nm.

The thickness of the Si layer t determines to extend of the dielectric contrast between the Si-glass substrate and as well as between Si-air, geometrically depicted in Fig. 5.1, consequently how the electromagnetic energy in the event of resonance is dissipated through the space. Moreover, t dictates the dielectric contrast experienced by the perpendicular component (with respect to surface normal) of the light incident on the air-Si interface. Si metasurfaces with five different Si thicknesses t = 60 nm, = 80 nm, = 90 nm, = 100 nm and = 150 nm were produced with p = 600 nm and p = 1000 nm simultaneously. The identification of the leaky modes of the Si metasurfaces with different thicknesses was done with ARTM. The spectral position of the leaky modes with 5 different t with TE polarized light under rotation through $\Gamma \rightarrow$ M high symmetry direction are shown in Fig. 5.3 (a) and (b) for Si metasurface with t = 600 nm and t = 1000 nm, respectively. Three important wavelengths, 808 nm - 980 nm - 1550 nm, which are widely studied for UC experiments concerning solar cells, bio-assays, and telecommunication applications, are indicated in Fig. 5.3 as white dashed horizontal lines. A systematic shift of the spectral position of the leaky modes through longer wavelengths is achieved with increasing t. It can easily be seen that the three important excitation wavelengths can be coupled with a few different leaky modes at various θ, which facilitates the accessibility of strong near fields. In addition, the difference between zeroth order transmittance maximum and minimum across the resonances are greatly increased. On the other hand, some of the resonant features for wavelengths shorter than 500 nm are not clearly visible with increasing t, since the Si absorption cross-section is larger in this regime, hence absorption depth increases greatly for thicker Si layer. Especially, the ability to distinguish the leaky modes for metasurfaces with t = 150 nm in Fig. 5.3 (a) and (b) is reduced down to 800 nm regime which limits applicability the Si metasurface for its possible application in the uv-vis regime, thus, Si metasurfaces with thicker layer thickness will not be considered in this study further.

The effectiveness of the incident radiation and leaky modes coupling on a Si metasurface depends on the dielectric contrast along the metasurface. If d and t are significantly smaller than λ_{exc}, the effect of the parameters on the metasurface is experienced as a small perturbation on the dielectric function, hence, the periodic nanostructures on the metasurface can only be probed by shorter wavelengths. If d

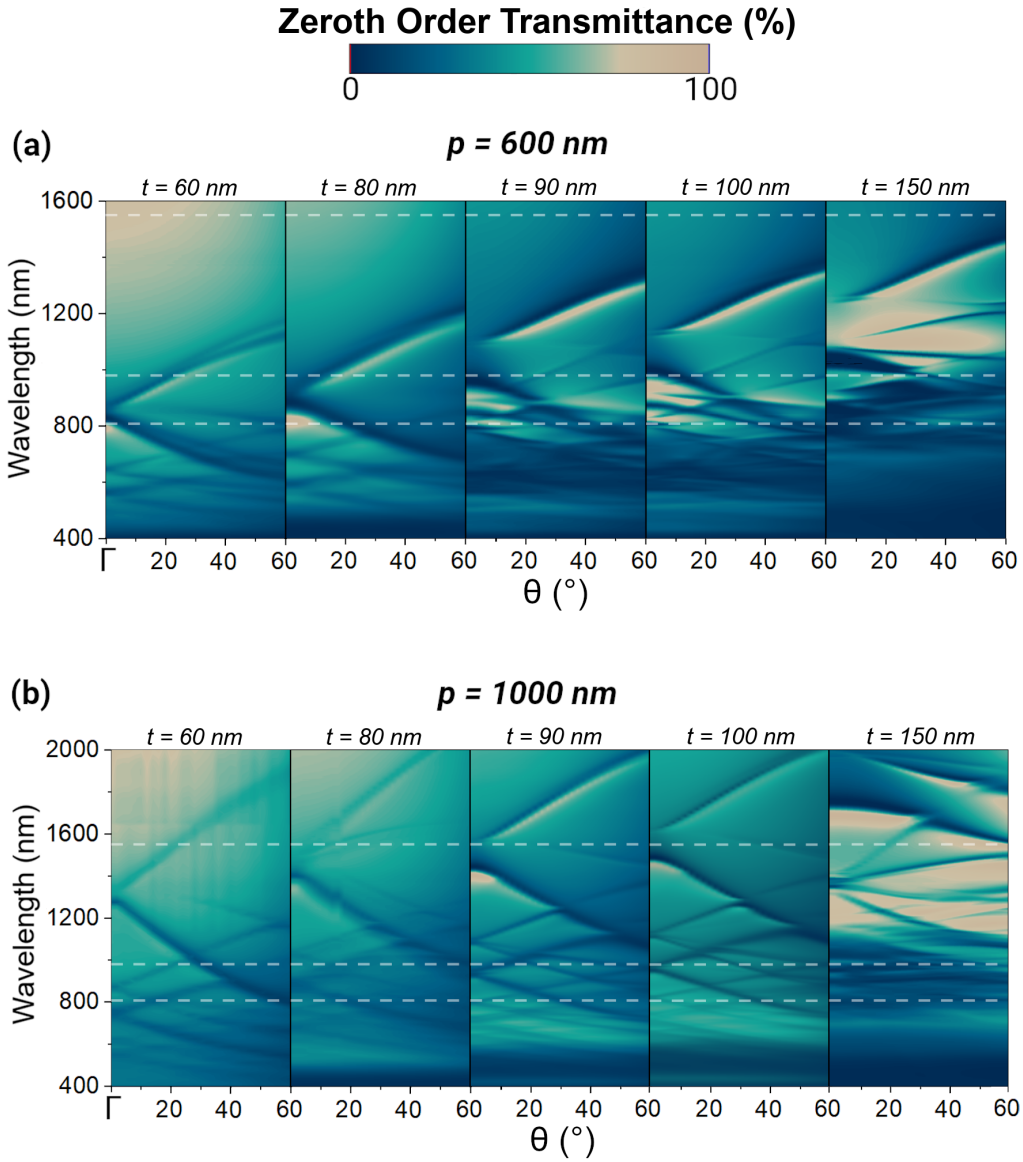

Figure 5.3: Angular resolved transmittance (zeroth order) measurements with TE polarized light under rotation through the Γ → M direction on Si metasurface with (a) p = 600 nm and (b) p = 600 nm. The thickness t varies from 60 nm to 150 nm (left to right). Taken from Ahiboz *et al*. [80].

gets larger, the amount of dielectric material on the metasurface decreases, hence, the effective dielectric constant of the metasurface decreases [69]. A critical value of t and d need to be optimized. A consequence of decreasing t can be seen as decreasing detectability of the leaky modes on the Si metasurfaces with thinner t, i.e the sub-600 nm leaky modes of the t = 60 nm Fig. 5.3 (a) and (b) t = 60 nm.

A similar behavior is observed when the t is greater than the certain value (after 100 nm), the quantification of the leaky modes in the visible part of the spectrum in Fig. 5.3 becomes challenging. Considering that Si has a high extinction coefficient for blue to green wavelengths, absorption by the Si metasurface becomes noticeable. Therefore, detection of the leaky modes by ARTM measurements is unreliable in this wavelength region. Concerning practical applications, such as the detection of signal with a visible wavelength on metasurface, the choice of t is restricted by the need of the application. As the previous discussion of the transmittance spectra in Fig. 5.3, a few of the produced metasurfaces stand promising candidates for near-field enhancement for practical application with at the three important excitation wavelengths mentioned before. Especially, Si metasurface with p = 1000 nm and t = 100 nm in Fig. 5.3 (b) shows three prominent resonances at near oblique incidence angles for the three wavelengths (808 nm, 978 nm and 1550 nm). Hence, the further analysis of the leaky modes is focused on the Si metasurface with p = 1000 nm and t = 100 nm.

5.1.3 Near-field effects on Si metasurfaces

Local energy density enhancement on the Si metasurface is expected when external radiation couples with one of the leaky modes of the Si metasurface. If luminescent particles are placed on the Si metasurface and excited by a light source, such that λ_{exc} is resonant at θ with one of the leaky modes of the Si metasurface, a brighter luminescence with respect to the non-resonant case is expected. To get a better insight into leaky modes and how effectively they can enhance near fields, ARTM spectra are calculated by FEM simulations for the Si metasurface with p = 1000 nm and t = 100 nm. A comparison between the ARTM experiment and ARTM simulation is drawn in Fig. 5.4 (a) and (b). All the other geometric parameters noted in Fig. 4.10 and excitation source profile are kept the same for the simulation with experimental parameters of metasurface as shown in Fig. 5.1. The rotation through $\Gamma \rightarrow$ M direction with TE polarized excitation with collimated planar wave approximation was calculated with FEM. As a result, an excellent agreement between ARTM-experiment (5.4 (a)) and ARTM-simulation (5.4 (b)) proves that the leaky modes are responsible for the resonant pattern in ARTM spectra. However, a slight disagreement on spectral dispersion of the leaky modes between experimental and simulated ARTM appears, which originate from the presence of the SiO_x

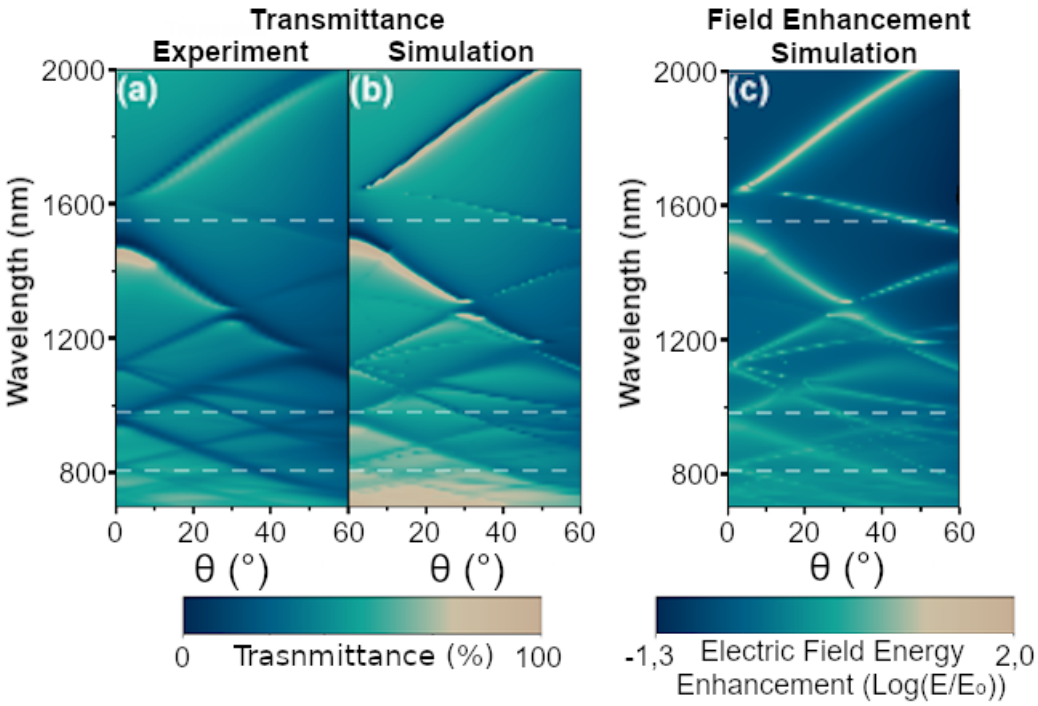

Figure 5.4: Comparison of experimental and simulation results of the Si metasurface with p = 1000 nm and t= 100 nm: (a) ARDT measurement, (b) the simulated ARDT, and (c) the simulated electric field energy enhancement in a 100 nm layer above the metasurface with rotation along the Γ → M direction under TE polarization. Taken from Ahiboz *et al*. [80].

residuals inside air holes as an artifact of mechanical abrasion during the Si metasurface production.

The electric field energy enhancement, which is the ratio of the total electric field energy density to incident electric field energy density, is calculated within 100 nm volume over the unit-cell of Si metasurface. The calculations are presented in 5.4 (c) on a logarithmic scale. The electric field energy enhancement achieved at incident angles θ , where the enhancement factor ($\log(\boldsymbol{E}/\boldsymbol{E}_0)$) is greater than zero, reasonably matches with the spectral position of the leaky modes. Therefore, the simulations of leaky modes can be employed for predicting the spectral and angular position of a specific λ_{exc} for achieving near-field enhancement. Large enhancement factors up to 100-fold of the electrical field energy have been predicted by FEM simulation, especially for $\lambda_{exc} > 1200$ nm. The FEM calculation also takes absorption of the Si into account, consequently, the electric field energy enhancement sub-λ_{exc} is substantially smaller due to a great portion of the $\boldsymbol{E}$ is absorbed by Si. Nonethe-

less, the simulation results show that the absorption losses for Si metasurface t = 100 nm is a small quantity.

As noted before, much practical application employs excitation source with λ_{exc} 1550 nm, 978 nm and 808 nm at normal incidence or slightly oblique θ. Therefore, electric field energy enhancement is calculated as a function of t at normal θ and slightly oblique θ. The calculated results are shown in Fig. 5.5 (a) and (b) for Si metasurface with p = 1000 nm and p = 600 nm, respectively.

The three important λ_{exc} = 1550 nm, = 978 nm, and = 808 nm are represented as 'blue', 'red' and 'black' curves in Fig. 5.5 (a) and (b), respectively. Moreover, the two different θ cases, θ = 0° and 4°, were illustrated as solid and dashed curves. Fig. 5.5 (a) and (b) shows that for designing an optimal t for Si metasurface enhanced application, λ_{exc} must be considered since the optimized t for maximum electrical field energy density enhancement is different for each one of the three λ_{exc}. The dependence of the electric field energy density enhancement on t can be attributed to two distinct phenomena. First, the t to achieve the highest electric field enhancement alters slightly, when θ increases from 0° to 4°. For example, the electric field energy enhancement for λ_{exc} at normal incidence is 15-fold for on the Si metasurface with t = 106 nm, whereas, the same enhancement value can be achieved for t = 109 nm for θ = 4°. The maximum electrical field enhancement in this regime is calculated to 17-fold for λ_{exc} = 1550 nm for the Si metasurface with p = 1000 nm (Fig. 5.5 (a)) while calculation reveals maximum electrical field energy enhancements for the λ_{exc} = 980 nm with t = 173 nm and λ_{exc} = 808 nm with t = 129 nm are 10-fold and 6-fold (Fig. 5.5 (b), respectively. Although electrical field energy by those leaky modes is limited, the enhancement values are less sensitive to thickness variation up to a certain extent, thereby, coupling between the leaky mode and excitation source is less dependent on local thickness variation due to structural imperfections introduced by the NIL process. The second type of thickness - electrical near field energy enhancement strongly depends on θ, when θ is increased from enhancement factor vastly increases for a specific narrow range of thickness values. At normal incidence (θ = 0°), the Si metasurface with p = 1000 nm enhances λ_{exc}1550 nm excitation more than 10 times when the t = 95 nm and t = 220 nm. On the other hand, the maximum enhancement values for λ_{exc} = 978 nm and 808 nm are fairly limited, maximum electrical field energy enhancement can be improved just a few fold in 5.5 (a). However, when the Si metasurface tilted to θ = 4° through $\Gamma \rightarrow$ M direction, the electrical field energy enhancement dramatically

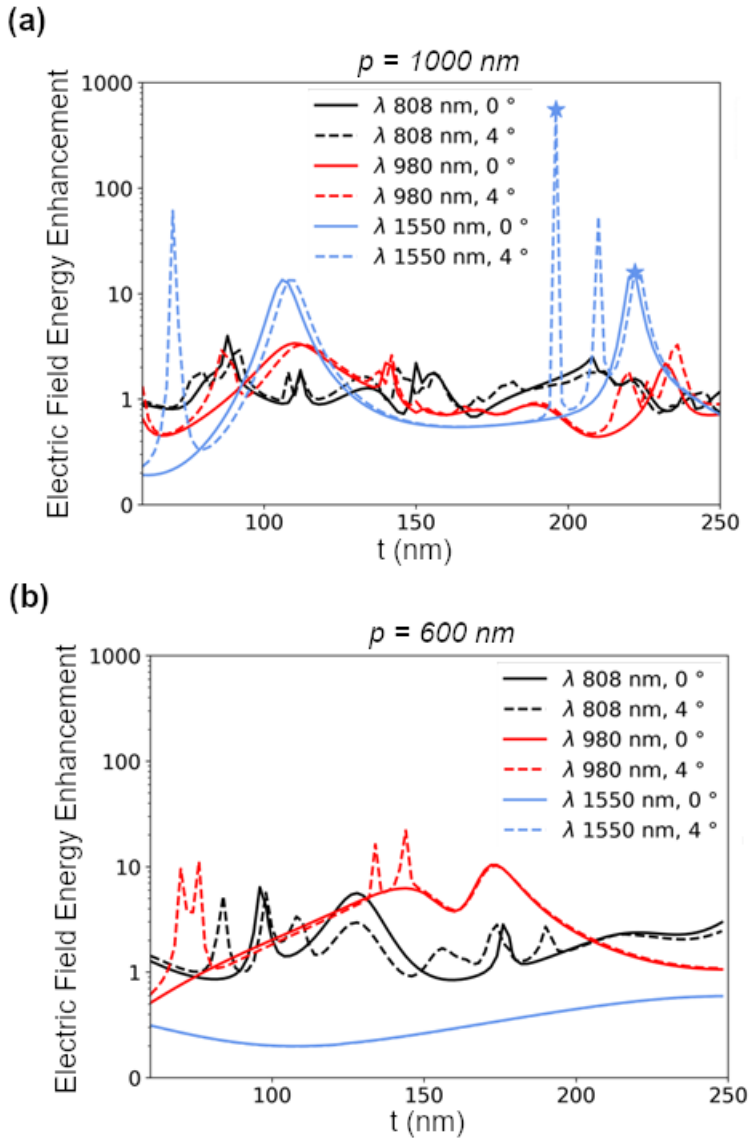

Figure 5.5: Electric field enery enhancement over Si metasurface with lattice period of (a) 1000 nm and (b) 600 nm as function of Si thickness. The solid curves represents TE polarized excitation at $\theta = 0°$ while the dashed curves represents TE polarized excitation at $\theta = 4°$ in the direction of $\Gamma \rightarrow$ M. Taken from Ahiboz *et al.* [80]

increases for $\lambda_{exc} = 1550$ nm (blue-dashed curve in 5.5). The electric field energy enhancement expended exceptionally up to 500-fold for the t = 195 nm , at $\theta = 4°$, while at $\theta = 0°$, by contrast, the electric field energy density is reduced. A similar increase with at $\theta = 4°$ appears when $t = 60$ nm and $t = 220$ nm for $\lambda_{exc} = 1550$ nm, and at various t for $\lambda_{exc} = 978$ nm and $\lambda_{exc} = 808$ nm as well in Fig. 5.5 (a). The sharp

increase in the electric field energy enhancement is also seen for the Si metasurface with p = 600 nm in Fig. 5.5 (b) for the λ_{exc} = 978 nm and 808 nm. However, no significant enhancement factor was calculated for λ_{exc} = 1550 nm which is consistent with the ARTM result presented in 5.3 (a), since no leaky modes were detected at 1550 nm.

The absence of enhancement effects on Si metasurface at normal incidence for specified t in which high enhancement factor calculated is originated from symmetry protected BICs [107, 157, 158]. The geometry of the hexagonal lattice of the Si metasurface is a member of the D-6 symmetry group, which forms symmetry-protected BIC at normal incidence. When the symmetry is broken by tilting the Si metasurface for 4°, the leaky mode is able to couple with external radiation and give a rise to electric field energy density over the Si metasurface [107]. Although these modes are fundamentally inaccessible, the local imperfection introduced by the NIL process transforms them into partially accessible modes. This effect can be easily substantiated by near-oblique incidence behavior of the leaky mode of Si metasurface with t = 90 nm, which lays between 1550 nm, and 978 nm dashed lines in Fig. 5.3 (b). There is no efficiently detectable coupling at normal incidence. As the t reduced down to 60 nm, resonant pattern at normal incidence can be seen as a result of the partial coupling of the leaky modes. However, as the t increases, the structural imperfections become insignificant and can be considered small perturbations on structural parameters of the Si metasurface, hence, coupling at normal incidence and near-oblique incidence becomes symmetry protected and resonance pattern at normal incidence vanishes. Furthermore, the BIC have potential to enhance electric field energy vastly. The BIC above the 1550 nm line investigated deeply by FEM calculations, the spectral position of the BIC shifts to 1630 nm when the t increased to 195 nm. In this case, when the symmetry is broken by the rotation to 4°, the electrical field energy enhancement up to 3000-fold can be achieved.

The two different thickness dependencies of the electric field energy enhancement are needed to be investigated elaborately to explore the full potential of the leaky modes, which leads to the two different behavior, for future luminescence enhancement on Si metasurface studies. Two different t of the Si Metasurface with p = 1000 nm, at t = 221 nm and t = 196 nm, leading to a high electric enhancement factor is indicated by a blue star, whose three-dimensional electric field energy enhancement values are depicted in Fig. 5.6 (a) and (b) for the metasurface's unit-cell, respectively. The normal incidence excitation with λ_{exc} = 1550 nm of the Si metasur-

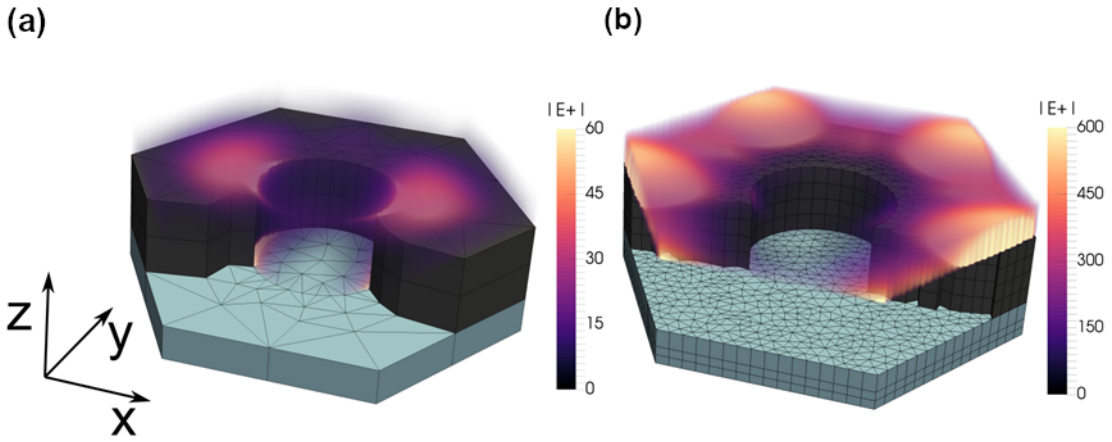

Figure 5.6: Three dimensional electric field energy density $|E_+|$ distribution of the Si metasurface with period of 1000 nm for (a) Si thickness of 221 nm under 1550 nm TE polarized excitation at $\theta = 0°$, and (b) Si thickness of 196 nm under 1550 nm TE polarized excitation at $\theta = 4°$. Different scale bars are used for part (a) and part (b). Taken from Ahiboz *et al.* [80].

face with $p = 1000$ nm and $t = 221$ nm in Fig. 5.6 (a) distributes electric field energy to two lobes located on x-axis. A small amount of electric field energy is calculated to be concentrated also on the bottom of the air holes of the Si metasurface. On the other hand, $\lambda_{exc} = 1550$ nm excitation of the Si metasurface with $p = 1000$ nm and $t = 196$ nm at $\theta = 4°$ leads to an intense electric field energy concentrated on six-lobes on the metasurface as shown in Fig. 5.6. The electric field energy distribution in Fig. 5.6 (b) contrasted with the one in Fig. 5.6 (a) in two ways: i) the electric field energy coverage is more uniform through the surface on which interaction of an emitter can be attained more easily, and ii) electric field energy is more intense, a factor of 10 exists when scale bars of the two graphs are compared.

5.2 Double-layer Silicon Metasurface

A schematic representation and a 30° tilted angle SEM photograph of the produced double-layer metasurface are shown in Fig. 5.7 (a) and (b). As it can be inferred by its name, the metasurface consists of two layers of periodic dielectric material; Si nano-disk layer with $t = 85$ nm and $d = 410$ nm supported by SiO_x nanopillars with the height of $h = 400$ nm from the glass substrate, and a Si slab with periodic hole. The structural parameters of the double-layer Si metasurface were

calculated by comparing SEM and AFM images as t = 85 nm. Both layers share the same lattice period p = 1000 nm. ARDT measurement of the double-layer Si is

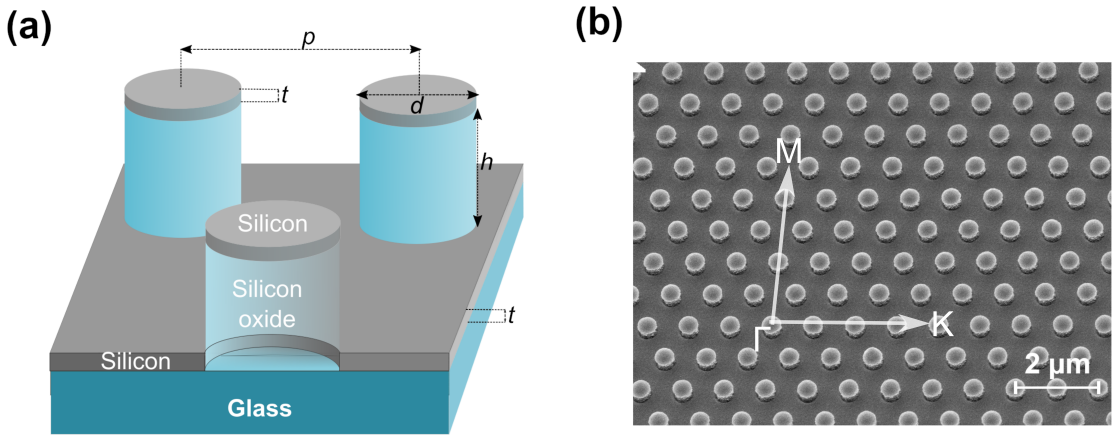

Figure 5.7: (a) A three-dimensional sketch, and (b) 30°-tilted angle SEM images of the double-layer Si metasurface.

shown in the left panel of Fig. 5.8 (a). The measurement results reveal the dispersion relation of the modes under rotation through $\Gamma \rightarrow$ M direction with TE excitation. The transmittance spectrum of the double-layer Si is simulated by using the same structural and geometrical parameters in experimental measurements. The simulated ARDT spectra are shown in the right panel of Fig. 5.8 (a). A satisfying agreement between experimental and simulated ARDT spectra is observed. However, the existence of four very narrow resonance pattern exists in simulated spectra, evidently, those resonances do not appear in ARDT measurements. These resonance patterns on the simulated ARDT are indicated with four blue stars, one for each resonance pattern. These sharp resonances, consequently modes with narrow spectral width are attributed to Rayleigh-Wood anomaly [110], are originated by the critical diffraction condition imposed by the Eqn. 2.16. When the external radiation incident on the metasurface at the critical angle of incidence, the radiating diffraction mode becomes an evanescent mode, which propagates along the metasurface [159]. These modes will be called *Rayleigh-Wood type resonances*. The reason for the disappearance of the Rayleigh-Wood type resonances in ARDT measurement is attributed to the fact that a narrow resonance is hard to couple with an excitation source with broader bandwidth than the width of the resonance. The spectral width of the light source in the ARDT measurement is 2 nm, which is significantly larger than the FWHM of the simulated Rayleigh-Wood type resonance. Furthermore, the

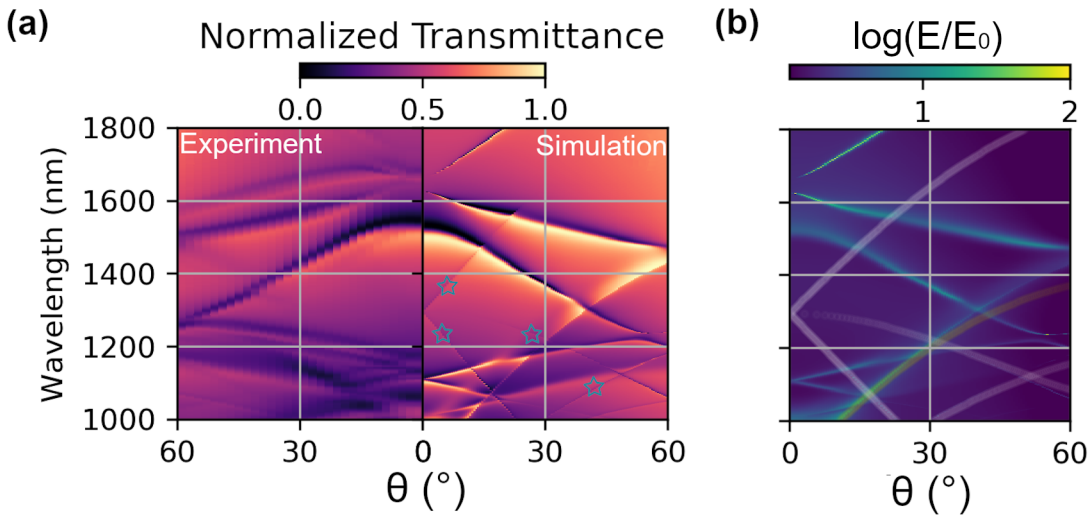

Figure 5.8: Comparison of experimental and simulation results of the double-layer Si metasurface with p = 1000 nm and t = 85 nm: (a) ARDT measurement, (b) the simulated ARDT, and (c) the simulated electric field energy enhancement on logarithmic scale in 100 nm layer above the metasurface with rotation along $\Gamma \rightarrow$ M direction under TE polarization. Taken from Manley *et al*. [81].

electric field energy enhancement factors are calculated by Eqn. 4.4 and normalized by the amplitude of the incident electric field. The E-field energy enhancement spectra are depicted in Fig. 5.8 (c). By comparing the ARDT simulation and E-field energy enhancement calculation results, strong near fields are expected where the modes exist in transmittance spectra of Fig. 5.8 (a). Vast E-field energy enhancement values with very narrow spectral widths are observed for Rayleigh-Wood-type resonances.

The leaky modes of the Si metasurfaces and BICs have already been discussed in previous sections but a deeper inspection of the source of the Rayleigh-Wood type resonances is needed. Therefore, mode contribution from each periodic dielectric layer of the metasurface in Fig. 5.7 (a) are probed separately in terms of E-field energy enhancement. The E-field energy enhancement of the double-layer Si metasurface in 5.9 (a) is compared with the Si nano-disk metasurface supported by SiO_x nano-pillars in 5.9 (b) and single-layer Si metasurface with SiO_x nano-pillars. When the Si slab is removed from the geometry of the double-layer Si metasurface, only Rayleigh-Wood type resonances are left, as shown in Fig. 5.9 (b). On the other hand, when Si nanodisks are removed from the top of the SiO_x nano-pillars on double-layer Si metasurface, similar resonance patterns with Fig. 5.9 (a) are cal-

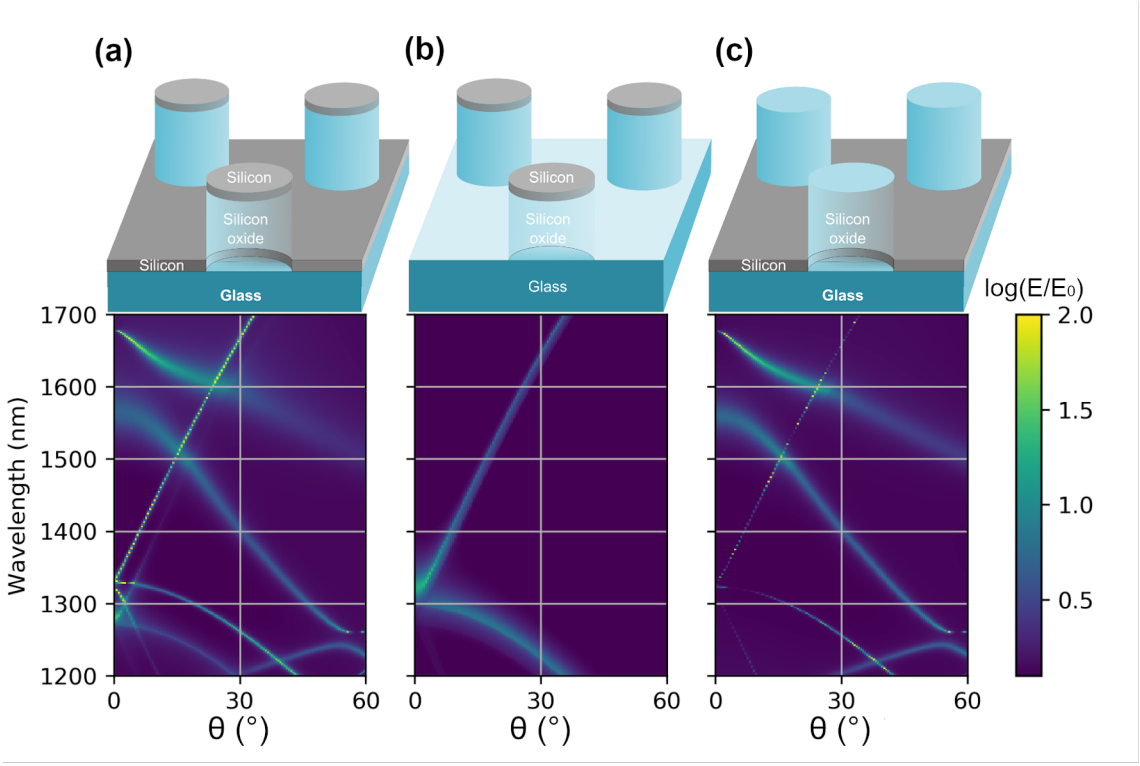

Figure 5.9: Electric field energy enhancement in logarithmic scale of Si metasurface with three different structure: (a) double-layer metasurface, (b) Si nano-disks metasurface supported by SiO_x nano-pillars, and (c) single-layer Si metasurface with SiO_x nano-pillars. Schematics of the each structure are show on top of their respective spectra. Taken from Manley *et al*. [81].

culated for Fig. 5.9 (c). Moreover, resonances at a smaller angle of incidence get narrower in Fig. 5.9 (a) with respect to Fig. 5.9 (a). A conclusion can be drawn at this point; the double metasurface broadens the Rayleigh-Wood type resonances. Therefore, a double-layer metasurface can be used for adjusting the spectral width of the Rayleigh-Wood type resonances compared to its single-layer counterpart, which may increase its coupling probability with external radiation with a broad spectral width.

6 The Photon Upconversion of β-$NaYF_4$: Er^{3+} Nanoparticles

6.1 Luminescent Properties of the β-$NaYF_4$:Er^{3+} UC-NPs

The UC emission of β-$NaYF_4$:Er^{3+} in c-Hexane solution is achieved under 1551 nm laser excitation. A photographic image shows intense UC emission of β-$NaYF_4$:Er^{3+} in 1 mm thick cuvette in Fig. 6.1 (a). In this image, 1551 nm laser excitation is incident from the left side on the cuvette, which is indicated with a white arrow. The bright orange light emission in the middle of the frame is the UC emission from UCNPs, which is a combination of a few emission bands in the visible spectrum. The UC emission spectra is recorded under laser excitation with P_{exc} = 32 W/cm^2 and with λ_{exc} = 1551 nm with optical setup described in Fig. 4.9 (d). The recorded emission spectra are shown in Fig. 6.1 (b). Four bright emission bands appear at the visible and NIR spectrum. These emission bands correspond to the radiative transition between energy levels of Er^{3+}.

An energy level diagram is plotted in Fig. 6.1 (c) based on UC emission peak by comparing experimental and calculated energy levels in literature to show the possible radiative decays between the energy levels [160–163]. The diagram displays the process of radiative relaxation from meta-stable states to the ground state $^4I_{15/2}$ of Er^{3+}. Additionally, radiative transition can occur between meta-stable states due to complex relaxation pathways. These emissions have wavelengths λ_{em} = 689 nm,

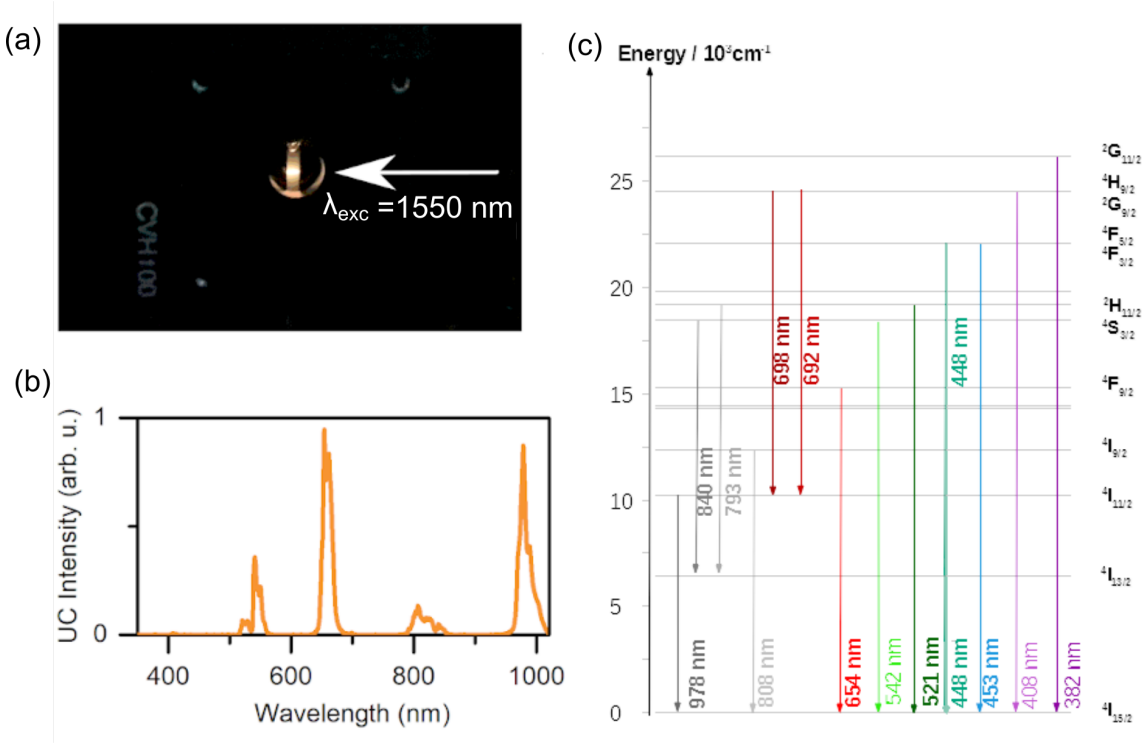

Figure 6.1: The luminescent properties of the β-$NaYF_4$:Er^{3+} UCNPs in c-Hexane solution. **(a)** A photographic image of the UC luminescence emission under 1551 nm laser excitation with P_{exc} = 39 W/cm^2, **(b)** the UC emission spectra between 350 nm and 1021 nm, and **(c)** the radiative transitions of the Er^{3+} ions. Adapted from Ahiboz *et al*. [79]

692 nm, 793 nm and 845 nm as shown in Fig. 6.1 (c).

Table-1 summarizes all observed radiative transitions and their corresponding peak emission wavelengths. The energy levels of Er^{3+} are categorized based on the number of photons with a wavelength of 1551 nm required to excite an electron from the ground state, and these levels are labeled as photon levels. For instance, to excite an electron from the ground state to $^4F_{9/2}$, $^4S_{3/2}$ and $^2H_{11/2}$ levels, at least 3 photons with a wavelength of 1551 nm must be absorbed. Therefore, these levels are labeled as 3-photon levels.

Table-1: Radiative transition of the Er^{3+} in UCNPs host			
λ_{em} (nm)	Initial state	Final state	Photon level
978	$^4I_{11/2}$	$^4I_{15/2}$	2-photon
840	$^4S_{3/2}$	$^4I_{13/2}$	3-photon
808	$^4I_{9/2}$	$^4I_{15/2}$	2-photon
793	$^2H_{11/2}$	$^4I_{13/2}$	3-photon
698	$^2H_{11/2}$	$^4I_{11/2}$	4-photon
692	$^2G_{9/2}$	$^4I_{11/2}$	4-photon
654	$^4F_{9/2}$	$^4I_{15/2}$	3-photon
542	$^4S_{3/2}$	$^4I_{15/2}$	3-photon
521	$^2H_{11/2}$	$^4I_{15/2}$	3-photon
453	$^4F_{5/2}$	$^4I_{15/2}$	4-photon
448	$^4F_{3/2}$	$^4I_{15/2}$	4-photon
408	$^2G_{9/2}$	$^4I_{15/2}$	5-photon
382	$^2G_{11/2}$	$^4I_{15/2}$	5-photon

6.2 Upconversion Dynamics of the β-$NaYF_4$:Er^{3+} UCNPs in Cyclo-Hexane

P_{exc} dependent UC intensity measurements are one of the common methods to explore the UC mechanism underlying the luminescent behavior of the Er^{3+} ions. It's a valuable technique to extract information on how energy levels are populated or depopulated. Moreover, the steady-state rate equation analysis based on the Eqn. 3.24-3.26 for various P_{exc} reveals the UC dynamics, such as radiative and non-radiative processes between the energy levels of a Er^{3+} ions. In this measurements, the P_{exc} increases systematically while keeping the λ_{exc} = 1551 nm. A cuvette containing β-$NaYF_4$:Er^{3+} UCNPs in c-Hexane solution is systematically excited with P_{exc} between 0.9 W/cm^2 and 40 W/cm^2 in the experimental setup depicted in Fig. 4.9 (d). The emission spectra of the β-$NaYF_4$:Er^{3+} UCNPs in c-hexane for various P_{exc} is shown in Fig. 6.2. The spectra in Fig. 6.2 in which the response of the UC emission to increasing P_{exc} is shown with blue to brown scale were recorded with an integration time of 50 s. The intensity of UC emission depends non-linearly on P_{exc}, however, the luminescence curves in Fig. 6.2 show that the response of the

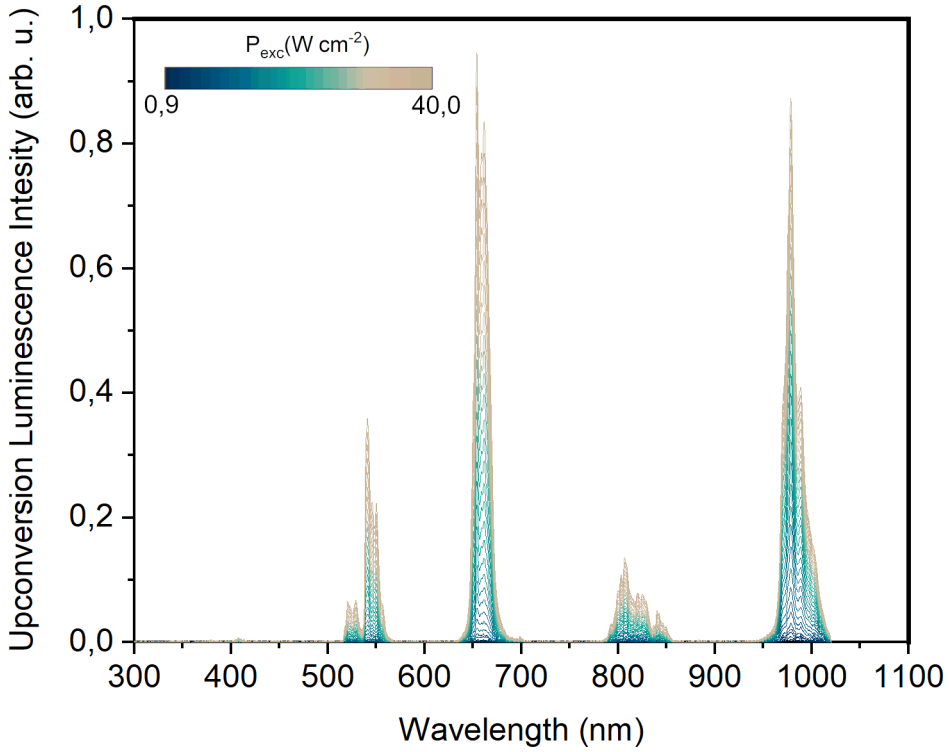

Figure 6.2: Upconversion emission spectra of the β-$NaYF_4$:Er^{3+} UCNPs in c-hexane as a function of P_{exc} between 0.9 W/cm^2 and 40 W/cm^2.

every emission band to is not the same: the dependence of the UC luminescence intensity on P_{exc} results in different emission intensity of the band. For example, the response of the green emission band to P_{exc} is greater than the response of the NIR emission bands in Fig. 6.2 when the P_{exc} increased from 0.9 W/cm^2 to 40 W/cm^2 systematically. The number of photons required for the excitation of a particular energy level can be an explanation of different trends in UC emission intensity of the emission bands. The power-law in Eqn. 3.27 predicts that emission from $^4I_{9/2}$ and $^4I_{11/2}$ to ground state $^4I_{15/2}$ of the Er^{3+} is proportional to ${P_{exc}}^2$ since these energy levels (1.24 eV and 1.53 eV with respect to ground state of Er^{3+}) can be populated by absorption of two 1551 nm photons (1.6 eV) via GSA + ESA or GSA + ET processes. Likewise, it is predicted that the emission from $^4F_{9/2}$, $^4S_{3/2}$ and $^2H_{11/2}$ levels to ground state level follow ${P_{exc}}^3$. A similar relation can be drawn for the emissions from higher energy states.

Slope values of UC emission by UCNPs: The peak value of the UC emission intensity of each emission band in Fig. 6.2 are plotted in Fig. 6.3 (a)-(h) as a function P_{exc} in double-logarithmic scale. The obtained curves are linearly fitted to extract slope values of the UC emission peaks by rearranging the Eqn. 3.27 as:

$$log(I) \propto n\, log(P_{\mathrm{exc}}) + const. \tag{6.1}$$

The fitted data shows two different trends; some of the emission peaks has single slope value (simply denoted as n) while the others have two distinct slope values at low-P_{exc} (n_1) and high-P_{exc} (n_2). For example, λ_{em} = 978 nm has two different n values: n_1 = 1.6 for low-P_{exc} (P_{exc} < 10 W/cm^2) whereas n_2 = 1.0 for high-P_{exc}. This behavior of the slope is not predicted by the power law. It is well-known fact that the power law has many assumptions, which are only valid under certain conditions [31]: It is only valid when the dominant depopulation mechanism for an energy level is the radiative transition to the ground state rather than to excitation to high energy levels [31]. In addition, the energy transfer between two dissimilar energy levels causes deviation from slope values predicted by the power law. For example, an electron occupying $^4I_{9/2}$ state of Er^{3+} transfers its energy to an electron in $^4I_{13/2}$ state of another Er^{3+} ion via CR that can lead to deviations on slope values predicted by power law.

The NIR emissions at λ_{em} = 978 nm, λ_{em} = 845 nm, λ_{em} = 820 nm and λ_{em} = 808 nm exhibit low-P_{exc} slope values between 1 and 2 in Fig. 6.3 (a)-(d) which can be a sign of 2-photon UC [164, 165]. Especially, λ_{em} = 845 nm shows quite a resemblance with two-photon UC with its slope n = 1.9 as predicted by the power-law. On the other hand, it is attributed to radiative transitions from $^4S_{3/2}$ to $^4I_{13/2}$ level which is shown in Fig. 6.1 (c) [161, 166]. This transition requires at least 3-photon energy. The n = 1.5 and n = 1.6 for λ_{em} = 808 nm and 825 nm follow same trend in P_{exc}; n remains same at two emission peaks. Both λ_{em} = 808 nm and λ_{em} = 825 nm belongs the same emission band which is yielded by $^4I_{9/2} \rightarrow {}^4I_{15/2}$ transitions [167]. λ_{em}= 978 nm emission has n_1 = 1.6 at low-P_{exc} but n_2 = 1.0 at high-P_{exc}. This is the an indication of a change in the way $^4I_{13/2}$ depopulated [124].

The slope values of the λ_{em} = 654 nm, λ_{em} = 542 nm and λ_{em} = 521 nm have two slope regimes at low-P_{exc} and high-P_{exc}. The values of n_1 for these three emission peaks vary between 2 and 3. Those values are attributed to the 3-photon upconversion [168, 169]. The λ_{em} = 542 nm and λ_{em} = 521 nm has nearly identical slope

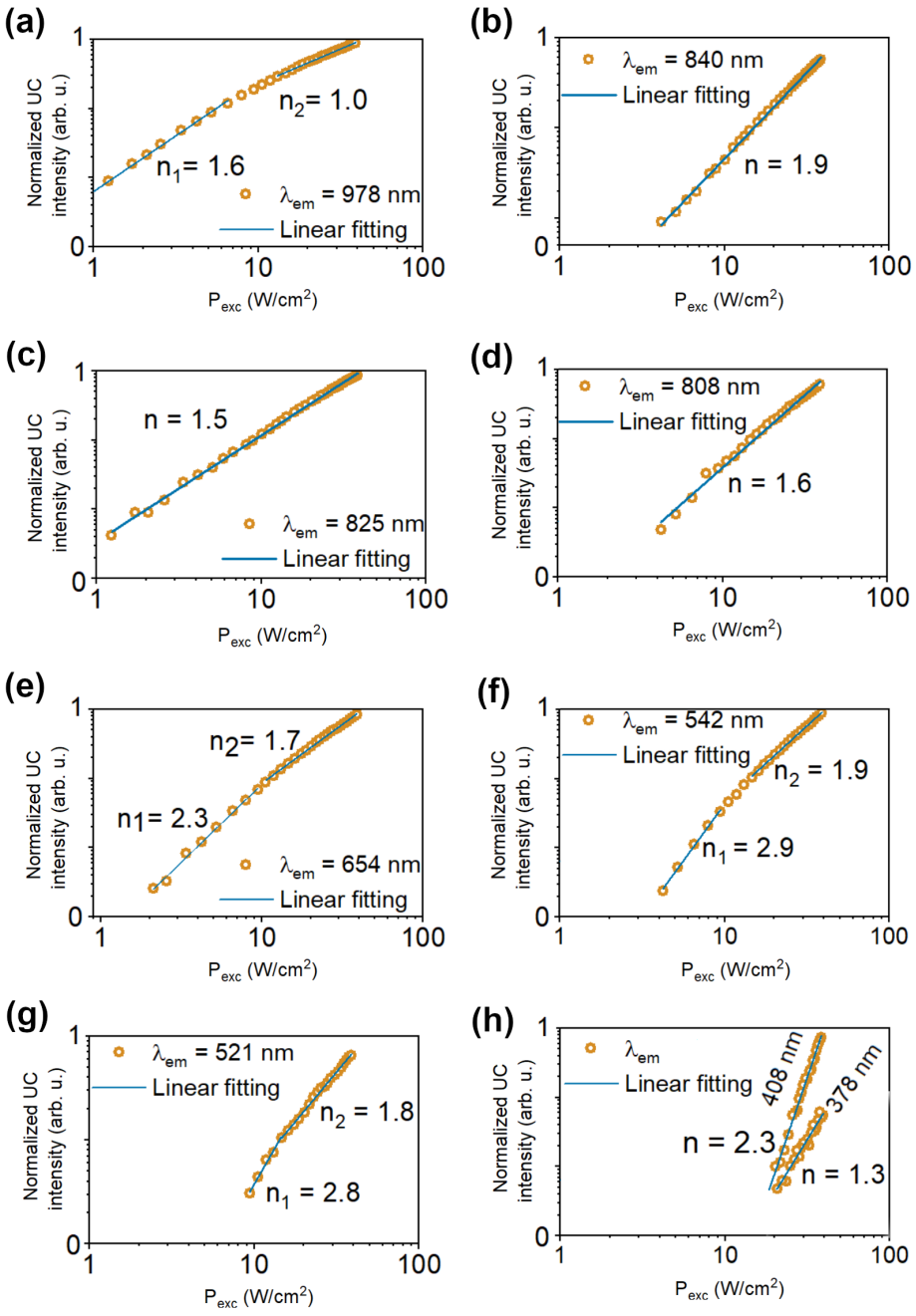

Figure 6.3: Upconversion emission intensities as function of excitation power density at λ_{exc} = (a) 1551 nm in double logarithmic scale. λ_{em} = (a) 978 nm, (b) 840 nm, (c) 825 nm, (d) 808 nm, (e) 654 nm, (f) 542 nm, (g) 521 nm, (h) 408 nm and 378 nm. The slope values with subscripts n_1 and n_2 indicate the slope values at low- and high-P_{exc}, respectively. The slope value n without subscript is used for the curves having a single slope value for both low-and high-P_{exc}.

values, n_1 = 2.9 and n_1 = 2.8, but λ_{em} = 654 nm has a slope value n_1 = 2.3. The deviation from the slope value of λ_{em} = 542 nm is a sign of differences underlying the UC mechanism of those energy states' population. Furthermore, those 3-photon UC emissions have significantly similar n_2 values of between 1.7-1.9. In addition, the change in slope values in Fig.6.3 (e)-(g) occurs at the same P_{exc} (~10 W/cm^2) as λ_{em} = 978 nm does in Fig.6.3 (a). This may imply that the population of these states ($^2H_{11/2}$, $^4S_{3/2}$ and $^4F_{9/2}$) are affected by how $^4I_{11/2}$ state is depopulated. For example, these states can be populated by ET from $^4I_{11/2}$.

The slope values for λ_{em} = 408 nm and λ_{em} = 378 nm are measured as n = 2.3 and n= 1.3. It's not possible to conclude about the dynamics of the transition leading those emissions since only the data in high-P_{exc} regime is available due to limitation on the detection capabilities of the experimental setup described in Fig. 4.9 (d). Furthermore, the UC emission from 4-photon energy levels ($^4F_{5/2}$ and $^4F_{3/2}$) at λ_{em} = 453 nm and λ_{em} = 448 nm are detectable with very high-P_{exc} in the experimental setup in Fig. 4.9 (d), however, not enough data points were able to be collected for statistical convenience. Therefore, no slope values for the blue emissions are reported here.

Modelling the P_{exc} dependend UC emission intensity: The slope values in Fig. 6.3 (a)-(g) deviates greatly from the slope values expected by the power law as discussed above. Only the slope values of λ_{em} = 542 nm and λ_{em} = 521 nm emissions obey the power-law. Nevertheless, the rate equation analysis stated in Eqn. 3.24-3.26 is needed to comprehend the UC dynamic of the UCNPs. An energy level diagram of the β-NaYF4:Er^{3+} UCNPs is proposed in Fig. 6.4 which explains population and depopulation routes of the energy levels of the β-$NaYF_4$:Er^{3+} UCNPs. This diagram represents the energy levels or all Er^{3+} contents of the UCNPs collectively on which the rate equation analysis is based. The following assumptions are made before steady-state solution of the rate equations:

1) Radiative transitions between the metastable states are considered as a small perturbation on population and de-population of the energy levels of Er^{3+}. Therefore, they are not involved in rate equations [124].

2) The UCNPs used in this experiment has 28.5 % Er^{3+} content. This means that ETU is the dominant UC mechanism over ESA-UC [124]. Hence, ESA is ignored in rate equations.

3) Since the 4- and 5-photon UC require enormously intense P_{exc}, the rate equa-

tion analysis is limited by 3-photon UC, namely 7-level energy system.

4) ET happens between N_1 and N_i levels, considering the fact that N_1 is populated before the other levels do.

The rate equations of the energy levels depicted in Fig. 6.4 are given as [31, 124, 131]:

$$\frac{dN_0}{dt} = -GN_0 + W_{ET1}N_1^2 + W_{ET2}N_1N_2 + W_{ET3}N_1N_3 + \sum_{i=1}^{6} k_{i0} \tag{6.2}$$

$$\frac{dN_1}{dt} = GN_0 - 2W_{ET1}N_1^2 - W_{ET2}N_1N_2 - W_{ET3}N_1N_3 - k_{10}N_1 \tag{6.3}$$

$$\frac{dN_2}{dt} = W_{MPR1}N_3 - W_{ET2}N_1N_2 - k_{20}N_2 \tag{6.4}$$

$$\frac{dN_3}{dt} = W_{ET1}N_1^2 - W_{MPR1}N_3 - W_{ET3}N_1N_3 - k_{30}N_3 \tag{6.5}$$

$$\frac{dN_4}{dt} = W_{ET3}N_1N_3 + W_{MPR2}N_6 + W_{MPR3}N_5 - k_{40}N_4 \tag{6.6}$$

$$\frac{dN_5}{dt} = W_{MPR4}N_6 - W_{MPR3}N_5 - k_{50}N_5 \tag{6.7}$$

$$\frac{dN_6}{dt} = W_{ET3}N_1N_3 - W_{MPR4}N_6 - W_{MPR4}N_6 - k_{60}N_6 \tag{6.8}$$

Where N_n (n = 0-6) is the population density of the n-th electronic level, G is the generation rate. W_{ET1},W_{ET2} and W_{ET3} are the probabilities of energy transfer ET-1, ET-2 and ET-3, while W_{MPR1},W_{MPR2},W_{MPR3} and W_{MPR4} are the probabilities of the multi-phonon relaxations MPR-1, MPR-2, MPR-3 and MPR-4, in Fig. 6.4 respectively. The indexed k_{i0} is the radiative transition probability from the i-th energy level to the ground state.

UC dynamics in low-P_{exc} regime: At low-P_{exc}, the N_1 level is populated by the GSA with the rate of G whereas the depopulation of this level mainly achieved through the ground state relaxation rather than excitation to upper states. Therefore, the term $k_{10}N_1$ dominates over the other terms of depopulation in Eqn. 6.3 and those terms can be ignored. This is a reasonable assumption considering that the absorption cross-section of the Er^{3+} is in the order of 10^{-21} cm^2 [170, 171]. The steady-state solution for the energy levels, $\frac{dN_n}{dt} = 0$, the N_1 becomes by using the

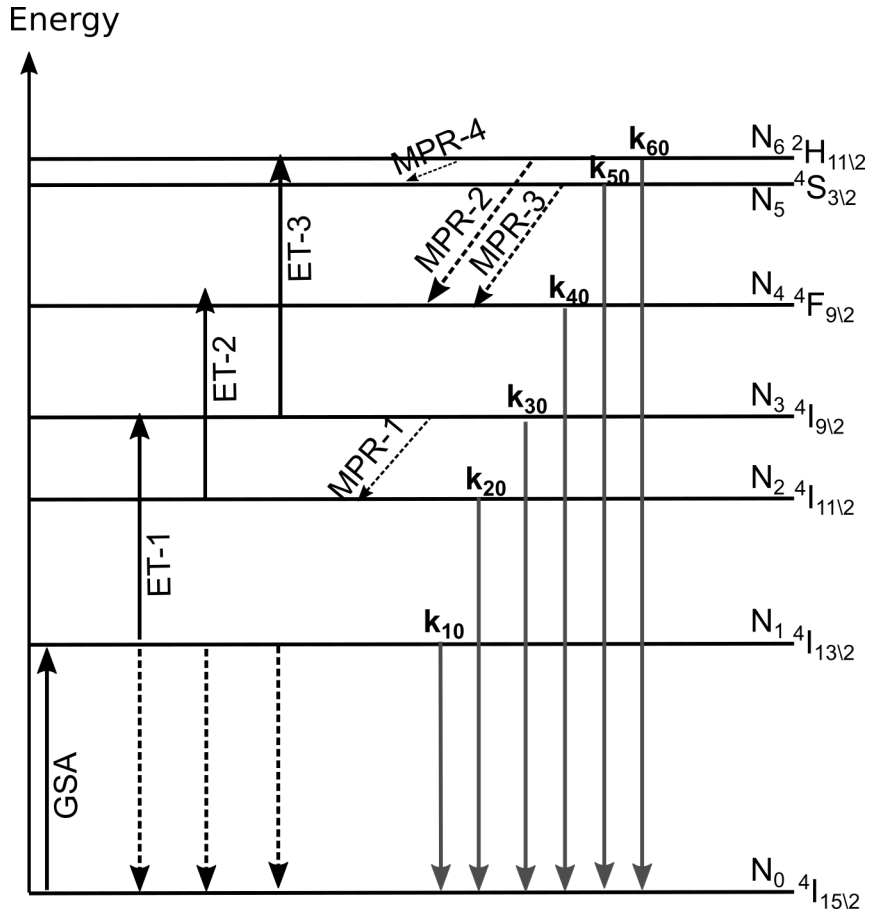

Figure 6.4: Energy levels of Erbium: Upward solid arrows indicate electron excitation to upper states. Downward solid arrows shows radiative transitions to the ground state of Er^{3+} while the downward dashed arrows represents non-readiative relaxation of the electrons due to energy transfer. Multi-phonon processes are shown by diagonal dashed arrows.

Eqn. 3.13:

$$N_1 = \frac{GN_0}{k_{01}} = \frac{\sigma_{01}(\omega)}{k_{01}\hbar\omega} P_{exc} \tag{6.9}$$

where $\sigma_{01}(\omega)$ and $\hbar\omega$ is the absorption cross-section of $^4I_{15/2} \rightarrow {}^4I_{13/2}$ transition for angular frequency of the laser excitation ω = 1215 s^{-1} (λ_{exc}=1551 nm) and the energy of a single 1551 nm photon (0.79 eV).

The population densities N_2 and N_3 are thermally coupled via MPR. There exists no population channel of $^4I_{11/2}$ from lower laying states via direct excitation by absorption of the λ_{exc}=1551 nm photons. The only population route for $^4I_{11/2}$ levels is the radiative or non-radiative relaxation of the higher energy states. Considering

the fact that no radiative transition was recorded in the spectral measurements, $^4I_{11/2}$ states can be populated by CR, ET, or MPR. Since the population densities of the 3- or more photon energy levels are sparse at low-P_{exc}, the MPR is a more probable population route. The energy difference between $^4I_{11/2}$ and $^4I_{9/2}$ states is roughly 2150 cm^{-1}, which is 5-6 times greater than maximum phonon energies of the β-$NaYF_4$:Er^{3+} nanocrystals ($\simeq$ 350-400 cm^{-1}) [172–174]. By revisiting the phonon gap law, it is expected that the MPR-1 in Fig. 6.4 becomes the main depopulation route of the $^4I_{9/2}$. The term W_{MPR1} dominates over the other depopulation term W_{ET1} in Eqn. 6.5. The effect of the MPR-1 can be seen in Fig. 6.2; the intensity of the λ_{em} = 978 nm emission is always greater than the intensity λ_{em} = 808 nm emission which means that the emission at λ_{em} = 808 nm is heavily quenched by MPR-1 process since the emission intensity λ_{em} = 808 nm $\propto k_{30}N_3$. Nevertheless, population densities N_2 and N_3 can be approximated as:

$$N_2 = \frac{W_{MPR1}W_{ET1}}{k_{10}^2 k_{20}(W_{MPR1} + k_{30})}\left(\frac{\sigma_{01}(\omega)}{\hbar\omega}\right)^2 (P_{exc})^2 \tag{6.10}$$

$$N_3 = \frac{W_{MPR1}W_{ET1}}{(k_{10}^2 + k_{30})}\left(\frac{\sigma_{01}(\omega)}{\hbar\omega}\right)^2 (P_{exc})^2 \tag{6.11}$$

The power dependence, hence the intensity of the UC emission, in Eqn. 6.10 and 6.11 have a quadratic relation with P_{exc}. However, the expected slope value at low-P_{exc} by Eqn. 6.10 and Eqn. 6.11 n_1 = 2.0 differs from the slope value extracted from the experimental data n_1 = 1.6. The difference between two slope values can be originated from either a process or mechanism which is responsible for the population and depopulation of the $^4I_{13/2}$ or population of the $^4I_{9/2}$ which is not considered in Eqn. 6.5. This will be discussed later in this chapter. Nonetheless, Eqn. 6.10 and Eqn. 6.11 explains why λ_{em} = 978 nm and λ_{em} = 808 nm emission intensities have the same slope value at low-P_{exc}: The $^4I_{11/2}$ level populated by the depopulation of $^4I_{9/2}$ level via MPR-1.

The $^4F_{9/2}$ is thermally coupled via MPR-2 and MPR-3 to $^2H_{11/2}$ and $^4S_{3/2}$. Similarly, $^2H_{11/2}$ has a depopulation channel to $^4S_{3/2}$ via MPR-4 as shown in Fig. 6.4. However, all of those three energy levels are able to be populated by energy transfer from low-laying energy states and the CR and ET processes involving higher energy levels, unlike the 2-photon level $^4I_{11/2}$. Moreover, at low-P_{exc}, the population of the 4- and 5-photon energy levels, and accordingly their radiative or non-radiative relaxation

to the 3-photon energy levels, are expected to be insignificant. The UC emission from 4- and 5-photon levels at low-P_{exc} are beyond the detection capabilities of the experimental setup. Therefore, those effects are neglected while forming the rate equations.

$^4F_{9/2}$ level can be populated by energy transfer ET-2 effectively besides MPR-2 amd MPR-3. $^2H_{11/2}$ can be populated by via MPR-4 process. On the other hand, $^4S_{3/2}$ can be populated by ET-3. Considering all mentioned facts and assumptions above, the equations giving the N_4, N_5 and N_6 are:

$$N_4 = \left[\frac{k_{10}^2 W_{ET2} W_{MPR1} \hbar\omega}{(W_{MPR1}+k_{30})(W_{ET2}(\sigma_{01}P_{exc}+k_{10}^2 k_{20}))} + \frac{((W_{MPR3}+k_{50})W_{MPR2}+W_{MPR3}W_{MPR4})W_{ET5}W_{ET1}}{(W_{MPR3}+k_{50})(W_{MPR2}+W_{MPR4}+k_{60})(W_{MPR1}+k_{30})} \right] \frac{(\sigma_{01}(\omega))^3}{k_{40}k_{10}^3(\hbar\omega)^3}(P_{exc})^3 \quad (6.12)$$

$$N_5 = \frac{W_{ET1}W_{ET5}(\sigma_{01}(\omega))^3}{k_{10}^3 k_{40}(W_{MPR3}+k_{50})(W_{MPR2}+M_{MPR4}+k_{60})(W_{MPR1}+k_{30})}(P_{exc})^3 \quad (6.13)$$

$$N_6 = \frac{W_{ET1}W_{ET5}(\sigma_{01}(\omega))^3}{k_{10}^3(W_{MPR2}+M_{MPR4}+k_{60})(W_{MPR1}+k_{30})(\hbar\omega)^3}(P_{exc})^3 \quad (6.14)$$

The population densities N_6 and N_5 depends on the third power of the P_{exc}. The emission intensities for λ_{em} = 542 nm and λ_{em} = 521 nm show the relation $I_{521} \propto k_{60}N_6 \propto P_{exc}^3$ and $I_{542} \propto k_{50}N_5 \propto P_{exc}^3$. The Eqn.6.13 and Eqn.6.14 predict a slope value n_1 = 3.0, which is in excellent agreement with observed slope values n_1 = 2.9 for λ_{em} = 542 nm and n_1 = 2.8 for λ_{em} = 521 nm in Fig.6.3 (f) and (g), respectively. On the other hand, the presence of the P_{exc} in the denominator of the first term inside the square brackets in Eqn. 6.12 reduces the value of the slope. Therefore, the experimental slope value n_1 = 2.3 can be explained by the population of $^4F_{9/2}$ level by ET-2 process.

UC dynamics in high-P_{exc} regime: The depopulation mechanism of the $^4I_{13/2}$ level is dominated by the excitation to energetic states at high-P_{exc}. The term $2W_{ET1}N_1^2$ in Eqn. 6.3 dominates over $k_{10}N_1$ and the other ET terms. The population density N_1 becomes:

$$N_1 = \left(\frac{GN_0}{2W_{ET1}}\right)^{1/2} = \left(\frac{\sigma_{01}(\omega)}{2W_{ET1}\hbar\omega}\right)^{1/2}(P_{exc})^{1/2} \quad (6.15)$$

The 2-photon levels can be expressed as:

$$N_2 = \frac{W_{MPR1} W_{ET1} \sigma_{01}(\omega)}{2W_{MPR1} k_{20} (W_{MPR1} + k_{30}) \hbar\omega} P_{exc} \tag{6.16}$$

$$N_3 = \frac{W_{ET1} \sigma_{01}(\omega)}{2W_{MPR1} (W_{MPR1} + k_{30}) \hbar\omega} P_{exc} \tag{6.17}$$

The UC emissions at λ_{em} = 978 nm and λ_{em} = 808 nm are expected to be linearly P_{exc} dependent. When the predicted slope value n_2 = 1 for λ_{em} = 978 nm in Eqn. 6.16 is compared to the slope value n_2 = 1.0 of experimental data in Fig. 6.3(a), the agreement between them is excellent. However, although a slope values change is predicted for λ_{em} = 808 nm, n = 1.6 remains same of this wavelength at high-P_{exc}. This can be caused by the population of the $^4I_{9/2}$ by upper states, i.e. 4-photon levels, via CR processes.

The population densities of the 3-photon levels N_4, N_5 and N_6 at high-P_{exc} are derived as:

$$N_4 = \left[\frac{2W_{ET1} W_{ET2} W_{MPR1} \hbar\omega}{(W_{MPR1} + k_{30})(W_{ET2}(\sigma_{01} P_{exc}))^{1/2} + 2W_{ET1} k_{20})} \right] + \left[\frac{((W_{MPR3} + k_{50}) W_{MPR2} + W_{MPR3} W_{MPR4}) W_{ET5} W_{ET1}}{(W_{MPR3} + k_{50})(W_{MPR2} + W_{MPR4} + k_{60})(W_{MPR1} + k_{30})} \right] \frac{(\sigma_{01}(\omega))^{3/2}}{k_{40}(2W_{ET1})^{3/2} (\hbar\omega)^{3/2}} (P_{exc})^{3/2} \tag{6.18}$$

$$N_5 = \frac{W_{ET5} (\sigma_{01}(\omega))^{3/2}}{2W_{ET1}^{3/2} k_{40} (W_{MPR3} + k_{50})(W_{MPR2} + M_{MPR4} + k_{60})(W_{MPR1} + k_{30})(\hbar\omega)^{3/2}} (P_{exc})^{3/2} \tag{6.19}$$

$$N_6 = \frac{W_{ET5} (\sigma_{01}(\omega))^{3/2}}{2W_{ET1}^{3/2} (W_{MPR2} + M_{MPR4} + k_{60})(W_{MPR1} + k_{30})(\hbar\omega)^{3/2}} (P_{exc})^{3/2} \tag{6.20}$$

The slope value for λ_{em} = 654 nm is predicted by Eqn. 6.18 as $1 < n_2 \leq 1.5$. The measured n_2 = 1.7 is greater than what is predicted for λ_{em} = 654 nm. The λ_{em} = 542 nm and λ_{em} = 521 nm emissions posses high-P_{exc} slopes n_2 = 1.9 and = 1.8, respectively. These values are greater than the n_2 values predicted by Eqn. 6.19 and Eqn. 6.20: n = 1.5. It is an observed common fact that the slope values are different from the predicted values when the concentration of Er^{3+} ions in the host

crystal increases since increasing inter-ionic dipole interactions can underpin the CR process [124, 175]. The small slope values for the 4-photon levels and 5-photon levels emissions, $n = 2.3$ for $\lambda_{em} = 408\,nm$ and $n = 1.3$ for $\lambda_{em} = 378\,nm$, may indicate more complex population and depopulation of the energy levels at high-P_{exc}. Although the blue emitting levels $^4F_{5/2}$ and $^4F_{3/2}$ in Fig. 6.5 are less energetic than $^2G_{11/2}$, $\lambda_{em} = 453\,nm$ and $\lambda_{em} = 453\,nm$ is less intense than $\lambda_{em} = 382\,nm$. The blue emitting levels, $^4F_{5/2}$ and $^4F_{3/2}$, can be populated by MPR from 4-photon levels $^4F_{5/2}$ and $^2G_{9/2}$ and $^4F_{5/2}$ and $^2H_{9/2}$ levels via MPR. However, one step (direct) excitation of the 4-photon levels of the Er^{3+} is needed to explore the mechanism which is responsible for quenching $\lambda_{em} = 453\,nm$ and $\lambda_{em} = 448\,nm$ emission.

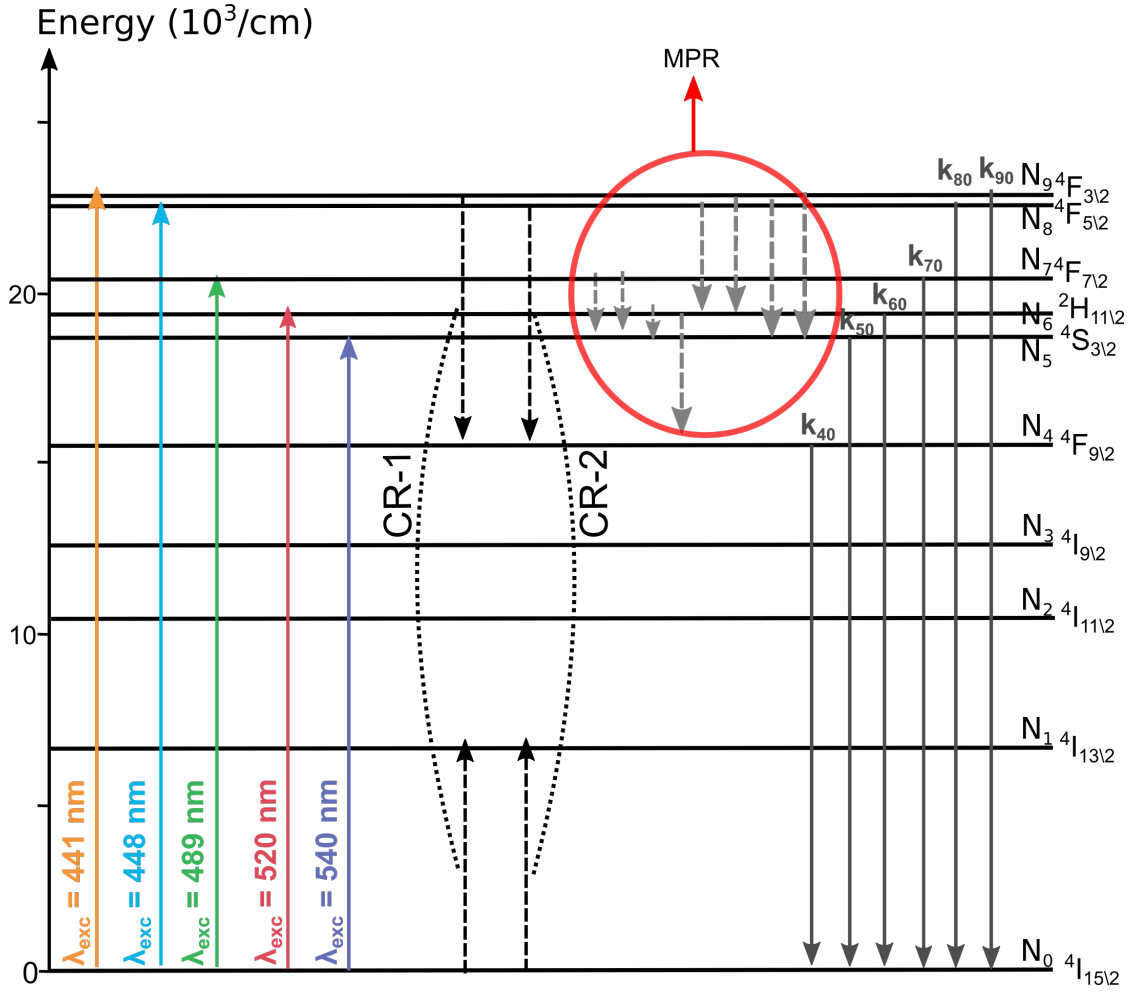

Figure 6.5: An energy level diagram showing the excited meta-stable states of Er^{3+} by $\lambda_{exc} = 441\,nm$, $448\,nm$, $489\,nm$, $520\,nm$ and $540\,nm$. The red circle indicates MPR between meta-stable states.

Direct excitation of the energy levels of Er^{3+} by laser: To explore the effect of the interaction of the higher energy levels, the $^4F_{3/2}$, $^4F_{5/2}$, $^4F_{7/2}$, $^2H_{11/2}$ and $^4S_{3/2}$ states are excited by GSA via laser with various λ_{exc}. The luminescence spectra recorded after GSA are shown in Fig. 6.5. These excitation wavelengths are indicated as colored upright arrow which also shows the excited energy levels. The λ_{exc} used for direct excitation of the energy levels slightly vary from the wavelength of the emission peaks of the Er^{3+} in Fig. 6.2. In this choice the fact that the maximum value absorption and emission cross-sections differ from each other [170, 171]. The excitation of the $^4F_{3/2}$ and $^4F_{5/2}$ levels are done by $\lambda_{exc} = 441\,nm$ and $\lambda_{exc} = 448\,nm$. The GSA at these wavelengths are followed by emissions at $\lambda_{em} = 521\,nm$, $\lambda_{em} = 541\,nm$ and $\lambda_{em} = 654\,nm$. By inspecting the difference between the energy levels of the energy diagram in Fig. 6.5, it is concluded that $^4F_{3/2}$ and $^4F_{5/2}$ levels relaxes via MPR to $^4S_{3/2}$ and $^2H_{11/2}$, and via CR process to $^4F_{9/2}$ as shown in Fig. 6.6. However, the

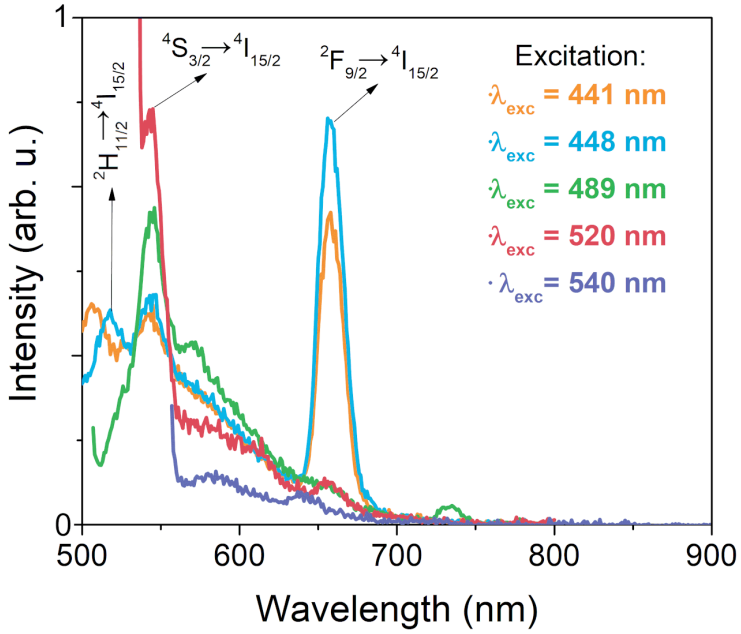

Figure 6.6: Luminescence of β-$NaYF_4$:Er^{3+} by direct excitation of the meta-stable states of Er^{3+}, courtesy of Dr. Elina Andresen.

intense red emission indicates that the CR process dominates over MPR to the depopulation of the $^4F_{3/2}$ and $^4F_{5/2}$ levels. The excitation of the $^4F_{7/2}$ results in red and green emissions but contrary to the excitation of the $^4F_{3/2}$ and $^4F_{5/2}$ levels, the green

emission is intense than the red emission. This means that the MPR can be the dominant mechanism of the depopulation of the $^4F_{7/2}$ level. Compared with the UC experiment, those three blue emitting levels are cannot be direct without depopulation of the higher energy levels or lower laying levels with $\lambda_{exc} = 1551\,nm$. Those states can be populated by MPR and CR from $^2G_{11/2}$, $^2G_{9/2}$ and $^2H_{9/2}$ levels. The MPR from $^2G_{11/2}$ and $^2H_{11/2}$ to $^4F_{9/2}$ since MPR probability is low considering the energy gap between those states. Therefore, $\lambda_{em} = 489\,nm$ couldn't be observed during UC experiments. On the other hand, $\lambda_{em} = 448\,nm$ and $\lambda_{exc} = 453\,nm$ were detected at very high-P_{exc}. Although, $^4F_{5/2}$ and $^4F_{3/2}$ can be populated via MPR process, the emission from those states are heavily quenched and consequently, underpin the strong red emission with $\lambda_{em} = 654\,nm$ due to CR [175]. The excitation of the 3-photon levels with $\lambda_{exc} = 520\,nm$ and $\lambda_{exc} = 540\,nm$. These excitations lead to the red mission at $\lambda_{em} = 654\,nm$ via MPR as expected. Nevertheless, the GSA absorption of the 3- and 4-photon levels show that the CR relaxation also takes place in UC dynamics. No significant emission at $\lambda_{em} = 808\,nm$ is seen in Fig. 6.6 which can be an indication of that $^4I_{9/2}$ does not involve CR process, $^4I_{11/2}$ and $^4I_{13/2}$ interacts 4- and 5-photons levels. Thus, these interactions can affect and result in different slope values for λ_{em} than expected.

7

The Enhanced Photon Upconversion of Er^{3+} and Yb^{3+} doped β-$NaYF_4$ Upconversion Nanoparticles on Silicon Metasurfaces

7.1 The Enhanced Photon Upconversion of β-$NaYF_4$: Er^{3+} Upconversion Nanoparticles on Silicon Metasurface upon 1550 nm Excitation

In this section, metasurface enhanced UC is demonstrated, and the effect of the coupling between leaky mode of the Si metasurface - laser excitation at λ_{exc} = 1551 nm on the luminescence intensity and the UC dynamics of β-$NaYF_4$:Er^{3+} UCNPs are investigated. The UCNPs that are investigated in Chapter-6 are used for the experiments that are subjected to this chapter. The Si metasurface that is subjected to this section was produced and all the optical characterizations and measurements on UCNP deposited Si metasurfaces by Doguscan Ahiboz at Helmholtz-Zentrum Berlin (HZB). The β-$NaYF_4$:Er^{3+} UCNPs are produced by Dr. Elina Andresen at Bundesanstalt für Materialforschung und -prüfung (BAM). The numerical calculations and simulations were performed by Dr. Phillip Manley (JCMwave GmbH). The SEM pictures were taken by Karola Klimm at Helmholtz-Zentrum Berlin (HZB). The Si metasurface and their characterization, and UC measurements of the UCNPs covered metasurfaces were done by Doguscan Ahiboz at HZB.

Considering the experimental and computational findings of Chapter 4.1, the thickness of the Si metasurfaces with p = 1000 nm is optimized for enhancing ab-

sorption of 1551 nm photons by Er^{3+} doped UCNPs on the metasurface. Since the metasurfaces with p = 1000 nm in Fig. 5.3 shows several leaky modes resonant at the NIR-III window. Moreover, the effect of the UCNPs layer on the spectral position of the leaky modes of the Si metasurface is also considered. The dielectric contrast across the interface between the UCNPs layer and Si (0.45) is weaker than the air-Si interface (0.55) for λ_{exc} = 1551 nm, consequently, the spectral position of the leaky modes are expected to shift longer wavelengths [149, 150]. The amount of the spectral shift is estimated as 50 nm. Therefore, optimization t_{Si} is done as if λ_{exc} = 1500 nm. In that way, the leaky modes resonances' can be shifted towards 1551 nm after UCNPs layer formation on the Si metasurface. Nonetheless, the silicon thickness optimized at t_{Si} = 50 nm so that absorption of the 1551 nm photons by Er^{3+} ions can increase.

An SEM cross-section image of the produced Si metasurface on a glass substrate shows excellent UCNP coverage on the Si metasurface in Fig. 7.1 (a). It is challenging to produce a large area (25 cm^2) Si metasurface at an exact thickness since production requires multiple material processing steps and each step introduces structural imperfections inheritedly. As a result, the extracted t_{Si} = 53 nm differs from the intended silicon thickness of 50 nm by 3 nm. The UCNPs are placed on Si metasurface drop-wise, which are shown in the SEM top-view image in Fig. 7.1 (b) as SEM top-view image. A cross-section image in Fig. 7.1 (c) shows the UCNPs layer with an average thickness of 660 nm. After a close inspection of the Fig. 7.1(c), a thin planar layer can be recognized on top of β-$NaYF_4$:Er^{3+} UCNP layer, however, it is thought to be a measurement artifact that originated from charging effects of the surface. This layer only appears in SEM cross-section images, while there is no evidence for the presence of such a layer on top of the UCNP layer, as it can be distinguished in Fig. 7.1 (c).

7.1.1 Interaction between the leaky modes of the Si netasurface and β-$NaYF_4$:Er^{3+} UCNPs layer

ARLM of the β-$NaYF_4$:Er^{3+} UCNPs on Si metasurface are conducted with polarized laser light, inside an integrating sphere. The sample is inserted in the middle position of the integrating sphere via a rotatable sample holder. The excitation source with λ_{exc} = 1551 nm and P_{exc} = 30 W/cm^2 set to launch on the rotation axis of the sample holder so that displacement of excitation spot is negligible the sam-

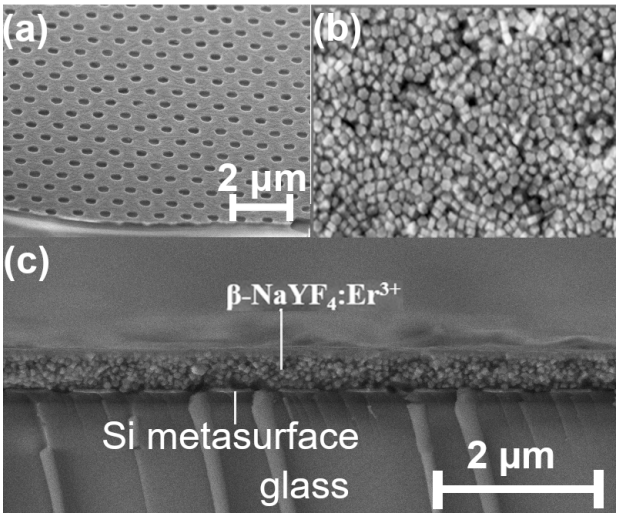

Figure 7.1: SEM images of the (a) Si metasurface with 53 nm thickness (b) β-$NaYF_4$:Er^{3+} UCNPs on Si metasurface, and (c) 660 nm thick UCNP layer on the Si metasurface. Taken from Ahiboz *et al*. [79].

ple holder rotates around its rotation axis. The sample is rotated through the high symmetry direction of the Si metasurface $\Gamma \rightarrow$ M, from normal incidence to $\theta = 40°$, with both TE and TM polarized light to resolve TE and TM leaky modes of the Si metasurface. The θ is increased in 2° steps and corresponding luminescence spectra are recorded and integrated from 350 nm - 1020 nm at every θ. The integrated luminescence on the Si metasurface with TE polarized light is shown in the left panel of Fig. 7.2 (a), while the UC luminescence with TM polarized light is shared on the right-hand side of the Fig. 7.2 (a). A vast increase in the luminescence of the UCNPs on the Si metasurface is observed in four different θ intervals, two of them are under TE polarized excitation and the others are under TM polarized excitation, which is thought to be an effect of near fields supported by the Si metasurface on increasing absorption of Er^{3+}. The angular position of the emission peaks are observed at $\theta = 8° \pm 1°$ and $\theta = 18° \pm 1°$ with the TE polarized light while $\theta = 14° \pm 1°$ and $\theta = 26° \pm 1°$ with the TE polarized light. To clarify the source of the luminescence enhancement at the mentioned four angles, the presence of the leaky modes of the Si metasurface is analyzed by ARRM in Fig. 7.2 (b). In these measurements, β-$NaYF_4$:Er^{3+} UCNPs on Si metasurface are excited with a polychromatic light source with λ_{exc} between 1400 nm and 1700 nm. The excitation wavelengths are changed by 2 nm steps for each θ between 0° and 40° through $\Gamma \rightarrow$ M high symmetry direction. Moreover, the position of the excitation beam area was meticulously

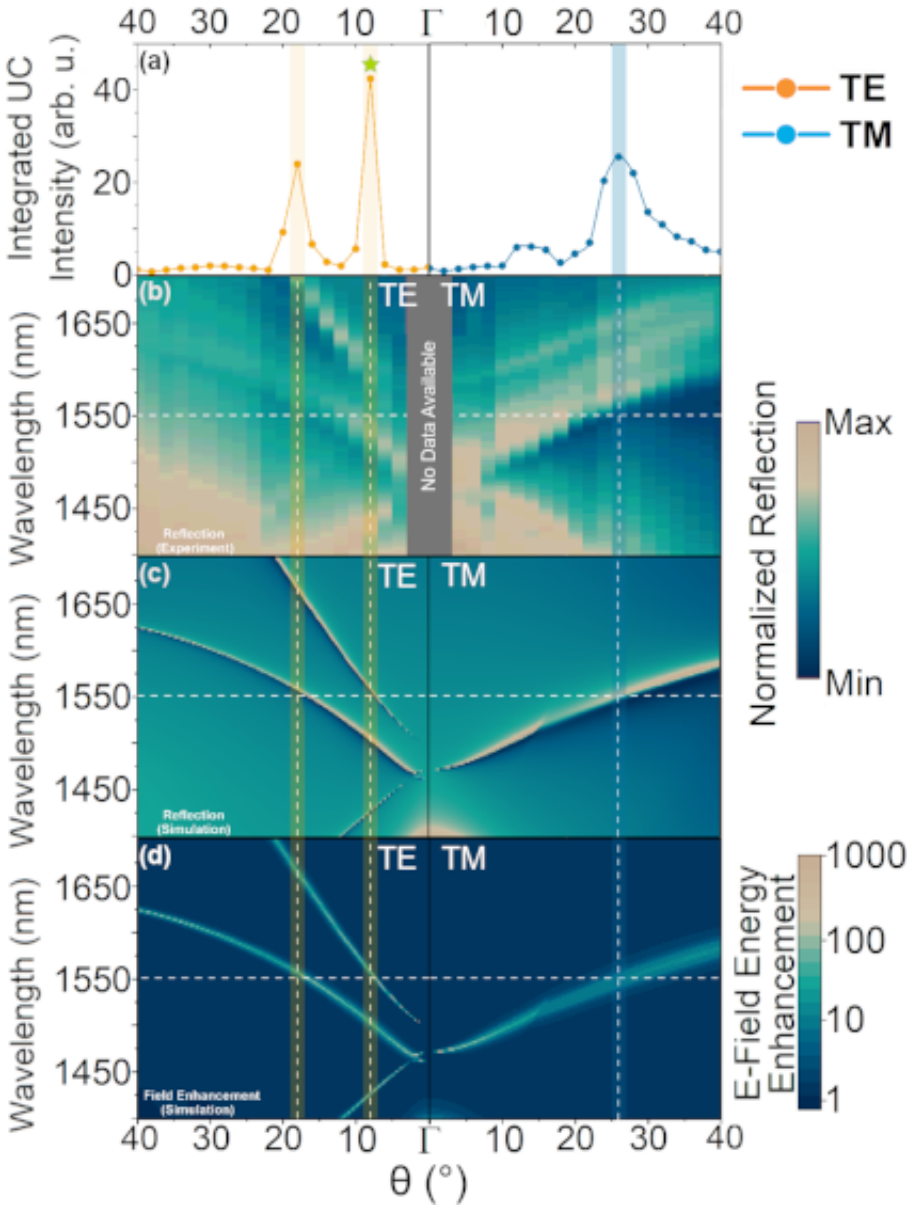

Figure 7.2: Angular resolved measurements: (a) Integrated UC emission (λ_{em}=350 nm-λ_{em}=1020 nm) from β-$NaYF_4$:Er^{3+} UCNPs on silicon metasurface as function of angle of incidence (θ) for rotation in $\Gamma \rightarrow$M high symmetry direction using TE (left) and TM (right) polarized 1551 nm radiation for excitation (P_{exc} = 30 W/cm^2). (b) the measured and (c) simulated reflectance of the β-$NaYF_4$:Er^{3+} UCNPs covered Si metasurface. The color bar ranges from 15 % to 50 % for a better visibility in (b) and from 0 to 1 for (c). (d) Calculated enhancement of the electrical near-field energy inside the β-$NaYF_4$:Er^{3+} UCNPs layer volume (compared to the respective electric field energy in the same volume in free space). White dashed lines represent laser excitation wavelength at 1551 nm while orange and blue shaded white lines present the angle of incidences where the peaks of UC emission are observed. Taken from Ahiboz *et al*. [79].

set in the same position as that was excited in the ARLM measurement. Therefore, more reliable results are obtained by avoiding local effects, such as imperfections on nanostructures, on spectral positions of the leaky modes. The resonance patterns, i.e. sharp changes between reflection maximum and minimum, in the reflection spectra of the integrated UC luminescence hint at the possibility of the strong near fields enhancing the absorption of the excitation [55]. The spectral and angular dispersion of the leaky modes of the Si metasurface reveals the possibility of coupling of 1551 nm excitation (shown as dashed white horizontal lines through the Fig. 7.2 (b) - (d)) and the leaky modes of the Si metasurface. The resonant features in the reflection spectra (dark and bright lines) appear at 1551 nm for the same θ as luminescence peaks appear at, thereby, leaky modes might be present on the Si metasurface. To justify the existence of the leaky modes, a FEM simulation of the ARRM is performed, and the simulation results are presented in Fig. 7.2 (c). An exceptional agreement between spectral dispersion of the leaky modes (Fig. 7.2(b) and Fig. 7.2 (c)) and the ARLM results (Fig. 7.2 (a)) is accomplished. Therefore, it can be an indication of the coupling between incident radiation and leaky modes of the Si metasurface which is expected to create strong near-field effects on the metasurface. However, the ARRM simulation results show no sign of leaky modes at θ = 14° for the TM polarized light, whereas the ARLM peak in Fig. 7.2 (a) (right panel) and resonance pattern in ARRM Fig. 7.2 (a) (right panel) exhibit. The TM mode at θ = 14° is attributed to the contribution from the leaky modes that exist under rotation through high symmetry direction $\Gamma \rightarrow$ K. The discrepancy between measurement and simulation was analyzed further by the ARDT measurements. The zeroth order transmission spectra under rotations through $\Gamma \rightarrow$ M and $\Gamma \rightarrow$ M are compared in Fig. 7.3 with TM polarized light. λ_{exc}, which is indicated as a horizontal red shaded line in Fig. 7.3, shifts towards 1500 nm to compensate for reduced dielectric constant due to the presence of the UCNP layer on metasurface, as discussed above. The presence of the TM leaky mode on the Si metasurface in the $\Gamma \rightarrow$ K direction is clearly seen in the left-hand side of Fig. 7.3 (intersection of the yellow shaded vertical line and red shaded line) at θ = 14°. The source of otherwise mode contribution is the imperfection introduced in Si metasurface production: Small misalignment between the glass and PDMS mold step in the s-NIL process (Fig. 4.2(e)) is responsible for the TM mode at θ = 14°. The TE and TM modes the $\Gamma \rightarrow$ M are distinguished by orange shaded-vertical lines for TE polarization and a blue shaded vertical line for TM polarization in Fig. 7.2.

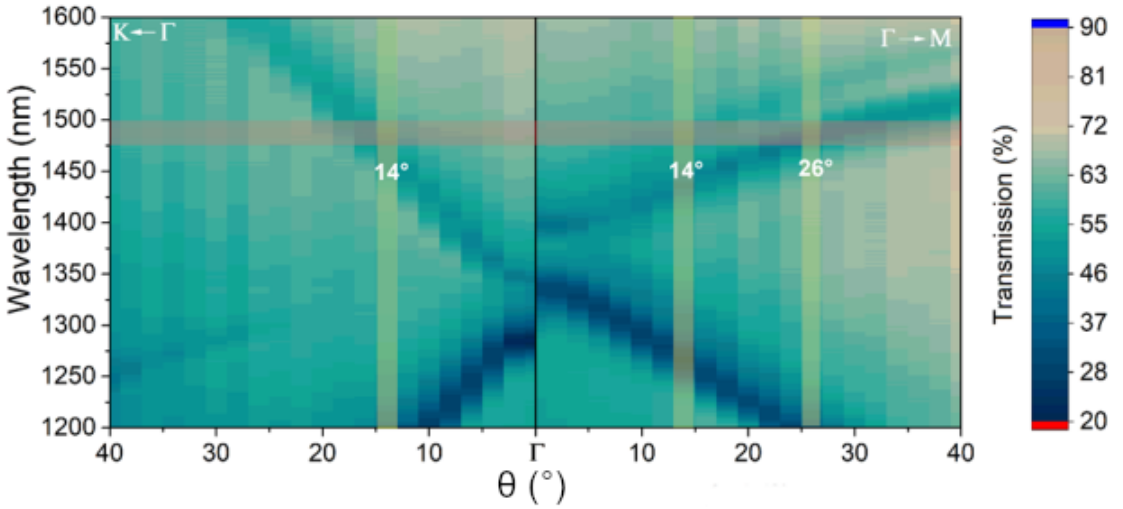

Figure 7.3: ARTM with TM polarized light on Si metasurface before β-$NaYF_4$: Er^{3+}deposition on Si metasurface. Rotations are through the high symmetry direction Γ → K (left) and Γ → M (right). Taken from supporting information for Ahiboz *et al*. [79].

The electric field enhancement on the Si metasurface is shown in Fig. 7.2 (d) to explain the source of the emission peaks of the ARLM spectra. The electric field energy enhancement is calculated within a volume 600 nm over the metasurface as a ratio of the incident electric field energy density to total electric field energy density described in Eqn. 4.4. The enhanced electric near fields up to 1000-fold are found due to the leaky mode-incident radiation coupling on the Si metasurface. The electromagnetic field energy enhancement is shown as light blue-brown lines in Fig. 7.2 (d). The maximum electromagnetic field energy enhancement factors at TE polarized λ_{exc} = 1551 nm are calculated as 900-fold, 730-fold at for θ = 7.3° and = 16.7°, whereas 157-fold enhancement is calculated for TM polarized λ_{exc} = 1551 nm at θ = 27.2°. The reason for the apparent difference between integrated UC luminescence peaks in ARLM and simulation of electrical near-field enhancement originated from limitations on the sensitivity of the angular detection of the experimental setup (± 2°, see Chapter-4). The three modes have different electrical-near field enhancement values due distribution of the w_e. The two-dimensional distribution of electric field energy density at θ = 7.3°, = 16.7° and = 27.2° profiles for the three orthogonal planes are depicted in Fig. 7.4 (a)-(c). Each column of Fig. 7.4 shows the three leaky modes separately. The black hexagonal in Fig. 7.4 (a) represents the unit cell of the metasurface lattice, while the black circle in the middle shows the

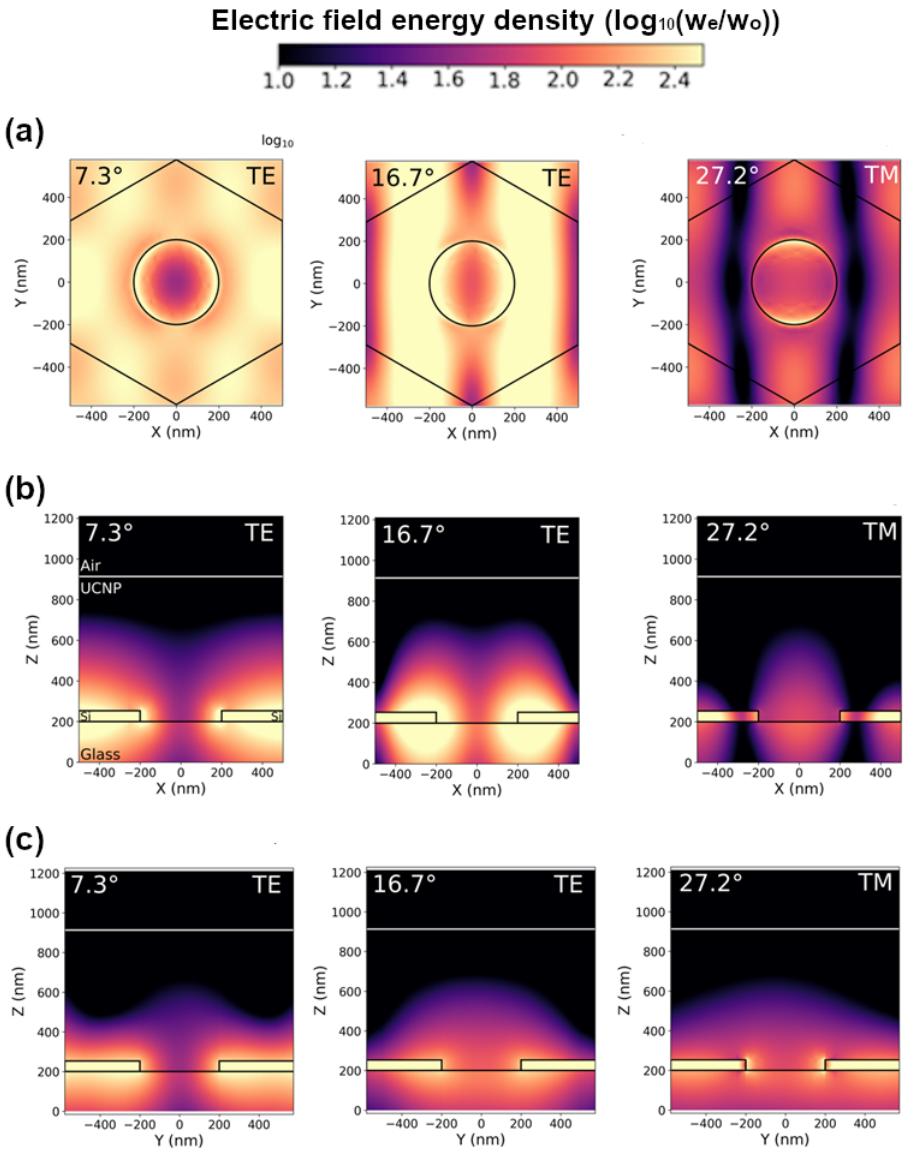

Figure 7.4: The electric field energy density in three orthogonal planes of the unit cell at the tree specified resonant θ with $\lambda_{\text{exc}} = 1551\,\text{nm}$. The x-y plane (a) is evaluated at $z = 1\,\text{nm}$ above the Si metasurface. The x-z (b) and y-z (c) planes are evaluated at $y = 0$ and $x = 0$, respectively. The θ and polarization state of the $\lambda_{\text{exc}} = 1551\,\text{nm}$ are indicated in each case; in part (b) the materials of the each leyer of the sample, UCNP - silicon (Si) and glass, are shown. Taken from supporting information for Ahiboz *et al*. [79].

nano-hole within the unit cell. The evaluated w_e above $z = 1\,\text{nm}$ shows that the w_e at $\theta = 7.3°$ in Fig. 7.4 (a) (left) reflects the rotational symmetries of the hexagonal

lattice of the Si metasurface and exhibits more evenly distributed electrical field density on x-y plane when it is compared with the ones at θ = 16.7° in Fig. 7.4 (a) (middle) and θ = 27.2° in Fig. 7.4 (a) (right). The w_e distributions in Fig. 7.4 (a), x-z plane in Fig. 7.4 (b) and y-z in Fig. 7.4 (c) show that the electromagnetic energy leaks through the both UCNP layer and the glass substrate, which is the characteristics of a leaky mode of a metasurface. However, the extent of the enhanced electrical fields is limited within 200 nm-300 nm UCNP layer as shown Fig. 7.4 (b) and (c). Among the three specific leaky modes, the one at θ = 8° (indicated with a green star in Fig. 7.2 (a)) with λ_{exc} = 1551 nm enhances UCNP's luminescence most due to its narrow FWHM, which is shown in Fig. 7.5 as angular dependent electrical field energy within the 600 nm β-$NaYF_4$:Er^{3+} UCNP layer. As previously discussed in section 4.1, the sharper the leaky mode resonance gets, and the stronger electrical near fields are created after the leaky mode-radiation coupling. The further luminescence measurements and examination of the UC dynamics of β-$NaYF_4$:Er^{3+} UCNPs and UC luminescence enhancement on Si metasurface with respect to planar Si surface are mainly based on leaky mode resonance at θ = 8° with λ_{exc} = 1551 nm.

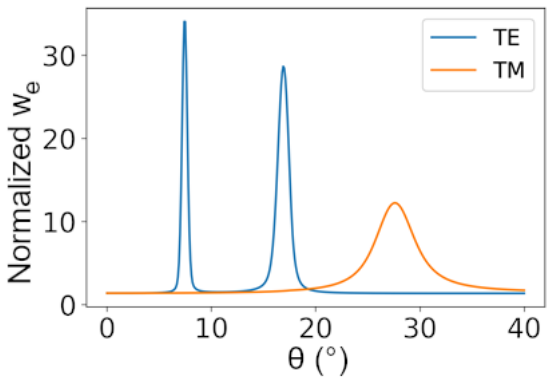

Figure 7.5: Electric field energy over the Si metasurface within β-$NaYF_4$:Er^{3+} UCNP layer with λ_{exc} = 1551 nm. Taken from supporting information for Ahiboz *et al*. [79].

7.1.2 The photon upconversion dynamics of the β-$NaYF_4$:Er^{3+} UCNPs on Si metasurface and planar Si surface

The dynamics of the UC on the Si metasurface and planar surface are investigated by P_{exc} dependent measurements. Luminescence measurements are done on the UCNPs on the Si metasurface inside an integrating sphere by the method explained in Fig. 4.9 (b). However, the experimental setup needed some modification for measurements on the planar Si sample because the UC luminescence emission intensity on the planar Si surface is so weak at low to intermediate (P_{exc}). Although an integrating sphere is able to harvest emission from every direction, it attenuates a significant portion of emission from a poor emitter, in general. The experimental setup described in Fig. 4.9 (c) was utilized for the UC measurements done on a planar Si sample without an integrating sphere. The tip of the fiber-coupled spectrometer was held as close as possible to the surface of the planar Si sample so that a significant UC luminescence can be recorded by the spectrometer. Although two different experimental setups are used for the measurements (integrating sphere for Si metasurface and without integrating sphere for planar Si sample), the rest of the experimental setup is identical to each other. Especially, the position of the sample on the optical path is kept fixed so that the excited area and spatial beam profile on the surfaces of the sample are the same for each measurement. Since the relative change in UC emission intensity from the UCNPs between two P_{exc} values is the matter to investigate UC dynamics, the exact values of the UC emission intensities do not affect the slope values of P_{exc} dependent slope factor analysis (see Chapter 4.2).

A series of P_{exc} dependent measurements on both UCNPs on Si metasurface and planar Si sample is performed. The UC emission peaks at 978 nm for 2-photon UC ($^4I_{11/2} \rightarrow {}^4I_{15/2}$), at 654 nm for 3-photons UC ($^4F_{9/2} \rightarrow {}^4I_{15/2}$) and are measured by sweeping P_{exc} with TE polarized λ_{exc} = 1551 nm. The 5-point moving average of the slope factors of λ_{em} = 978 nm ($^4I_{11/2} \rightarrow {}^4I_{15/2}$) and λ_{em} = 654 nm emission are illustrated in Fig. 7.6 (a) and (b), respectively. The slope factors are obtained by forward differentiation of the logarithm of the UC luminescence intensities for specified emission peaks with respect to the logarithm of the P_{exc}. As discussed in Chapter 4.2 in detail, the main UC mechanism at low-P_{exc} is expected to be ETU for 2-photons UC. At the low P_{exc}, the slopes factors of λ_{em} = 978 nm and λ_{em} = 654 nm are both correlated with findings of Chapter-6 for both on Si metasurface

and planar Si reference. However, with increasing P_{exc}, slope factors greatly reduce. Especially, the slope factor was reduced under the value predicted in Chapter-3 for high-P_{exc}. The intense near fields supported by Si metasurface at a resonant angle, θ = 8°, dramatically improves the absorption of UCNPs so that the energy levels are mostly depopulated by UC [31].

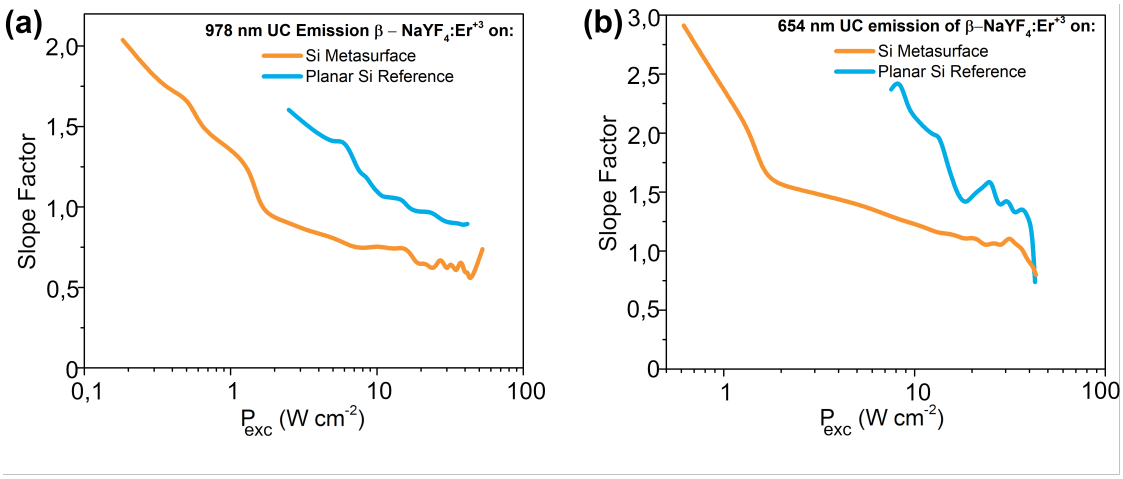

Figure 7.6: Excitation power density dependence of β-$NaYF_4$:Er^{3+} UC-NPs on Si metasurface (orange curves/dots) and planar Si reference (blue curves/dots): slope factors of (a) UC emission at 978 nm (($^4I_{11/2} \rightarrow {}^4I_{15/2}$) and (b) 654 nm ($^4I_{9/2} \rightarrow {}^4I_{15/2}$) UC emission, and (c) red-to-green emisson ratios with various P_{exc} with λ_{exc} = 1551 nm. Taken from Ahiboz *et al*. [79].

7.1.3 The enhanced upconversion luminescence of β-$NaYF_4$:Er^{3+} UCNP by the Si metasurface

The effect of the strong near fields provided by the leaky modes of the Si metasurface on UC luminescence is analyzed by comparing intensities and P_{exc} dependence of the UC luminescence of the β-$NaYF_4$:Er^{3+} UCNPs on the metasurface and planar Si reference. The UC emission spectra of the β-$NaYF_4$:Er^{3+} UCNPs under TM polarized excitation of P_{exc} = 52 W/cm^2 with λ_{exc} = 1551 nm at θ = 8°on the Si metasurface and planar Si reference are shown in Fig. 7.7. The UC emission spectrum of β-$NaYF_4$:Er^{3+} UCNPs on the Si planar reference is 100 times magnified for easy comparison. Nearly 100-fold more intense 2-photon upconversion emission at 978 nm due to $^4I_{11/2} \rightarrow {}^4I_{15/2}$ transition is observed. On the other hand, the luminescence of the transitions requiring more than two photons, such as transition $^4F_{9/2}$

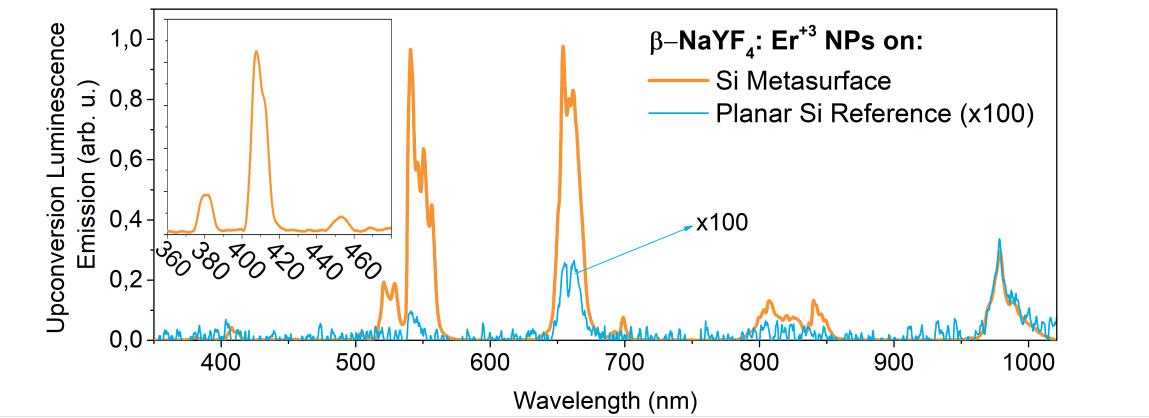

Figure 7.7: UC emission spectra of β-$NaYF_4$:Er^{3+} UCNPs on Si metasurface (orange curve) and planar Si reference (blue curve). The spectrum on planar Si reference is 100 times magnified. Inset: a close view of emission spectra on Si metasurface between 360 nm and 470 nm). Taken from Ahiboz *et al*. [79].

→ $^4I_{15/2}$ and $^4S_{3/2}$ → $^4I_{15/2}$, are enormously intense on Si metasurface comparing with planar Si reference. Furthermore, the UC emission factor, which is defined as the emission intensity ratios of the β-$NaYF_4$:Er^{3+} UCNPs on Si metasurface and planar Si reference, are inspected closely for the emission peaks at 978 nm ($^4I_{11/2}$ → $^4I_{15/2}$), 654 nm ($^4F_{9/2}$ → $^4I_{15/2}$) and 542 nm ($^4S_{3/2}$ → $^4I_{15/2}$) at θ's between -30° and +30° in Fig. 7.8 (a) in a way that the effect of the coupling between all the TM leaky modes of the Si metasurface in Γ → M and Γ → -M direction and incident radiation can be seen. The enhancement factors around the value of 10 at the non-resonant angles indicate that the luminescence enhancement can still be achieved with off-resonant interactions of Si metasurface. However, the source of UC emission enhancement at non-resonant θ is different from the leaky mode enhanced near fields. The enhanced UC emission is attributed to two different effects: the off-resonant interactions by nanostructures of the Si metasurface and presence of the 660 nm thick β-$NaYF_4$:Er^{3+} UCNP layer. In the case of off-resonant interactions, the reflected transmission orders can increase the absorption probability of 1551 nm photons by UCNPs. Moreover, the incident light can be diffracted by the periodic nanostructure of the Silicon metasurface and those diffraction orders can experience total internal reflection in β-$NaYF_4$:Er^{3+} UCNP layer. Consequently, better light trapping increases UC emission intensity [81]. Vast enhancement factors at resonant θ = ±8° and = ±18° in Fig. 7.8 (a), which perfectly matches with the predicted angular positions of the TM leaky modes in Fig. 7.2 (a)-(d), up to 100,

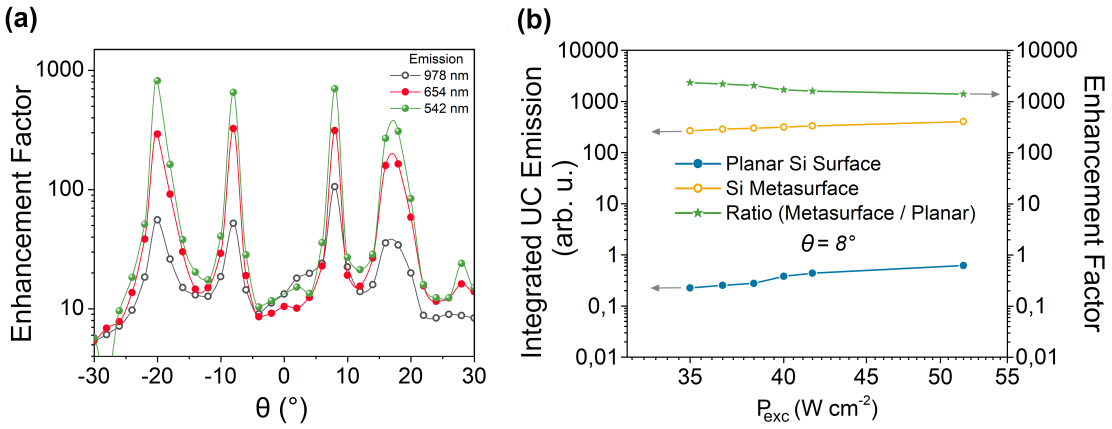

Figure 7.8: Excitation power density dependence of β-$NaYF_4$:Er^{3+} UC-NPs on Si metasurface (orange curves/dots) and planar Si reference (blue curves/dots): slope factors of (a) UC emission at 978 nm ($(^4I_{11/2} \rightarrow {}^4I_{15/2}$) and (b) 654 nm ($^4I_{9/2} \rightarrow {}^4I_{15/2}$) UC emission under P_{exc} = 35 - 52 W/cm^2 with λ_{exc} = 1551 nm. Taken from Ahiboz *et al*. [79].

300 and 800 times for λ_{em} = 978 nm, = 654 nm, and = 542 nm emission peaks are observed, respectively. The different enhancement factors at different wavelengths are due to differences in the population dynamics of each energy level. For example, Eqn. 3.27 predicts that 2-photon UC from an energy level has power dependence of P^2_{exc}, whereas 3-photon UC emission has P^3_{exc} at low-P_{exc}. Therefore, A difference in UC luminescence enhancement of 2- and 3-photon UC is expected up to 1-order, in principle. Especially, the 8-fold difference between the enhancement factors at λ_{em} = 978 nm and λ_{em} = 542 nm is close to the predicted 10-fold difference in enhancement factor. However, a striking difference between the two 3-photons enhancement factors at λ_{em} = 654 nm and λ_{em} = 542 nm exists, which can be caused by the fact that the CR pathways involve in λ_{em} = 654 nm emission as discussed before in Chapter-6 [175]. Nonetheless, the effect of the enhanced near fields by Si metasurface at resonant angles are immense numbers, a greater enhancement factors in total emission are expected. To verify, the UC emission spectra of the β-$NaYF_4$:Er^{3+} on Si metasurface and planar Si reference sample in Fig. 7.7 at resonant θ = 8° are integrated between 500 nm and 1021 nm. The choice of the lower limit of integration is based on the fact that the sub-500 nm emission on planar Si reference sample is beyond the detection capability of the experimental setup, whereas the upper limit at 1021 nm is the longest wavelength can be detected by the Si CCD array spectrometer. The integrated spectra and their ratios are called

integrated UC emission and UC emission enhancement factor, respectively. A large UC emission enhancement factor, 1150 times enhanced total emission, under P_{exc} = 52 W/cm^2 is recorded. Moreover, a possible power dependence of UC emission enhancement factor is investigated by varying P_{exc} from 52 W/cm^2 to 35 W/cm^2 as shown in Fig 7.8 (b). A gigantic UC emission enhancement factor of 2040 is achieved when P_{exc} = 35 W/cm^2. The decreasing trend of green lines and dots in Fig 7.8 (b) is evidence of the P_{exc} dependence of the UC emission enhancement factor. A close inspection of the integrated spectra of the Si metasurface (orange lines and dots in Fig 7.8 (b)) and the planar Si reference (blue lines and dots in Fig 7.8 (b)) shows that both integrated spectra increase with increasing P_{exc}, indeed. However, UC emission intensity on planar Si reference sample is more strongly depends on P_{exc} than on Si metasurface in the measured range of P_{exc}. This behavior is attributed to extremely intense P_{exc} experienced by the β-$NaYF_4$:Er^{3+} due to intense near fields provided by the leaky mode. In this intense excitation regime, the main depopulation mechanism of the electronic levels of the Er^{3+} is excitation through the high energy levels, namely, ETU is a significant effect on the UC process while the main depopulation of the electronic level on planar Si reference sample still dominated by UC through the ground state relaxation [124]. In addition, this effect can be traced in the Fig. 7.6 (a) and (b) by comparing the slope factor of λ_{em} = 978 nm and λ_{em} = 654 nm emission on Si metasurface and planar Si reference sample between P_{exc} = 52 W/cm^2 and = 32 W/cm^2.

7.2 The Enhanced Photon Upconversion Emission of the β-$NaYF_4$: Yb^{3+} / Er^{3+} by Silicon Metasurface upon 980 nm Excitation

In this section, the Si metasurfaces were produced by Doguscan Ahiboz at Helmholtz-Zentrum Berlin (HZB). The UCNP production, UCNP/PMMA layer deposition on Si metasurface, and optical measurements are conducted by Robert Voigt and Dr. Christian Würth at Bundesanstalt für Materialforschung und -prüfung (BAM).

UC of the produced β-$NaYF_4$:Yb^{3+}/Er^{3+} UCNPs, which are spherical nanoparticles with an average diameter of 25 nm, in PMMA matrix on Si metasurface is investigated. A 125 nm thick UCNP/PMMA mixture covered on Si metasurface

with structural parameters: t_{Si} = 125 nm, p = 600 nm and d = 325 nm. The formed UCNP-PMMA layer on the Si metasurface is shown in 30° tilted angle SEM images in Fig. 7.9 (a) and (b).

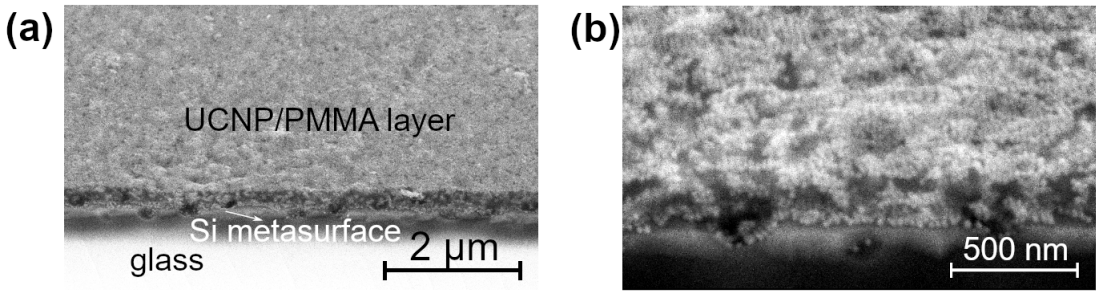

Figure 7.9: A large area (a) and a close-up (b) 30° tilted angle SEM cross-section images of the β-$NaYF_4$:Yb^{3+}/Er^{3+} UCNP-PMMA layer on Si metasurface. Reprinted with permission from Würth *et al*. [6]. Copyright 2020 American Chemical society.

The energy level diagram of β-$NaYF_4$:Yb^{3+}/Er^{3+} is shown in Fig. 7.10 (a). The

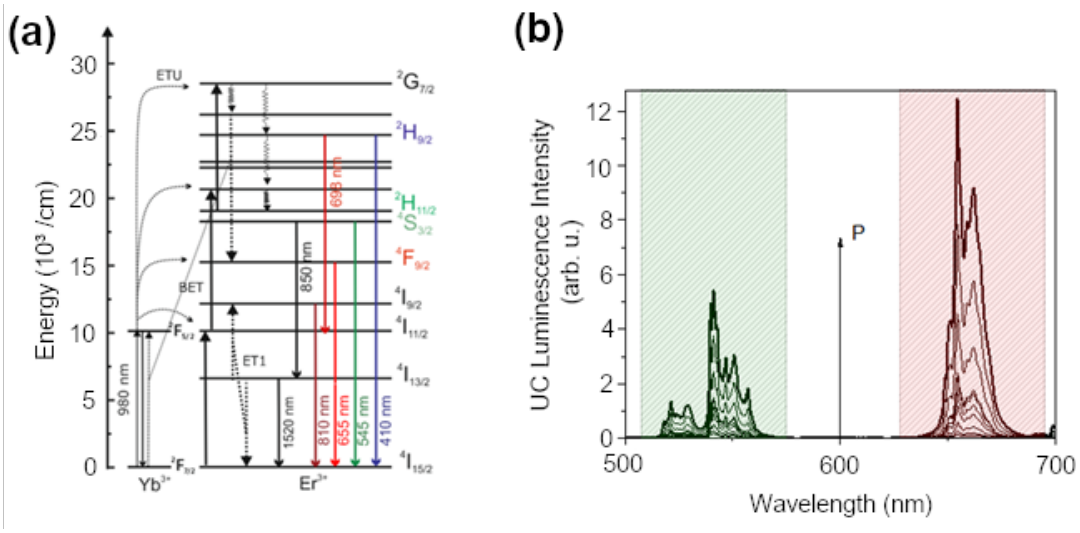

Figure 7.10: UC emission of β-$NaYF_4$:$Yb^{3+}Er^{3+}$ UCNPs: (a) Energy levels and electronic transitions of Yb^{3+} and Er^{3+}, (b) visible UC emission of the β-$NaYF_4$:Er^{3+} UCNPs under P_{exc} = 16 - 380 W/cm^2 with λ_{exc} = 980 nm. Reprinted with permission from Würth *et al*. [6]. Copyright 2020 American Chemical Society.

Er^{3+} ions are sensitized by Yb^{3+}, in other words, the electrons that are excited to form $^2F_{7/2}$ to $^2F_{5/2}$ of Yb^{3+} transfer their energy to electrons of Er^{3+}. Yb^{3+} ions has a better absorption of λ_{exc} = 980 nm excitation than Er^{3+} since the absorption cross-

section of $^4I_{15/2} \rightarrow {}^4I_{11/2}$ is much smaller than Yb^{3+}'s absorption cross-section of $^2F_{7/2} \rightarrow {}^2F_{5/2}$ transition [176–178]. In general, Yb^{3+} and Er^{3+} co-doped UCNPs are better better absorbers comparing the only Er^{3+} doped UCNPs under λ_{exc} = 976 nm excitation [179]. The visible UC emission between 500 nm and 700 nm from UCNPs is shown in Fig. 7.10 (b). The UCNPs are excited with various P_{exc} between 16 W/cm^2 and 380 W/cm^2 with λ_{exc} = 976 nm. The red emission (λ_{em} = 655 nm) from UCNPs-PMMA layer shows greater response to increasing *Pexc* than the green emission (λ_{em} = 545 nm), which indication of different population pathways of $^4F_{9/2}$ level of the Er^{3+}, as discussed in Chapter-4.2. This response can be useful for the detection of the electric field intensity in nano-scale since the ratio of the red and green emissions strongly depends on P_{exc}. ARTM of 125 nm thick UCNPs-PMMA layer on 125 nm thick Si metasurface is shown in Fig. 7.10 (a). The measurement is done by rotating the sample in $\Gamma \rightarrow$ K direction. The horizontal red shaded line in Fig. 7.11 (b) indicates the laser excitation wavelength that is used in UC luminescence measurement which is λ_{exc} = 976 nm. By tracing the λ_{exc}, the leaky mode around θ = 10° with narrow spectral width and a broad leaky mode between θ = 20°-30° that can potentially overlap with laser excitation wavelength can be distinguished from the other leaky modes on NIR spectra in Fig. 7.10 (a). As discussed before, in general, the coupling of a narrow leaky mode with external radiation over broader leaky modes as soon as a significant spectral overlap between the leaky modes and the excitation source are present. The UC emission enhancement factors, which are measured between 500 nm, and 700 nm, are shown in Fig. 7.11 (b). The ARLM is performed by rotation through $\Gamma \rightarrow$ K direction with three different P_{exc} = 12.5 W/cm^2, = 17.5 W/cm^2 and = 20 W/cm^2. The UC emission enhancement factors (with respect to the emission on the planar sample) more than 1000-fold at θ = 10° is achieved while comparably less emission enhancement factors are accomplished at θ > 20°. A significant, 10-fold, enhancement factors at off-resonant angles are observed, at any angle of incidence up to θ = 50° can be benefited to extract more photons under excitation with λ_{exc} = 976 nm. Furthermore, the enhancement factor is inversely depends on P_{exc}, likewise previously was observed for UC of the β-$NaYF_4$:Yb^{3+}/Er^{3+} UCNPs under λ_{exc} = 1551 nm excitation on Si metasurface.

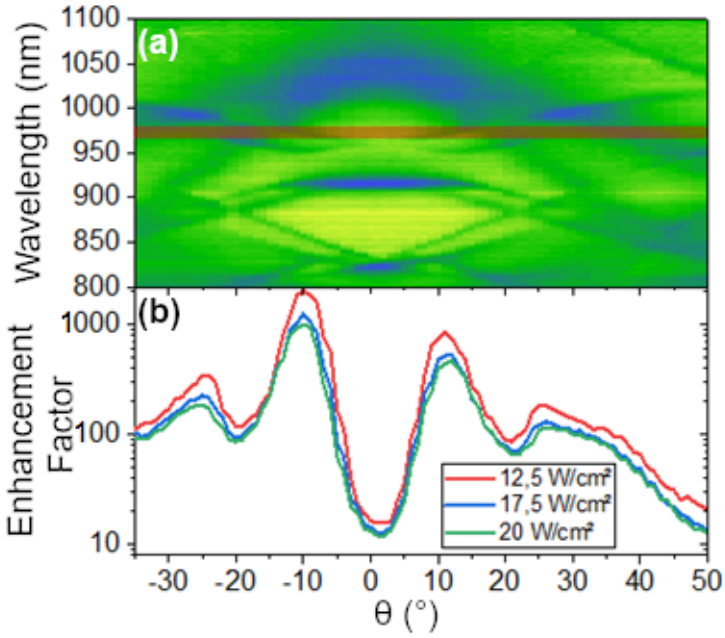

Figure 7.11: (a)Angle resolved transmittance measurement of UCNPS-PMMA on Si metasurface through Γ → K high symmetry direction.(b) UC emission enhancement factor as a function of angle of incidence. Reprinted with permission from Würth *et al*. [6]. Copyright 2020 American Chemical Society.

8 Discussion and Outlook

Chapters-5 to -7 of this monograph present and discuss the findings. In Chapter-5, the work on spectral engineering and identification of the modes of Si metasurfaces is explained. The study reveals that Si metasurfaces exhibit three distinct resonant phenomena: Leaky modes, Wood-Rayleigh modes, and BICs. The ARTM measurement results demonstrate that the spectral position of leaky modes of the Si metasurfaces can be easily adjusted by the thickness of the Si layer, making Si metasurfaces a suitable platform for enhancing the UC of the β-$NaYF_4$:Er^{3+} UCNPs. Chapter-6 presents a detailed analysis of the luminescent properties of the UCNP. The slope values of the excitation power-dependent measurements are modeled with the rate equation. Additionally, the mechanism behind the quenched blue emission and intense red emission of the β-$NaYF_4$:Er^{3+} UCNPs via CR are revealed. Chapter-7 tests the idea of enhanced UC by Si metasurface and demonstrates that Si metasurface can enhance UC up to 2040 times at P_{exc} = 35 W/cm^2 as a result of the coupling between leaky modes of the Si metasurfaces and 1551 nm laser excitation. However, a detailed discussion of future applications of the metasurface enhanced photon upconversion is still needed. The practical applications of Si metasurface-enhanced UC are discussed in, here, Chapter-8, which includes the feasibility and applicability concept of Si metasurface-enhanced UC for Si solar cells and optical detection.

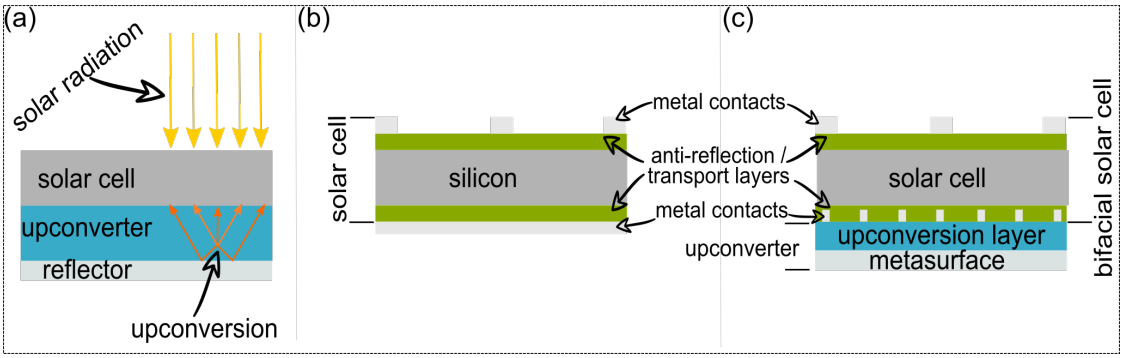

Figure 8.1: Upconterver implemented solar cells: (a) This illustration shows a solar cell with an upconverter and reflector. The yellow arrow represents solar photons, while the orange arrow shows upconverted photons. The second part of the diagram shows (b) a conventional Si solar cell and (c) a bifacial solar cell with an upconverter.

8.1 Application ideas of the Si metasurface enhanced photon upconversion

8.1.1 Silicon solar cells

The most effective way to implement an upconverter, any device which exhibits UC, to a solar cell is to place its back side (the side that not directly facing to the Sun) of a solar cell. A schematic drawing in Fig. 8.1 (a) illustrates such a solar cell with an upconverter. In Fig. 8.1 (a), the yellow arrows represent the solar radiation that hits the solar cells. The solar cell being discussed has an upconverter device and the reflection losses from its material interfaces and metallic layer are not considered. The solar cell is assumed to be a perfect absorber, meaning only sub-bandgap photons are transmitted to the metasurface and UCNPs. These transmitted sub-bandgap photons are absorbed and upconverted in sequence, producing UC emission, which is represented by the orange arrows in Fig. 8.1 (a). In order to collect the emitted photons and direct them towards the solar cells, a reflector is integrated under the upconverter since UC emission propagates in every direction. It is assumed that all UC photons are absorbed by the solar cell. To determine the benefits of using an upconverter in this scenario, the solar spectrum needs to be analyzed. The analysis is limited to Si solar cells since they dominate the solar cell market [180].

The amount of solar power that reaches Earth under AM 1.5 condition is 0.10

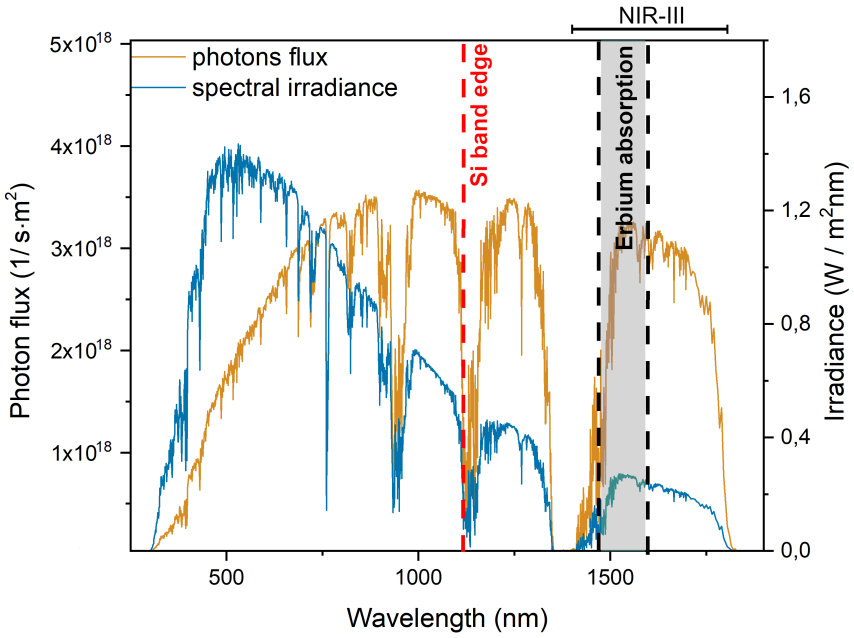

Figure 8.2: Spectral analysis of the A.M. 1.5 solar irradiance for photon upconversion

W/cm^2 [181]. A blue curve in Fig. 8.2 shows the spectral distribution of solar irradiance between 300 nm and 1800 nm [182]. Although the solar spectrum contains many photons with a wide range of wavelengths, not all are useful for a Si solar cell. Only photons with wavelengths shorter than the Si absorption band edge, which is indicated by a vertical dashed red line in Fig. 8.2, can be absorbed by the cell and generate electrical current. The power density reached on unit area can be calculated from solar irradiance spectra:

$$P_s = \int_{\lambda_1}^{\lambda_2} \phi_s(\lambda)\, d\lambda \tag{8.1}$$

where P_s, $\phi_s(\lambda)$, λ_1 and λ_2 are spectral power density (W/cm^2), spectral irradiance (W/m^{2}nm), the lower wavelength limit and upper wavelength limit (nm) of the integration, respectively. When P_s calculated for wavelengths longer than the Si band edge (λ_1 = 1100 and λ_2 = 1800 nm) in Fig. 8.2, it reveals that a significant portion of the spectral irradiance, equivalent to 15 mW/cm^2, is transmitted through the Si solar cell without contributing electric current generation.

To determine the average photon flux that can be absorbed by the cell, one can

calculate the number of photons within the spectral irradiance:

$$\phi_p(\lambda) = \int_{\lambda_1}^{\lambda_2} \frac{\lambda \phi_s(\lambda)}{hc} d\lambda \tag{8.2}$$

where $\phi_p(\lambda)$ is the photon flux (1/s·m^2) while h and c are the Planck's constant and speed of light in free space. The calculated spectral photon flux is shown as an orange curve in Fig. 8.2 as a function of wavelength. The $\phi_p(\lambda)$ over the Si band edge is calculated as 1.57×10^{21} (1/s·m^2). In the NIR-III spectrum (λ_1 = 1400 nm to λ_2 = 1800 nm), only 3.33×10^{20} (1/s·m^2) of photon flux can be absorbed by Er^{3+} (in Fig. 8.2 as gray shaded area) when the photon flux is calculated by Eqn. 8.2 for λ_1 = 1400 nm and λ_2 = 1600 nm. The photon flux in this spectral range (1400 nm - 1600 nm) corresponds to GSA ($^4I_{15/2} \rightarrow {}^4I_{13/2}$) of the Er^{3+}. By using a perfect NIR upconverter, which can convert energy from every pair of photons into a single photon, the average photon flux that can be absorbed by Si solar cells can increase by 1.67×10^{20} (1/s·m^2). Here, it is assumed that the upconverter exhibits only 2-photon UC with 100 % efficiency and all the emitted photons from the upconverter are effectively gathered by the solar cell without any loss. In this assumption, a solar cell can gain 2.67 mA/cm^2 of photo current. However, it is important to note that there is no mechanism to limit the upconversion (UC) process to only 2-photon UC, as 3-photon UC processes may also occur simultaneously. Using a perfect upconverter, the pure 3-photon UC (only 3-photon UC is exhibited by the upconverter) can increase the photon flux only by 1.11×10^{20} (1/s·m^2) and it can generate photo current of 1.78 mA/cm^2 since energy of the three photons is converted into a single photon. While UC processes involving more than 3 photons can be considered, limiting the calculation to 3 photons is sufficient due to the power delivered by the Sun and the power dependence of the UCNPs UC, as discussed in Chapter-6. Therefore, it's expected that there will be an improvement of less than 1.67×10^{20} (1/s·m^2) in the photon flux that Si solar cells can absorb. While the calculated improvements in photo current in solar cell due to UC of the Er^{3+} (2.67 mA/cm^2 and 1.78 mA/cm^2 for purely 2-photon and 3-photon UC, respectively) are promising, it is not realistic to expect the same level of improvement in Si solar cell efficiency. These calculations are based on the assumption that Er^{3+} has unit quantum efficiency, which means that every incident photon can involve in GSA and every excited photon in the $^4I_{13/2}$ state of Er^{3+} is upconverted before relaxing back to its ground state. However, the

quantum efficiency of Er^{3+} upconversion is just a few percent under intense laser excitation [27]. The irradiance of the sun on Earth is not comparable with the excitation power densities that are reached on those experiments.

Fig. 8.1 displays three solar cell devices, each with its unique characteristics. The first device, in Fig. 8.1 (a), serves as an explanatory model and is not a functional solar cell. In contrast, the second device, in Fig. 8.1 (b), consists of multiple layers stacked on both sides of the Si absorber, making it more realistic. These layers, including charge transport layers, anti-reflection layers, and metal contacts, aid in charge separation within Si while minimizing reflections from the solar cell. The metal contacts in front and behind the solar cell can partially or completely prevent NIR radiation from reaching the upconverter. However, the third device, in Fig. 8.1 (c), known as a bifacial solar cell, enables light to engage to solar cell form its back side, making it unique [27, 183]. Moreover, bifacial design of the solar cell allows for NIR radiation to be transmitted through upconverter. Despite the optimization of carrier transport and anti-reflection layers to improve the Si solar cell's absorption, these layers can cause severe NIR radiation reflection losses for the upconverter. While optimizing these layers for upconversion is possible, it results in reflection losses for the solar cells [27]. However, the current UC efficiency of Er^{3+} doped UCNPs or bulk materials is not as competitive as that of well-optimized bifacial Si solar cells. Therefore, the benefit of minimizing NIR losses to improve UC performance of a upconverter through layer optimization is not significant.

Fig. 8.1 (c) demonstrates an photon upconverter integrated between a bifacial solar cell and the metasurface on the which recieves NIR light tranmitted through the solar cell. However, it is important to note that the upconversion emission enhancement factors presented in Chapter-7 may not be entirely expected for solar cell applications, as these values are only valid for a limited range of incidence angles which are the resonant angle of incidences (θ) of the leaky modes of the Si metasurfaces. In contrast, commercial solar cells are generally designed to be installed at an angle with respect to ground to receive sunlight perpendicular to their surface during peak irradiance, which causes shorter excitation times for resonant modes as Earth rotates [184]. While wider angle resonant modes may be preferable, they only offer minor enhancement factors. Furthermore, textured surfaces on either the front or back of solar cells can refract light within the solar cell, which increases the total internal reflection of the light coupled into the solar cell. Unfortunately, this can have a negative effect on the metasurface-enhanced upconversion, given that

the NIR light transmitted to the metasurface comes from multiple angles of incidence, with only a small fraction of the NIR light capable of coupling with leaky modes. The effects of near-field enhancement are only noticeable in a small volume above the metasurface. The electric field energy density calculations reveal that the majority of the electric field energy density is stored within the upconversion nanoparticles in close proximity to the silicon metasurface or within the silicon layer of the metasurface itself. As the thickness of the upconversion nanoparticles layer decreases on both the silicon metasurface and silicon planar surface, the enhancement factor of the silicon metasurface (compared to the emission on the planar silicon surface) shows a significant increase. Conversely, the upconversion enhancement factor is proportional to the upconversion emission on the planar silicon surface, and as the thickness of the upconversion nanoparticles layer increases, the enhancement factor decreases. According to recent calculations by B. Richards *et al.*, even in the most optimistic scenario, in which a purely 2-photon UC generates 3.77 mA/cm^{-2} photo current in a solar cell, the photon upconverter cannot compete with the 10 % - 30 % gain can be achieved by bifaciality of the solar cell without an upconverter. Therefore, it is not feasible to apply Er^{3+}-based upconverters to Si solar cells considering the current status of the solar cell designs [27].

8.1.2 Optical detection

At the nano-scale, it is possible to detect physical quantities such as temperature or electromagnetic field through optical means. This is done by monitoring the color and intensity of the UC emission produced by UCNPs. Fig. 8.3 provides an illustration of the UC emission coming from two different regions on UCNPs covered metasurface. These regions are characterized by high or low temperature, and strong or weak electromagnetic field, respectively.

Certain energy levels, such as $^4S_{3/2}$ and $^2H_{11/2}$, located close to each other, can serve as a thermometer at the nanoscale [185–187]. The temperature change in the vicinity of a UCNP affects the occupation of its phonon states. For instance, if a reaction occurs near the UCNPs, the emitted heat can be absorbed by nano-crystals of β-$NaYF_4$. This alteration affects the number of electrons that non-radiatively decay from $^2H_{11/2}$ to $^4S_{3/2}$ via MPR. The temperature of the local environment surrounding the UCNP can be determined by monitoring the relative UC emission intensity of λ_{em} = 542 nm to λ_{em} = 521 nm under λ_{exc} = 1551 nm by low power laser sources.

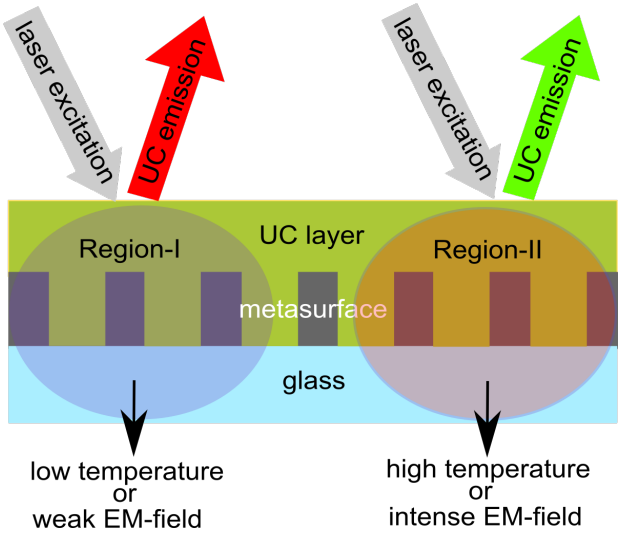

Figure 8.3: UC layer on top of a Si metasurface for detection purposes at nanoscale. The gray-shaded regions represent low-temperature and weak EMW field regions (region-I) and high-temperature and strong-EMW field regions (region-II).

Alternatively, as demonstrated in the last part of Chapter-7, UCNPs co-doped with Yb^{3+} and Er^{3+} can be excited by λ_{exc} = 980 nm, which populates $^4S_{3/2}$ via 2-photon processes. An electron in this state can absorb phonons and be excited to the $^2H_{11/2}$ state. In this scenario, the number of occupied phonon states determines the intensity of the λ_{em} = 542 nm.

The strength of the UC intensity at 654 nm compared to 542 nm is heavily influenced by the level of P_{exc} [79]. As P_{exc} increases, the relative intensity of UC emission at 654 nm decreases. This observation can be used to detect the electromagnetic field intensity at 1550 nm on a nanoscale level, which is valuable for integrated nanophotonic technology.

The metasurface and the concept of metasurface enhanced UC can be used to detect bio-molecules [188]. The surface of the UCNPs can be chemically modified to attach specific molecules [189, 190]. By attaching specific molecules to UCNPs, they can interact with target molecules. Detection of these molecules can be achieved by laser excitation at 1550 nm, 980 nm or 808 nm. Therefore, this method can be used to detect the target molecules with low power densities.

8.2 Brief outlook for enhanced photon upconversion by Si metasurfaces

Metasurface-enhanced photon upconversion has numerous practical applications, including the ability to reduce power consumption for laser-related tasks while maintaining luminescence intensity. A crucial use case for this technology is the production of useful UC emission from UCNPs for Si solar cells, which can harness the power of sub-bandgap photons of Si. By exciting at 1550 nm wavelength, significant enhancements of the UC emission from UCNPs up to 2040-fold have been achieved. However, this application is still not feasible for operating under sunlight. To further enhance the metasurface enhanced UC, Si master structures with slightly asymmetric nanostructures can be designed, such as elliptical nano-holes instead of circular ones. This allows external radiation to couple with resonant modes of Si metasurface, enhancing UC at normal incidence excitation and avoiding symmetry-protected BICs.

There are two points in this monograph that require further exploration. Firstly, the constant slope value of λ_{exc} = 808 nm in Fig 6.3 (d) is needed to study in a follow-up study. Through high power laser with λ_{exc} = 978 nm, the density of states of $^4I_{11/2}$ of Er^{3+} can be depleted while exciting $^4I_{9/2}$ state of Er^{3+} through increasing or decreasing P_{exc} values. The resulting luminescence spectra can reveal interactions that lead to the constant slope value. Secondly, to address the missing low-P_{exc} slope values of the emission peaks of 5-photon levels in Fig. 6.3 (h), an upgrade of detection unit of the measurement setup in Fig. 4.9 (b)-(d) is needed through future studies. This can help explain the behavior of the slope value at λ_{exc} = 808 nm, specifically if any of the 5-photon levels interact with $^4I_{9/2}$ level via ET or CR.

Conclusion

This dissertation aimed to gain a deep understanding of the properties of externally excited leaky metasurface resonances and their interaction with UC materials so that UC luminescence of the β-$NaYF_4$:Er^{3+} UCNPs under λ_{exc}=1551 nm excitation can be enhanced. The UC emission intensity of β-$NaYF_4$:Er^{3+} UCNPs was shown to dramatically improve more than 2040-fold on the produced Si metasurface.

First, two different kinds of large area (25 cm^2) Si metasurfaces were produced by a nano-imprinting lithography-based method: Mono-layer Si metasurface with hexagonal nanohole array with two different periods p = 600 nm and p = 1000 nm and double-layer Si metasurface consisting of a nanohole array on Si and Si disks supported by silicon-oxide nanopillars with p = 1000 nm. It has been demonstrated that the spectral position of the leaky modes can be systematically tuned by adjusting the silicon layer thickness of the metasurfaces during the Si deposition. The thickness of the silicon layer is an easily accessible geometric parameter of the metasurface production process, thereby, it offers a feasible and simple method for spectral engineering of the leaky modes. It has been shown that the produced mono-layer metasurfaces exhibit two different kinds of resonances in their directional transmittance measurement spectra; bound states in continuum and leaky modes. Measurement results show that the resonances provided by leaky modes can efficiently couple with incident light at a resonant angle of incidence, once the metastructure is resonant with probe wavelength. Numerical calculations predict that the leaky modes can exhibit strong near-fields within and in close vicinity of the metasurface as a result of its coupling with the incident radiation. Similarly,

bound states in continuum can also couple with incident light at off-resonant angles, i.e. when the symmetry protection of the mode is broken at a slightly oblique angle of incidence, and yielding in a resonant pattern in transmittance spectra of the metasurface. On the other hand, the leaky modes of Si metasurface are easier to couple with incident excitation with broader spectral width, yet they are predicted to enhance electric near-fields up to 3000-fold at resonant angles and 17-fold at normal incidence by numerical calculations. Nevertheless, by considering the aim of this dissertation, mono-layer silicon metasurface is referred to as a platform enhancing photon UC since their leaky modes are easily accessible.

Next, the excitation power density-dependent luminescence measurements done on β-$NaYF_4$:Er^{3+} UCNPs in c-hexane shows that high erbium content in the produced UCNPs results in deviations from excitation power dependence of the luminescence of UCNP as predicted by so-called power-law. Power law draws an empirical relation between UC emission and excitation power density, which states that the UC emission is proportional to the n-th power of the excitation power density, where n is the number of absorbed photons by a UC material to exhibit UC emission. The rate equation analysis on P_{exc} dependent UC luminescence intensity shows that UC dynamics of the UCNPs are more complex than predicted by power-law. Moreover, it's revealed that the blue emission at λ_{em} =448 nm and = 454 nm of β-$NaYF_4$:Er^{3+} are heavily quenched by cross-relaxation process which underpin red emission at λ_{exc} = 654 nm.

By placing the β-$NaYF_4$:Er^{3+} UCNPs on the Si metasurface and planar Si reference sample, the effect of the metasurface on the UC luminescence is explored. At the resonance angle of incidences, the coupling of the 1551 nm laser light and leaky modes of the Si metasurface gave rise to giant luminescence when compared with the UC luminescence on planar silicon reference. The strong near-fields emerging from the coupling of the leaky modes and the 1551 nm excitation at a resonant angle result in 2040-fold enhanced UC luminescence of the UCNPs on the Si metasurface. Furthermore, the correlation between the enhancement factor and excitation power density was investigated in detail. The results have shown that the enhancement factor has a dependence on excitation power density; the enhancement factor decreases with increasing excitation power density. Moreover, enhancement effects were investigated by comparing UC dynamics on the metasurface and planar silicon reference by comparing excitation power-dependent slope factors, which measure how UC emission intensity changes after a small change in excitation power

density. The difference in the slope factors of the UC luminescence on the metasurface and the planar silicon reference assures that the absorption of the 1551 nm photons increases on the metasurface and enables an estimation of the near-field enhancement factor. Furthermore, interactions between leaky modes and Erbium - Ytterbium co-doped β-$NaYF_4$ UCNPs embedded in the polymer matrix were investigated. A 125 nm thin layer of Poly-methyl-meth-acrylate (PMMA) - β-$NaYF_4$: Yb^{3+} / Er^{3+} UCNPs is covered on Si metasurface. It has been shown that UC emission can still be enhanced inside a dielectric layer and increase UC emission intensity. In addition, green (λ_{em} = 545 nm) and red (λ_{em} = 655 nm) emissions from UCNPs exhibit a different response to increasing excitation power density, the relative emission rate of red and green emission can be used to estimate electric field energy density below sub-micron thickness inside the UCNPs-PMMA layer.

Finally, the demonstrated silicon metasurface enhanced photon UC can reduce the requirement for intense excitation sources for photon UC-based applications. Although the UC emission is greatly enhanced by the metasurface, still, excitation power densities needed for improving photo conversation efficiency for a silicon solar cell by UC process cannot supported by the photon flux of 3.33×10^{20} (1/s·m^2) received by Sun in the 1400 nm - 1600 nm spectral range, where erbium ions can absorb incident radiation. Moreover, the leaky modes have narrow spectral widths comparing the NIR spectrum of the sun that erbium can absorb; a single leaky mode cannot couple with all photons of the 1400 nm - 1600 nm spectral region at a fixed angle of incidence. Further study can deal with broadening the spectral width of leaky modes while maintaining significant UC emission enhancement. In this case, a trade-off between covering a broad range of NIR wavelengths and reducing near-field intensity due to broadened spectral width of the leaky mode should be considered elaborately.

This research has demonstrated that an intense laser excitation can lead to an useful UC emission intensity. Although the metasurface enhanced UC concept may not be practical for solar cell usage due to the low quantum efficiency of UCNPs and limited range of enhanced near-fields over the metasurface, it's still possible to theoretically increase the photon flux on a solar cell by 1.67×10^{20} (1/s·m^2). Nevertheless, these findings are a crucial step forward in achieving the practical application of UC technology to solar cells.

The requirement for excitation power density for an efficient optical detection application can be reduced by employing Si metasurface a platform enhancing the

UC. Furthermore, the detection limit of an optical system probing UCNP's luminescence can benefit from the strong near-fields, since the UC luminescence signal can be greatly enhanced on the metasurface. Moreover, those findings can pave the way to realize nanoscale electromagnetic field sensing technologies as a technologically feasible method.

Contributions

Publications

1. Doğuşcan Ahiboz, Phillip Manley, and Christiane Becker. "Adjustable large-area dielectric metasurfaces for near-normal oblique incident excitation." OSA Continuum 3.4 (2020): 971-981.

2. Christian Würth, Phillip Manley, Robert Voigt, **Doğuşcan Ahiboz**, Christiane Becker, and Ute Resch-Genger. "Metasurface enhanced sensitized photon upconversion: Toward highly efficient low power upconversion applications and nanoscale E-field sensors." Nano Letters 20, no. 9 (2020): 6682-6689.

3. Phillip Manley, Michele Segantini, **Doğuşcan Ahiboz**, Martin Hammerschmidt, Georgios Arnaoutakis, Rowan W. MacQueen, Sven Burger, and Christiane Becker. "Double-layer metasurface for enhanced photon up-conversion." APL Photonics 6, no. 3 (2021): 036103.

4. Doğuşcan Ahiboz, Elina Andresen, Phillip Manley, Ute Resch-Genger, Christian Würth, and Christiane Becker. "Metasurface-Enhanced Photon Upconversion upon 1550 nm Excitation." Advanced Optical Materials 9, no. 24 (2021): 2101285.

5. Doğuşcan Ahiboz, Elina Andresen, Phillip Manley, Ute Resch Genger, Christian Würth, and Christiane Becker. "Enhanced photon upconversion using erbium-doped nanoparticles interacting with silicon metasurfaces." In 2021 IEEE 48th Photovoltaic Specialists Conference (PVSC), pp. 2008-2010. IEEE, 2021.

Bibliography

[1] M. You, J. Zhong, Y. Hong, Z. Duan, M. Lin, and F. Xu, "Inkjet printing of upconversion nanoparticles for anti-counterfeit applications," *Nanoscale*, vol. 7, no. 10, pp. 4423–4431, 2015.

[2] J. C. Goldschmidt and S. Fischer, "Upconversion for photovoltaics–a review of materials, devices and concepts for performance enhancement," *Advanced Optical Materials*, vol. 3, no. 4, pp. 510–535, 2015.

[3] R. Peltomaa, E. Benito-Peña, H. H. Gorris, and M. C. Moreno-Bondi, "Biosensing based on upconversion nanoparticles for food quality and safety applications," *Analyst*, vol. 146, no. 1, pp. 13–32, 2021.

[4] G. Lin and D. Jin, "Responsive sensors of upconversion nanoparticles," *ACS sensors*, vol. 6, no. 12, pp. 4272–4282, 2021.

[5] X. Wu, S. Zhan, J. Han, and Y. Liu, "Nanoscale ultrasensitive temperature sensing based on upconversion nanoparticles with lattice self-adaptation," *Nano Letters*, vol. 21, no. 1, pp. 272–278, 2020.

[6] C. Wurth, P. Manley, R. Voigt, D. Ahiboz, C. Becker, and U. Resch-Genger, "Metasurface enhanced sensitized photon upconversion: Toward highly efficient low power upconversion applications and nanoscale e-field sensors," *Nano Letters*, vol. 20, no. 9, pp. 6682–6689, 2020.

[7] N. Bloembergen, "Solid state infrared quantum counters," *Physical Review Letters*, vol. 2, no. 3, p. 84, 1959.

[8] A. Nadort, J. Zhao, and E. M. Goldys, "Lanthanide upconversion luminescence at the nanoscale: fundamentals and optical properties," *Nanoscale*, vol. 8, no. 27, pp. 13 099–13 130, 2016.

[9] F. Auzel, "History of upconversion discovery and its evolution," *Journal of Luminescence*, vol. 223, p. 116900, 2020.

[10] E. Snitzer and R. Woodcock, "Yb3+–er3+ glass laser," *Applied Physics Letters*, vol. 6, no. 3, pp. 45–46, 1965.

[11] H. Gandy, R. Ginther, and J. Weller, "Energy transfer in triply activated glasses," *Applied Physics Letters*, vol. 6, no. 3, pp. 46–49, 1965.

[12] C. K. Jørgensen, "Theoretical chemistry of rare earths," *Handbook on the physics and chemistry of rare earths*, vol. 3, pp. 111–169, 1979.

[13] L. A. Riseberg and H.-W. Moos, "Multiphonon orbit-lattice relaxation of excited states of rare-earth ions in crystals," *Physical Review*, vol. 174, no. 2, p. 429, 1968.

[14] L. Riseberg, "Laser-induced fluorescence-line-narrowing spectroscopy of glass: Nd," *Physical Review A*, vol. 7, no. 2, p. 671, 1973.

[15] T. Miyakawa and D. Dexter, "Phonon sidebands, multiphonon relaxation of excited states, and phonon-assisted energy transfer between ions in solids," *Physical Review B*, vol. 1, no. 7, p. 2961, 1970.

[16] F. K. Fong and W. A. Wassam, "Multi-quantum scattering processes in radiationless relaxation of electronically excited ions in crystals," *The Journal of Chemical Physics*, vol. 58, no. 3, pp. 956–960, 1973.

[17] D. Yeh, R. Petrin, W. Sibley, V. Madigou, J. Adam, and M. Suscavage, "Energy transfer between er 3+ and tm 3+ ions in a barium fluoride–thorium fluoride glass," *Physical Review B*, vol. 39, no. 1, p. 80, 1989.

[18] S. Tanabe, K. Hirao, and N. Soga, "Upconversion fluorescences of teo2-and ga2o3-based oxide glasses containing er3+," *Journal of non-crystalline solids*, vol. 122, no. 1, pp. 79–82, 1990.

[19] F. Auzel, "Upconversion processes in coupled ion systems," *Journal of Luminescence*, vol. 45, no. 1-6, pp. 341–345, 1990.

[20] J. Van der Ziel, L. Van Uitert, W. Grodkiewicz, and R. Mikulyak, "1.5-μm infrared excitation of visible luminescent in y1- x er x f3 and y1- x- y er x tm y f3 via resonant-energy transfer," *Journal of applied physics*, vol. 60, no. 12, pp. 4262–4267, 1986.

[21] C. Chen, R. Petrin, D. Yeh, W. A. Sibley, and J. Adam, "Concentration-dependent energy-transfer processes in er 3+-and tm 3+-doped heavy-metal fluoride glass," *Optics letters*, vol. 14, no. 9, pp. 432–434, 1989.

[22] M. Yin, W. Zhang, S. Xia, and J.-C. Krupa, "Luminescence of nanometric scale y2sio5: Eu3+," *Journal of luminescence*, vol. 68, no. 6, pp. 335–339, 1996.

[23] J.-C. Boyer, F. Vetrone, L. A. Cuccia, and J. A. Capobianco, "Synthesis of colloidal upconverting nayf4 nanocrystals doped with er3+, yb3+ and tm3+, yb3+ via thermal decomposition of lanthanide trifluoroacetate precursors," *Journal of the American Chemical Society*, vol. 128, no. 23, pp. 7444–7445, 2006.

[24] S. Heer, K. Kömpe, H.-U. Güdel, and M. Haase, "Highly efficient multicolour upconversion emission in transparent colloids of lanthanide-doped nayf4 nanocrystals," *Advanced Materials*, vol. 16, no. 23-24, pp. 2102–2105, 2004.

[25] S. Heer, O. Lehmann, M. Haase, and H.-U. Guedel, "Blue, green, and red upconversion emission from lanthanide-doped lupo4 and ybpo4 nanocrystals in a transparent colloidal solution," *Angewandte Chemie International Edition*, vol. 42, no. 27, pp. 3179–3182, 2003.

[26] J. Zhou, Q. Liu, W. Feng, Y. Sun, and F. Li, "Upconversion luminescent materials: advances and applications," *Chemical reviews*, vol. 115, no. 1, pp. 395–465, 2015.

[27] B. S. Richards, D. Hudry, D. Busko, A. Turshatov, and I. A. Howard, "Photon upconversion for photovoltaics and photocatalysis: A critical review: Focus review," *Chemical Reviews*, vol. 121, no. 15, pp. 9165–9195, 2021.

[28] E. Hemmer, A. Benayas, F. Légaré, and F. Vetrone, "Exploiting the biological windows: current perspectives on fluorescent bioprobes emitting above 1000 nm," *Nanoscale Horizons*, vol. 1, no. 3, pp. 168–184, 2016.

[29] M. H. Alkahtani, F. Alghannam, L. Jiang, A. A. Rampersaud, R. Brick, C. L. Gomes, M. O. Scully, and P. R. Hemmer, "Fluorescent nanodiamonds for luminescent thermometry in the biological transparency window," *Optics letters*, vol. 43, no. 14, pp. 3317–3320, 2018.

[30] G. Bottiroli and A. C. Croce, "Autofluorescence spectroscopy of cells and tissues as a tool for biomedical diagnosis." *Photochemical & photobiological sciences: Official journal of the European Photochemistry Association and the European Society for Photobiology*, vol. 3, no. 11-12, pp. 189–210, 2004.

[31] D. R. Gamelin and H. U. Gudel, "Upconversion processes in transition metal and rare earth metal systems," *Transition metal and rare earth compounds*, pp. 1–56, 2001.

[32] T. Tiedje, E. Yablonovich, G. Cody, and B. Brooks, "Limiting efficiency of silicon solar cells," *IEEE TRANSACTIONS ON ELECTRON DEVICES*, vol. ED-31, 1984, <br />.

[33] S. Fischer, J. Goldschmidt, P. Löper, G. Bauer, R. Brüggemann, K. Krämer, D. Biner, M. Hermle, and S. Glunz, "Enhancement of silicon solar cell efficiency by upconversion: Optical and electrical characterization," *Journal of applied physics*, vol. 108, no. 4, p. 044912, 2010.

[34] B. S. Richards and A. Shalav, "Enhancing the near-infrared spectral response of silicon optoelectronic devices via up-conversion," *IEEE Transactions on Electron Devices*, vol. 54, no. 10, pp. 2679–2684, 2007.

[35] A. Shalav, B. Richards, T. Trupke, K. Krämer, and H.-U. Güdel, "Application of nayf 4: Er 3+ up-converting phosphors for enhanced near-infrared silicon solar cell response," *Applied Physics Letters*, vol. 86, no. 1, p. 013505, 2005.

[36] P. Worsfold, A. Townshend, C. F. Poole, and M. Miró, *Encyclopedia of analytical science*. Elsevier, 2019.

[37] R. Zhang, L. Liang, Q. Meng, J. Zhao, H. T. Ta, L. Li, Z. Zhang, Y. Sultanbawa, and Z. P. Xu, "Responsive upconversion nanoprobe for background-free hypochlorous acid detection and bioimaging," *Small*, vol. 15, no. 2, p. 1803712, 2019.

[38] R. Arppe, L. Mattsson, K. Korpi, S. Blom, Q. Wang, T. Riuttamaki, and T. Soukka, "Homogeneous assay for whole blood folate using photon upconversion," *Analytical chemistry*, vol. 87, no. 3, pp. 1782–1788, 2015.

[39] M. Moskovits, "Surface-enhanced raman spectroscopy: a brief retrospective," *Journal of Raman Spectroscopy*, vol. 36, no. 6-7, pp. 485–496, 2005.

[40] S.-Y. Ding, E.-M. You, Z.-Q. Tian, and M. Moskovits, "Electromagnetic theories of surface-enhanced raman spectroscopy," *Chemical Society Reviews*, vol. 46, no. 13, pp. 4042–4076, 2017.

[41] S. Laing, L. E. Jamieson, K. Faulds, and D. Graham, "Surface-enhanced raman spectroscopy for in vivo biosensing," *Nature Reviews Chemistry*, vol. 1, no. 8, pp. 1–19, 2017.

[42] K. N. Kanipe, P. P. Chidester, G. D. Stucky, and M. Moskovits, "Large format surface-enhanced raman spectroscopy substrate optimized for enhancement and uniformity," *ACS nano*, vol. 10, no. 8, pp. 7566–7571, 2016.

[43] C. Miccichè, G. Arrabito, F. Amato, G. Buscarino, S. Agnello, and B. Pignataro, "Inkjet printing ag nanoparticles for sers hot spots," *Analytical Methods*, vol. 10, no. 26, pp. 3215–3223, 2018.

[44] M. Saboktakin, X. Ye, U. K. Chettiar, N. Engheta, C. B. Murray, and C. R. Kagan, "Plasmonic enhancement of nanophosphor upconversion luminescence in au nanohole arrays," *ACS nano*, vol. 7, no. 8, pp. 7186–7192, 2013.

[45] S.-M. Lee, W. Li, P. Dhar, S. Malyk, Y. Wang, W. Lee, A. Benderskii, and J. Yoon, "High-performance flexible nanostructured silicon solar modules with plasmonically engineered upconversion medium," *Advanced Energy Materials*, vol. 5, no. 21, p. 1500761, 2015.

[46] X. Liu and D. Y. Lei, "Simultaneous excitation and emission enhancements in upconversion luminescence using plasmonic double-resonant gold nanorods," *Scientific reports*, vol. 5, no. 1, pp. 1–13, 2015.

[47] P.-F. Guo, S. Wu, Q.-J. Ren, J. Lu, Z. Chen, S.-J. Xiao, and Y.-Y. Zhu, "Fluorescence enhancement by surface plasmon polaritons on metallic nanohole arrays," *The Journal of Physical Chemistry Letters*, vol. 1, no. 1, pp. 315–318, 2010.

[48] J. Kim, G. Dantelle, A. Revaux, M. Berard, A. Huignard, T. Gacoin, and J.-P. Boilot, "Plasmon-induced modification of fluorescent thin film emission nearby gold nanoparticle monolayers," *Langmuir*, vol. 26, no. 11, pp. 8842–8849, 2010.

[49] A. L. Feng, M. L. You, L. Tian, S. Singamaneni, M. Liu, Z. Duan, T. J. Lu, F. Xu, and M. Lin, "Distance-dependent plasmon-enhanced fluorescence of upconversion nanoparticles using polyelectrolyte multilayers as tunable spacers," *Scientific reports*, vol. 5, no. 1, pp. 1–10, 2015.

[50] J. Luan, J. J. Morrissey, Z. Wang, H. G. Derami, K.-K. Liu, S. Cao, Q. Jiang, C. Wang, E. D. Kharasch, R. R. Naik *et al.*, "Add-on plasmonic patch as a universal fluorescence enhancer," *Light: Science & Applications*, vol. 7, no. 1, pp. 1–13, 2018.

[51] G. Y. Lee, K. Jung, H. S. Jang, J. Kyhm, I. K. Han, B. Park, H. Ju, S. J. Kwon, and H. Ko, "Upconversion luminescence enhancement in plasmonic architecture with random assembly of metal nanodomes," *Nanoscale*, vol. 8, no. 4, pp. 2071–2080, 2016.

[52] A. Peter Amalathas and M. M. Alkaisi, "Nanostructures for light trapping in thin film solar cells," *Micromachines*, vol. 10, no. 9, p. 619, 2019.

[53] D. Pissuwan, C. Gazzana, S. Mongkolsuk, and M. B. Cortie, "Single and multiple detections of foodborne pathogens by gold nanoparticle assays," *Wiley Interdisciplinary Reviews: Nanomedicine and Nanobiotechnology*, vol. 12, no. 1, p. e1584, 2020.

[54] S. Schietinger, T. Aichele, H.-Q. Wang, T. Nann, and O. Benson, "Plasmon-enhanced upconversion in single nayf4: Yb3+/er3+ codoped nanocrystals," *Nano letters*, vol. 10, no. 1, pp. 134–138, 2010.

[55] N. Ganesh, W. Zhang, P. C. Mathias, E. Chow, J. Soares, V. Malyarchuk, A. D. Smith, and B. T. Cunningham, "Enhanced fluorescence emission from quantum dots on a photonic crystal surface," *Nature nanotechnology*, vol. 2, no. 8, pp. 515–520, 2007.

[56] C. Becker, S. Burger, C. Barth, P. Manley, K. Jager, D. Eisenhauer, G. Koppel, P. Chabera, J. Chen, K. Zheng *et al.*, "Nanophotonic-enhanced two-photon-excited photoluminescence of perovskite quantum dots," *ACS Photonics*, vol. 5, no. 11, pp. 4668–4676, 2018.

[57] L. Ondič, O. Babchenko, M. Varga, A. Kromka, J. Čtyrokỳ, and I. Pelant, "Diamond photonic crystal slab: Leaky modes and modified photoluminescence emission of surface-deposited quantum dots," *Scientific reports*, vol. 2, no. 1, pp. 1–6, 2012.

[58] C. Barth, S. Roder, D. Brodoceanu, T. Kraus, M. Hammerschmidt, S. Burger, and C. Becker, "Increased fluorescence of pbs quantum dots in photonic crystals by excitation enhancement," *Applied Physics Letters*, vol. 111, no. 3, p. 031111, 2017.

[59] N.-V. Hoang, A. Pereira, H. S. Nguyen, E. Drouard, B. Moine, T. Deschamps, R. Orobtchouk, A. Pillonnet, and C. Seassal, "Giant enhancement of luminescence down-shifting by a doubly resonant rare-earth-doped photonic metastructure," *ACS photonics*, vol. 4, no. 7, pp. 1705–1712, 2017.

[60] Z. Yin, Y. Zhu, W. Xu, J. Wang, S. Xu, B. Dong, L. Xu, S. Zhang, and H. Song, "Remarkable enhancement of upconversion fluorescence and confocal imaging of pmma opal/nayf4: Yb 3+, tm 3+/er 3+ nanocrystals," *Chemical Communications*, vol. 49, no. 36, pp. 3781–3783, 2013.

[61] W. Niu, L. T. Su, R. Chen, H. Chen, Y. Wang, A. Palaniappan, H. Sun, and A. I. Y. Tok, "3-dimensional photonic crystal surface enhanced upconversion emission for improved near-infrared photoresponse," *Nanoscale*, vol. 6, no. 2, pp. 817–824, 2014.

[62] A. Tittl, A. Leitis, M. Liu, F. Yesilkoy, D.-Y. Choi, D. N. Neshev, Y. S. Kivshar, and H. Altug, "Imaging-based molecular barcoding with pixelated dielectric metasurfaces," *Science*, vol. 360, no. 6393, pp. 1105–1109, 2018.

[63] T. G. Habteyes, I. Staude, K. E. Chong, J. Dominguez, M. Decker, A. Miroshnichenko, Y. Kivshar, and I. Brener, "Near-field mapping of optical modes on all-dielectric silicon nanodisks," *ACS Photonics*, vol. 1, no. 9, pp. 794–798, 2014.

[64] M. Decker, I. Staude, M. Falkner, J. Dominguez, D. N. Neshev, I. Brener, T. Pertsch, and Y. S. Kivshar, "High-efficiency dielectric huygens' surfaces," *Advanced Optical Materials*, vol. 3, no. 6, pp. 813–820, 2015.

[65] S. Romano, G. Zito, S. Manago, G. Calafiore, E. Penzo, S. Cabrini, A. C. De Luca, and V. Mocella, "Surface-enhanced raman and fluorescence spectroscopy with an all-dielectric metasurface," *The Journal of Physical Chemistry C*, vol. 122, no. 34, pp. 19 738–19 745, 2018.

[66] V. G. Veselago, "The electrodynamics of substances with simultaneously negative values of img align= absmiddle alt= eps/img and μ," *Physics-Uspekhi*, vol. 10, no. 4, pp. 509–514, 1968.

[67] S. John, "Strong localization of photons in certain disordered dielectric superlattices," *Physical review letters*, vol. 58, no. 23, p. 2486, 1987.

[68] E. Yablonovitch, "Inhibited spontaneous emission in solid-state physics and electronics," *Physical review letters*, vol. 58, no. 20, p. 2059, 1987.

[69] J. D. Joannopoulos, S. G. Johnson, J. N. Winn, and R. D. Meade, "Molding the flow of light," *Princeton Univ. Press, Princeton, NJ [ua]*, 2008.

[70] D. Rosenblatt, A. Sharon, and A. A. Friesem, "Resonant grating waveguide structures," *IEEE Journal of Quantum electronics*, vol. 33, no. 11, pp. 2038–2059, 1997.

[71] S. G. Johnson, S. Fan, P. R. Villeneuve, J. D. Joannopoulos, and L. Kolodziejski, "Guided modes in photonic crystal slabs," *Physical Review B*, vol. 60, no. 8, p. 5751, 1999.

[72] S. Fan and J. D. Joannopoulos, "Analysis of guided resonances in photonic crystal slabs," *Physical Review B*, vol. 65, no. 23, p. 235112, 2002.

[73] M. Deubel, G. Von Freymann, M. Wegener, S. Pereira, K. Busch, and C. M. Soukoulis, "Direct laser writing of three-dimensional photonic-crystal templates for telecommunications," *Nature materials*, vol. 3, no. 7, pp. 444–447, 2004.

[74] L. Ondič, M. Varga, K. Hruška, J. Fait, and P. Kapusta, "Enhanced extraction of silicon-vacancy centers light emission using bottom-up engineered polycrystalline diamond photonic crystal slabs," *ACS Nano*, vol. 11, no. 3, pp. 2972–2981, 2017.

[75] D. Andren, J. Martinez-Llinas, P. Tassin, M. Kall, and R. Verre, "Large-scale metasurfaces made by an exposed resist," *ACS Photonics*, vol. 7, no. 4, pp. 885–892, 2020.

[76] M. Kanskar, P. Paddon, V. Pacradouni, R. Morin, A. Busch, J. F. Young, S. Johnson, J. MacKenzie, and T. Tiedje, "Observation of leaky slab modes in an air-bridged semiconductor waveguide with a two-dimensional photonic lattice," *Applied physics letters*, vol. 70, no. 11, pp. 1438–1440, 1997.

[77] V. Astratov, D. Whittaker, I. Culshaw, R. Stevenson, M. Skolnick, T. Krauss, and R. De La Rue, "Photonic band-structure effects in the reflectivity of periodically patterned waveguides," *Physical Review B*, vol. 60, no. 24, p. R16255, 1999.

[78] A. K. Ghatak, "Leaky modes in optical waveguides," *optical and quantum electronics*, vol. 17, no. 5, pp. 311–321, 1985.

[79] D. Ahiboz, E. Andresen, P. Manley, U. Resch-Genger, C. Würth, and C. Becker, "Metasurface-enhanced photon upconversion upon 1550 nm excitation," *Advanced Optical Materials*, vol. 9, no. 24, p. 2101285, 2021.

[80] D. Ahiboz, P. Manley, and C. Becker, "Adjustable large-area dielectric metasurfaces for near-normal oblique incident excitation," *OSA Continuum*, vol. 3, no. 4, pp. 971–981, 2020.

[81] P. Manley, M. Segantini, D. Ahiboz, M. Hammerschmidt, G. Arnaoutakis, R. W. MacQueen, S. Burger, and C. Becker, "Double-layer metasurface for enhanced photon up-conversion," *APL Photonics*, vol. 6, no. 3, p. 036103, 2021.

[82] E. Gaillou, "An overview of gem opals: From the geology to color and microstructure," in *Proceedings of the Thirteenth Annual Sinkankas Symposium—Opal, Carlsbad, CA, USA*, vol. 18, 2015.

[83] F. Marlow, P. Sharifi, R. Brinkmann, and C. Mendive, "Opals: status and prospects," *Angewandte Chemie International Edition*, vol. 48, no. 34, pp. 6212–6233, 2009.

[84] V. Golubev, J. Hutchison, V. Kosobukin, D. Kurdyukov, A. Medvedev, A. Pevtsov, J. Sloan, and L. Sorokin, "Three-dimensional ordered silicon-based nanostructures in opal matrix: preparation and photonic properties," *Journal of non-crystalline solids*, vol. 299, pp. 1062–1069, 2002.

[85] B. D. Wilts, B. A. Zubiri, M. A. Klatt, B. Butz, M. G. Fischer, S. T. Kelly, E. Spiecker, U. Steiner, and G. E. Schröder-Turk, "Butterfly gyroid nanostructures as a time-frozen glimpse of intracellular membrane development," *Science advances*, vol. 3, no. 4, p. e1603119, 2017.

[86] J. Hu, S. Bandyopadhyay, Y.-h. Liu, and L.-y. Shao, "A review on metasurface: from principle to smart metadevices," *Frontiers in Physics*, vol. 8, p. 502, 2021.

[87] S. M. Kamali, E. Arbabi, A. Arbabi, and A. Faraon, "A review of dielectric optical metasurfaces for wavefront control," *Nanophotonics*, vol. 7, no. 6, pp. 1041–1068, 2018.

[88] V. A. Fedotov, J. Wallauer, M. Walther, M. Perino, N. Papasimakis, and N. I. Zheludev, "Wavevector selective metasurfaces and tunnel vision filters," *Light: Science & Applications*, vol. 4, no. 7, pp. e306–e306, 2015.

[89] A. M. Shaltout, V. M. Shalaev, and M. L. Brongersma, "Spatiotemporal light control with active metasurfaces," *Science*, vol. 364, no. 6441, p. eaat3100, 2019.

[90] J. Wang and J. Du, "Metasurfaces for spatial light manipulation," *Metamaterials: Devices and Applications*, p. 57, 2017.

[91] J. Engelberg and U. Levy, "The advantages of metalenses over diffractive lenses," *Nature communications*, vol. 11, no. 1, pp. 1–4, 2020.

[92] Y. Meng, Y. Chen, L. Lu, Y. Ding, A. Cusano, J. A. Fan, Q. Hu, K. Wang, Z. Xie, Z. Liu *et al.*, "Optical meta-waveguides for integrated photonics and beyond," *Light: Science & Applications*, vol. 10, no. 1, pp. 1–44, 2021.

[93] A. C. Overvig, S. Shrestha, S. C. Malek, M. Lu, A. Stein, C. Zheng, and N. Yu, "Dielectric metasurfaces for complete and independent control of the optical amplitude and phase," *Light: Science & Applications*, vol. 8, no. 1, pp. 1–12, 2019.

[94] M. Liu, W. Zhu, P. Huo, L. Feng, M. Song, C. Zhang, L. Chen, H. J. Lezec, Y. Lu, A. Agrawal *et al.*, "Multifunctional metasurfaces enabled by simultaneous and independent control of phase and amplitude for orthogonal polarization states," *Light: Science & Applications*, vol. 10, no. 1, pp. 1–11, 2021.

[95] S. Gao, C. Zhou, W. Yue, Y. Li, C. Zhang, H. Kan, C. Li, S.-S. Lee, and D.-Y. Choi, "Efficient all-dielectric diatomic metasurface for linear polarization generation and 1-bit phase control," *ACS Applied Materials & Interfaces*, vol. 13, no. 12, pp. 14 497–14 506, 2021.

[96] S.-E. Mun, J. Hong, J.-G. Yun, and B. Lee, "Broadband circular polarizer for randomly polarized light in few-layer metasurface," *Scientific reports*, vol. 9, no. 1, pp. 1–8, 2019.

[97] C. F. Kenworthy, L. P. Stoevelaar, A. J. Alexander, and G. Gerini, "Using the near field optical trapping effect of a dielectric metasurface to improve sers enhancement for virus detection," *Scientific reports*, vol. 11, no. 1, pp. 1–10, 2021.

[98] A. Zangwill, *Modern electrodynamics*. Cambridge University Press, 2013.

[99] M. Fox, "Optical properties of solids," 2002.

[100] K. Sakoda, *Optical properties of photonic crystals*. Springer Science & Business Media, 2004, vol. 80.

[101] J. Singleton, *Band theory and electronic properties of solids*. Oxford University Press, 2001, vol. 2.

[102] E. Armstrong and C. O'Dwyer, "Artificial opal photonic crystals and inverse opal structures–fundamentals and applications from optics to energy storage," *Journal of materials chemistry C*, vol. 3, no. 24, pp. 6109–6143, 2015.

[103] S. H. Simon, *The Oxford solid state basics*. OUP Oxford, 2013.

[104] J. Hu and C. R. Menyuk, "Understanding leaky modes: slab waveguide revisited," *Advances in Optics and Photonics*, vol. 1, no. 1, pp. 58–106, 2009.

[105] V. Lousse, W. Suh, O. Kilic, S. Kim, O. Solgaard, and S. Fan, "Angular and polarization properties of a photonic crystal slab mirror," *Optics express*, vol. 12, no. 8, pp. 1575–1582, 2004.

[106] T. Ochiai and K. Sakoda, "Dispersion relation and optical transmittance of a hexagonal photonic crystal slab," *Physical review B*, vol. 63, no. 12, p. 125107, 2001.

[107] C. W. Hsu, B. Zhen, A. D. Stone, J. D. Joannopoulos, and M. Soljačić, "Bound states in the continuum," *Nature Reviews Materials*, vol. 1, no. 9, pp. 1–13, 2016.

[108] A. I. Ovcharenko, C. Blanchard, J.-P. Hugonin, and C. Sauvan, "Bound states in the continuum in symmetric and asymmetric photonic crystal slabs," *Physical Review B*, vol. 101, no. 15, p. 155303, 2020.

[109] S. Joseph, S. Pandey, S. Sarkar, and J. Joseph, "Bound states in the continuum in resonant nanostructures: an overview of engineered materials for tailored applications," *Nanophotonics*, 2021.

[110] A. A. Darweesh, S. J. Bauman, D. T. Debu, and J. B. Herzog, "The role of rayleigh-wood anomalies and surface plasmons in optical enhancement for nano-gratings," *Nanomaterials*, vol. 8, no. 10, p. 809, 2018.

[111] M. Fox, *Quantum optics: an introduction*. OUP Oxford, 2006, vol. 15.

[112] C. J. Foot, *Atomic physics*. OUP Oxford, 2004, vol. 7.

[113] R. Menzel, *Photonics: linear and nonlinear interactions of laser light and matter*. Springer Science & Business Media, 2013.

[114] K. A. Gschneidner, J.-C. G. Bunzli, and V. K. Pecharsky, *Handbook on the physics and chemistry of rare earths*. Elsevier, 2005, vol. 34.

[115] D. H. McIntyre, *Quantum mechanics*. Cambridge University Press, 2022.

[116] B. Wardle, *Principles and applications of photochemistry*. John Wiley & Sons, 2009.

[117] C. M. Marian, "Spin–orbit coupling and intersystem crossing in molecules," *Wiley Interdisciplinary Reviews: Computational Molecular Science*, vol. 2, no. 2, pp. 187–203, 2012.

[118] B. G. Wybourne, "The fascination of the rare earths—then, now and in the future," *Journal of alloys and compounds*, vol. 380, no. 1-2, pp. 96–100, 2004.

[119] B. R. Judd, "Optical absorption intensities of rare-earth ions," *Physical review*, vol. 127, no. 3, p. 750, 1962.

[120] G. Ofelt, "Intensities of crystal spectra of rare-earth ions," *The journal of chemical physics*, vol. 37, no. 3, pp. 511–520, 1962.

[121] B. Walsh, B. Di Bartolo, and O. Forte, "Advances in spectroscopy for lasers and sensing," *Judd-Ofelt Theory: Principles and Practices*, pp. 403–433, 2006.

[122] R. S. Quimby, *Photonics and lasers: an introduction*. John Wiley & Sons, 2006.

[123] K. Kuroda and Y. Yoshikuni, "Determination of metastable state lifetimes of a high-concentration erbium-doped fiber under population inversion conditions at 980 nm pump and 1.5 μm probe wavelengths," *Applied Physics B*, vol. 126, no. 8, pp. 1–7, 2020.

[124] M. Pollnau, D. R. Gamelin, S. Lüthi, H. Güdel, and M. P. Hehlen, "Power dependence of upconversion luminescence in lanthanide and transition-metal-ion systems," *Physical Review B*, vol. 61, no. 5, p. 3337, 2000.

[125] R.-S. Liu, *Phosphors, up conversion nano particles, quantum dots and their applications*. Springer, 2017, vol. 1.

[126] F. E. Auzel, "Materials and devices using double-pumped-phosphors with energy transfer," *Proceedings of the IEEE*, vol. 61, no. 6, pp. 758–786, 1973.

[127] G. A. Jones and D. S. Bradshaw, "Resonance energy transfer: from fundamental theory to recent applications," *Frontiers in Physics*, vol. 7, p. 100, 2019.

[128] D. Donges and K. L. Bray, *Transition Metal and Rare Earth Compounds: Excited States, Transitions, Interactions II*. Springer Science & Business Media, 2001, vol. 2.

[129] M. Weber, "Radiative and multiphonon relaxation of rare-earth ions in y 2 o 3," *Physical Review*, vol. 171, no. 2, p. 283, 1968.

[130] Q. Pan, D. Yang, S. Kang, J. Qiu, and G. Dong, "Regulating mid-infrared to visible fluorescence in monodispersed er 3+-doped la 2 o 2 s (la 2 o 2 so 4) nanocrystals by phase modulation," *Scientific reports*, vol. 6, no. 1, pp. 1–12, 2016.

[131] G. Liu, "Advances in the theoretical understanding of photon upconversion in rare-earth activated nanophosphors," *Chemical Society Reviews*, vol. 44, no. 6, pp. 1635–1652, 2015.

[132] J. D. Plummer, *Silicon VLSI technology: fundamentals, practice and modeling*. Pearson Education India, 2009.

[133] T. Ito and S. Okazaki, "Pushing the limits of lithography," *Nature*, vol. 406, no. 6799, pp. 1027–1031, 2000.

[134] L. R. Harriott, "Limits of lithography," *Proceedings of the IEEE*, vol. 89, no. 3, pp. 366–374, 2001.

[135] R. M. Hasan, X. Luo *et al.*, "Promising lithography techniques for next-generation logic devices," *Nanomanufacturing and Metrology*, vol. 1, no. 2, pp. 67–81, 2018.

[136] E. Sharma, R. Rathi, J. Misharwal, B. Sinhmar, S. Kumari, J. Dalal, and A. Kumar, "Evolution in lithography techniques: Microlithography to nanolithography," *Nanomaterials*, vol. 12, no. 16, p. 2754, 2022.

[137] S. T. Howell, A. Grushina, F. Holzner, and J. Brugger, "Thermal scanning probe lithography—a review," *Microsystems & nanoengineering*, vol. 6, no. 1, pp. 1–24, 2020.

[138] A. Cattoni, D. Mailly, O. Dalstein, M. Faustini, G. Seniutinas, B. Rösner, and C. David, "Sub-10 nm electron and helium ion beam lithography using a recently developed alumina resist," *Microelectronic Engineering*, vol. 193, pp. 18–22, 2018.

[139] J. A. Rogers and R. G. Nuzzo, "Recent progress in soft lithography," *Materials today*, vol. 8, no. 2, pp. 50–56, 2005.

[140] S. R. Quake and A. Scherer, "From micro-to nanofabrication with soft materials," *science*, vol. 290, no. 5496, pp. 1536–1540, 2000.

[141] Z. Ahmad and A. M. Rahman, "Plastics in waveguide application," *Reference Module in Materials Science and Materials Engineering; Elsevier: Amsterdam, The Netherlands*, 2021.

[142] Y. Xia and G. M. Whitesides, "Soft lithography," *Angewandte Chemie International Edition*, vol. 37, no. 5, pp. 550–575, 1998.

[143] H. Lan, *Soft UV nanoimprint lithography and its applications*. InTech New York, 2013.

[144] Y. Chen, Z. Shu, S. Zhang, P. Zeng, H. Liang, M. Zheng, and H. Duan, "Sub-10-nm fabrication: methods and applications," *International Journal of Extreme Manufacturing*, 2021.

[145] S. Y. Chou, P. R. Krauss, and P. J. Renstrom, "Imprint lithography with 25-nanometer resolution," *Science*, vol. 272, no. 5258, pp. 85–87, 1996.

[146] C. Becker, P. Wyss, D. Eisenhauer, J. Probst, V. Preidel, M. Hammerschmidt, and S. Burger, "5× 5 cm 2 silicon photonic crystal slabs on glass and plastic foil exhibiting broadband absorption and high-intensity near-fields," *Scientific reports*, vol. 4, no. 1, pp. 1–7, 2014.

[147] S. Y. Chou, P. R. Krauss, and P. J. Renstrom, "Nanoimprint lithography," *Journal of Vacuum Science & Technology B: Microelectronics and Nanometer Structures Processing, Measurement, and Phenomena*, vol. 14, no. 6, pp. 4129–4133, 1996.

[148] D. Qin, Y. Xia, and G. M. Whitesides, "Soft lithography for micro-and nanoscale patterning," *Nature protocols*, vol. 5, no. 3, p. 491, 2010.

[149] E. D. Palik, *Handbook of optical constants of solids*. Academic press, 1998, vol. 3.

[150] V. Sokolov, A. Zvyagin, S. Igumnov, S. Molchanova, M. Nazarov, A. Nechaev, A. Savelyev, A. Tyutyunov, E. Khaydukov, and V. Y. Panchenko, "Determination of the refractive index of β-nayf 4/yb 3+/er 3+/tm 3+ nanocrystals using spectroscopic refractometry," *Optics and Spectroscopy*, vol. 118, pp. 609–613, 2015.

[151] C. Becker, D. Lockau, T. Sontheimer, P. Schubert-Bischoff, E. Rudigier-Voigt, M. Bockmeyer, F. Schmidt, and B. Rech, "Large-area 2d periodic crystalline silicon nanodome arrays on nanoimprinted glass exhibiting photonic band structure effects," *Nanotechnology*, vol. 23, no. 13, p. 135302, 2012.

[152] C. Becker, V. Preidel, T. Sontheimer, C. Klimm, E. Rudigier-Voigt, M. Bockmeyer, and B. Rech, "Direct growth of periodic silicon nanostructures on imprinted glass for photovoltaic and photonic applications," *physica status solidi (c)*, vol. 9, no. 10-11, pp. 2079–2082, 2012.

[153] S. Wilhelm, M. Kaiser, C. Würth, J. Heiland, C. Carrillo-Carrion, V. Muhr, O. S. Wolfbeis, W. J. Parak, U. Resch-Genger, and T. Hirsch, "Water dispersible upconverting nanoparticles: effects of surface modification on their luminescence and colloidal stability," *Nanoscale*, vol. 7, no. 4, pp. 1403–1410, 2015.

[154] N. Ganesh, I. D. Block, P. C. Mathias, W. Zhang, E. Chow, V. Malyarchuk, and B. T. Cunningham, "Leaky-mode assisted fluorescence extraction: application to fluorescence enhancement biosensors," *Optics Express*, vol. 16, no. 26, pp. 21 626–21 640, 2008.

[155] R. Podgorsek, T. Sterkenburgh, J. Wolters, T. Ehrenreich, S. Nischwitz, and H. Franke, "Optical gas sensing by evaluating atr leaky mode spectra," *Sensors and Actuators B: Chemical*, vol. 39, no. 1-3, pp. 349–352, 1997.

[156] J. Pomplun, S. Burger, L. Zschiedrich, and F. Schmidt, "Adaptive finite element method for simulation of optical nano structures," *physica status solidi (b)*, vol. 244, no. 10, pp. 3419–3434, 2007.

[157] Y. Plotnik, O. Peleg, F. Dreisow, M. Heinrich, S. Nolte, A. Szameit, and M. Segev, "Experimental observation of optical bound states in the continuum," *Physical review letters*, vol. 107, no. 18, p. 183901, 2011.

[158] A. S. Kupriianov, Y. Xu, A. Sayanskiy, V. Dmitriev, Y. S. Kivshar, and V. R. Tuz, "Metasurface engineering through bound states in the continuum," *Physical Review Applied*, vol. 12, no. 1, p. 014024, 2019.

[159] K.-Y. Kim, X. Chong, F. Ren, and A. X. Wang, "Slow-light effect via rayleigh anomaly and the effect of finite gratings," *Optics letters*, vol. 40, no. 22, pp. 5339–5342, 2015.

[160] M. T. Berry and P. S. May, "Disputed mechanism for nir-to-red upconversion luminescence in nayf4: Yb3+, er3+," *The Journal of Physical Chemistry A*, vol. 119, no. 38, pp. 9805–9811, 2015.

[161] F. Frenzel, C. Würth, O. Dukhno, F. Przybilla, L. M. Wiesholler, V. Muhr, T. Hirsch, Y. Mély, and U. Resch-Genger, "Multiband emission from single β-nayf4 (yb, er) nanoparticles at high excitation power densities and comparison to ensemble studies," *Nano Research*, vol. 14, no. 11, pp. 4107–4115, 2021.

[162] P. S. Peijzel, A. Meijerink, R. Wegh, M. Reid, and G. W. Burdick, "A complete 4fn energy level diagram for all trivalent lanthanide ions," *Journal of solid state chemistry*, vol. 178, no. 2, pp. 448–453, 2005.

[163] S. Fischer, F. Hallermann, T. Eichelkraut, G. von Plessen, K. W. Krämer, D. Biner, H. Steinkemper, M. Hermle, and J. C. Goldschmidt, "Plasmon enhanced upconversion luminescence near gold nanoparticles–simulation and analysis of the interactions," *Optics express*, vol. 20, no. 1, pp. 271–282, 2012.

[164] Q. Feng, W. Zheng, J. Pu, Q. Chen, and W. Shao, "Nir-ii upconversion photoluminescence of er3+ doped liyf4 and nay (gd) f4 core-shell nanoparticles," *Frontiers in Chemistry*, vol. 9, p. 690833, 2021.

[165] S. Ryszczynska, K. Trejgis, Ł. Marciniak, and T. Grzyb, "Upconverting srf2: Er3+ nanoparticles for optical temperature sensors," *ACS Applied Nano Materials*, vol. 4, no. 10, pp. 10 438–10 448, 2021.

[166] D. Avram, I. Tiseanu, B. S. Vasile, M. Florea, and C. Tiseanu, “Near infrared emission properties of er doped cubic sesquioxides in the second/third biological windows,” *Scientific reports*, vol. 8, no. 1, pp. 1–12, 2018.

[167] R. Martínez, E. Polo, S. Barbosa, P. Taboada, P. Del Pino, and B. Pelaz, “808 nm-activable core@ multishell upconverting nanoparticles with enhanced stability for efficient photodynamic therapy,” *Journal of nanobiotechnology*, vol. 18, no. 1, pp. 1–15, 2020.

[168] T. Grzyb, D. Przybylska, A. Szczeszak, E. Śmiechowicz, P. Kulpiński, and I. R. Martín, “Multifunctional cellulose fibers: Intense red upconversion under 1532 nm excitation and temperature-sensing properties,” *Carbohydrate Polymers*, vol. 294, p. 119782, 2022.

[169] Y. Liu, Z. Zhou, S. Zhang, E. Zhao, J. Ren, L. Liu, and J. Zhang, “Mechanisms of upconversion luminescence of er3+-doped nayf4 via 980 and 1530 nm excitation,” *Nanomaterials*, vol. 11, no. 10, p. 2767, 2021.

[170] T. Chu, C. Zhu, and P. Wang, “Modeling of active fiber loop ring-down spectroscopy considering non-linear effects of edfa gain,” *IEEE Sensors Journal*, vol. 21, no. 3, pp. 3155–3162, 2020.

[171] M. Srivastava, D. Venkitesh, and B. Srinivasan, “Effects of wavelength filtering on pulse dynamics in a tunable, actively q-switched fiber laser,” *Optics & Laser Technology*, vol. 98, pp. 190–197, 2018.

[172] C. Renero-Lecuna, R. Martín-Rodríguez, R. Valiente, J. González, F. Rodríguez, K. Kramer, and H. Gudel, “Origin of the high upconversion green luminescence efficiency in β-nayf4: 2% er3+, 20% yb3+,” *Chemistry of Materials*, vol. 23, no. 15, pp. 3442–3448, 2011.

[173] H. Wu, Z. Hao, L. Zhang, X. Zhang, Y. Xiao, G.-H. Pan, H. Wu, Y. Luo, H. Zhao, and J. Zhang, “Phonon energy dependent energy transfer upconversion for the red emission in the er3+/yb3+ system,” *The Journal of Physical Chemistry C*, vol. 122, no. 17, pp. 9611–9618, 2018.

[174] J. Shan, M. Uddi, N. Yao, and Y. Ju, “Anomalous raman scattering of colloidal yb3+, er3+ codoped nayf4 nanophosphors and dynamic probing of the upcon-

version luminescence," *Advanced Functional Materials*, vol. 20, no. 20, pp. 3530–3537, 2010.

[175] A. Baride, P. S. May Jr, and M. T. Berry, "Cross-relaxation from er3+ (2h11/2, 4s3/2) and er3+ (2h9/2) in β-nayf4: Yb, er and implications for modeling up-conversion dynamics," *The Journal of Physical Chemistry C*, vol. 124, no. 3, pp. 2193–2201, 2019.

[176] T. Wei, Y. Tian, C. Tian, X. Jing, J. Zhang, L. Zhang, and S. Xu, "Optical spectroscopy and population behavior between 4 i 11/2 and 4 i 13/2 levels of erbium doped germanate glass," *Optical Materials Express*, vol. 4, no. 10, pp. 2150–2165, 2014.

[177] Q. Wang, R. Dahal, I.-W. Feng, J. Lin, H. Jiang, and R. Hui, "Emission and absorption cross-sections of an er: Gan waveguide prepared with metal organic chemical vapor deposition," *Applied Physics Letters*, vol. 99, no. 12, p. 121106, 2011.

[178] Q. Han, W. Yan, Y. Yao, Y. Chen, and T. Liu, "Optimal design of er/yb co-doped fiber amplifiers with an yb-band fiber bragg grating," *Photonics Research*, vol. 4, no. 2, pp. 53–56, 2016.

[179] J. Do Nascimento, A. Sales, D. Sousa, M. Da Silva, S. Moreira, K. Pavani, M. Soares, M. Graça, J. S. Kumar, and A. Sombra, "Temperature-, power-, and concentration-dependent two and three photon upconversion in er 3+/yb 3+ co-doped lanthanum ortho-niobate phosphors," *RSC advances*, vol. 6, no. 72, pp. 68 160–68 169, 2016.

[180] C. Ballif, F.-J. Haug, M. Boccard, P. J. Verlinden, and G. Hahn, "Status and perspectives of crystalline silicon photovoltaics in research and industry," *Nature Reviews Materials*, vol. 7, no. 8, pp. 597–616, 2022.

[181] P. Würfel and U. Würfel, *Physics of solar cells: from basic principles to advanced concepts*. John Wiley & Sons, 2016.

[182] A. Standard, "G173, 2012," *Standard Tables for Reference Solar Spectral Irradiances: Direct Normal and Hemispherical on*, vol. 37, 2012.

[183] T. S. Liang, M. Pravettoni, C. Deline, J. S. Stein, R. Kopecek, J. P. Singh, W. Luo, Y. Wang, A. G. Aberle, and Y. S. Khoo, "A review of crystalline silicon bifacial photovoltaic performance characterisation and simulation," *Energy & Environmental Science*, vol. 12, no. 1, pp. 116–148, 2019.

[184] G. Hailu and A. S. Fung, "Optimum tilt angle and orientation of photovoltaic thermal system for application in greater toronto area, canada," *Sustainability*, vol. 11, no. 22, p. 6443, 2019.

[185] X. Li, L. Yang, Y. Zhu, J. Zhong, and D. Chen, "Upconversion of transparent glass ceramics containing β-nayf 4: Yb 3+, er 3+ nanocrystals for optical thermometry," *RSC advances*, vol. 9, no. 14, pp. 7948–7954, 2019.

[186] Y. Cui, L. Zheng, W. Xu, H. Liu, L. Li, and Z. Zhang, "Influence of 980 nm pump power on optical thermometry based on nayf4: Yb3+/er3+ nanoparticles," *Materials Research Express*, vol. 5, no. 6, p. 065018, 2018.

[187] R. G. Geitenbeek, P. T. Prins, W. Albrecht, A. van Blaaderen, B. M. Weckhuysen, and A. Meijerink, "Nayf4: Er3+, yb3+/sio2 core/shell upconverting nanocrystals for luminescence thermometry up to 900 k," *The Journal of Physical Chemistry C*, vol. 121, no. 6, pp. 3503–3510, 2017.

[188] S. Zhang, C. L. Wong, S. Zeng, R. Bi, K. Tai, K. Dholakia, and M. Olivo, "Metasurfaces for biomedical applications: imaging and sensing from a nanophotonics perspective," *Nanophotonics*, vol. 10, no. 1, pp. 259–293, 2020.

[189] J.-C. Boyer, M.-P. Manseau, J. I. Murray, and F. C. Van Veggel, "Surface modification of upconverting nayf4 nanoparticles with peg- phosphate ligands for nir (800 nm) biolabeling within the biological window," *Langmuir*, vol. 26, no. 2, pp. 1157–1164, 2010.

[190] Y. Ma, M. Chen, and M. Li, "Hydrothermal synthesis of hydrophilic nayf4: Yb, er nanoparticles with bright upconversion luminescence as biological label," *Materials Letters*, vol. 139, pp. 22–25, 2015.